

NAVAL POSTGRADUATE SCHOOL MONTEREY, CALIFORNIA



THESIS

AEROTHERMAL EFFECTS ON THE INFRARED
SEEKER STARING SENSOR PERFORMANCE
OF HIGH SUPERSONIC MISSILES

by

Clélio Dinis Ferreira Leite

December, 1995

Thesis Advisor:

Alfred W. Cooper

Thesis Co-Advisors:

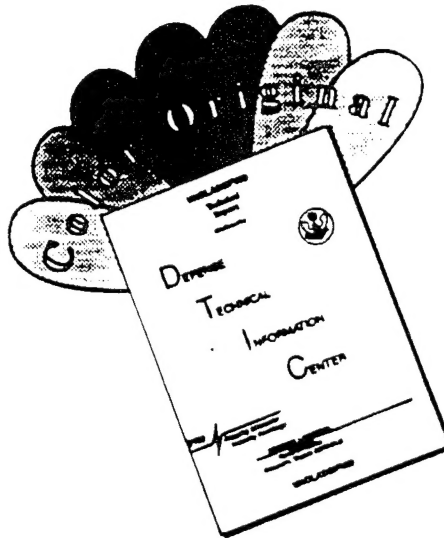
Max Platzer

Scott Davis

Approved for public release; distribution is unlimited.

19960806 008

DISCLAIMER NOTICE



THIS DOCUMENT IS BEST QUALITY AVAILABLE. THE COPY FURNISHED TO DTIC CONTAINED A SIGNIFICANT NUMBER OF COLOR PAGES WHICH DO NOT REPRODUCE LEGIBLY ON BLACK AND WHITE MICROFICHE.

REPORT DOCUMENTATION PAGE

Form Approved OMB No. 0704-0188

Public reporting burden for this collection of information is estimated to average 1 hour per response, including the time for reviewing instruction, searching existing data sources, gathering and maintaining the data needed, and completing and reviewing the collection of information. Send comments regarding this burden estimate or any other aspect of this collection of information, including suggestions for reducing this burden, to Washington Headquarters Services, Directorate for Information Operations and Reports, 1215 Jefferson Davis Highway, Suite 1204, Arlington, VA 22202-4302, and to the Office of Management and Budget, Paperwork Reduction Project (0704-0188) Washington DC 20503.

1. AGENCY USE ONLY (Leave blank)		2. REPORT DATE Dec 1995.	3. REPORT TYPE AND DATES COVERED Master's Thesis	
4. TITLE AND SUBTITLE Aerothermal Effects on the Infrared Seeker Staring Sensor Performance of High Supersonic Missiles (U)			5. FUNDING NUMBERS	
6. AUTHOR(S) Leite, Clélio D.Ferreira				
7. PERFORMING ORGANIZATION NAME(S) AND ADDRESS(ES) Naval Postgraduate School Monterey CA 93943-5000			8. PERFORMING ORGANIZATION REPORT NUMBER	
9. SPONSORING/MONITORING AGENCY NAME(S) AND ADDRESS(ES)			10. SPONSORING/MONITORING AGENCY REPORT NUMBER	
11. SUPPLEMENTARY NOTES The views expressed in this thesis are those of the author and do not reflect the official policy or position of the Department of Defense or the U.S. Government.				
12a. DISTRIBUTION/AVAILABILITY STATEMENT Approved for public release; distribution is unlimited.			12b. DISTRIBUTION CODE	
13. ABSTRACT (maximum 200 words) The present work investigates the aerothermal effects on the electro-optical performance of a conceptual infrared seeker missile at Mach 4 at small angles of attack. Two window dome configurations are studied: an optical hemisphere and ellipsoidal shape window attached to a 3:1 ogive nose. A three dimensional thin-layer compressible flow solver is used to compute the flow field in front of the window and the window aerodynamic heating. A solution adaptive-grid scheme is applied to accurately compute the flow field and capture the bow shock. Noise-Equivalent-Temperature-Difference degradation due to "background" noise of the hot window is derived and computed for 3 levels of array non-uniformity for a range of mean dome temperatures covering the whole supersonic regime. Acquisition range for a staring sensor is estimated for several maritime scenarios modeled by LOWTRAN code. Background photon flux distribution on an array generated by the hot dome is computed using radiation transfer methods using the dome temperature field obtained by computational fluid dynamic methods. It is found that array non-uniformity has a strong influence on the seeker performance. This study indicates that the non-uniformity of the dome temperature has significant influence on the array fixed pattern noise induced by dome emission and so in the seeker detection and tracking ability.				
14. SUBJECT TERMS Thermal Imaging, Polarization, Infrared Radiation			15. NUMBER OF PAGES 185	
			16. PRICE CODE	
17. SECURITY CLASSIFICATION OF REPORT Unclassified	18. SECURITY CLASSIFICATION OF THIS PAGE Unclassified	19. SECURITY CLASSIFICATION OF ABSTRACT Unclassified	20. LIMITATION OF ABSTRACT UL	

Approved for public release; distribution is unlimited.

AEROTHERMAL EFFECTS ON THE INFRARED SEEKER STARING SENSOR
PERFORMANCE OF HIGH SUPERSONIC MISSILES

Clélio Dinis Ferreira Leite
Lieutenant, Portuguese Navy
B.S., Portuguese Naval Academy, 1987

Submitted in partial fulfillment
of the requirements for the degree of

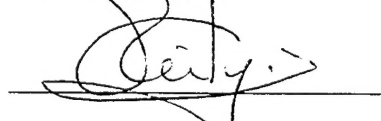
MASTER OF SCIENCE IN PHYSICS

from the

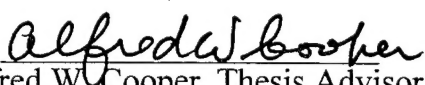
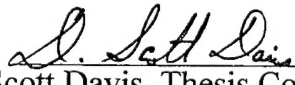
NAVAL POSTGRADUATE SCHOOL

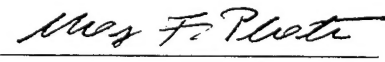
December 1995

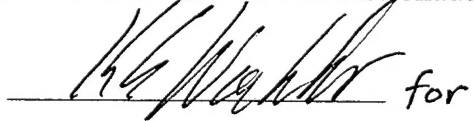
Author:


Clélio D. Ferreira Leite

Approved by:

 
Alfred W. Cooper, Thesis Advisor Scott Davis, Thesis Co-Advisor
Department of Physics


Max Platzer, Thesis Co-Advisor
Department of Aeronautics and Astronautics

 for
William B. Colson, Chairman of the Physics Department

ABSTRACT

The present work investigates the aerothermal effects on the electro-optical performance of a model infrared seeker missile at Mach 4 and small angle of attack. Two window dome configurations are studied: an optical hemispherical and ellipsoidal shape window attached to a 3:1 ogive nose. A three-dimensional thin-layer compressible flow solver is used to compute the flow field in front of the window and the window aerodynamic heating. Grid adaptation is performed in order to accurately compute the flow field and capture the bow shock. Noise-Equivalent-Temperature-Difference degradation due to "background" noise of the hot window is derived and computed for 3 levels of array non-uniformity for a range of mean dome temperatures covering the whole supersonic regime. Acquisition range for a staring sensor is estimated for several maritime scenarios modeled by LOWTRAN code. Background photon flux distribution on an array generated by the hot dome is computed using radiation transfer methods and the computed dome temperature. It is found that array non-uniformity has a strong influence on the seeker performance. This study indicates that the non-uniformity of the dome temperature field has a significant influence on the array fixed pattern noise induced by dome emission and, as a result, on the seeker detection and tracking ability.

TABLE OF CONTENTS

I.	INTRODUCTION	1
II.	BACKGROUND	5
	A. BLUNT BODY STRUCTURE	5
	B. AERODYNAMIC HEATING AND HEAT TRANSFER	6
	1. The Heat Transfer Process	6
	2. Recovery Temperature	9
	3. Heat Transfer to a Hemisphere	14
	C. AEROSTRUCTURE OF THE INFRARED DOME	18
	1. Thermal Shock Resistance of the IR Dome	19
	2. Pressure Induced Stresses	21
	D. RADIATION PROPERTIES OF SURFACES	24
	1. Radiometry	24
	2. Blackbody Radiation	27
	3. Directional Emissivity	30
	4. Optical Properties of Dielectric Window Materials	32
	E. DOME EMISSION AND EMISSIVITY AT HIGH TEMPERATURES	36
III.	GOVERNING EQUATIONS OF FLUID MECHANICS	41
	A. CONTINUITY EQUATION	41
	B. MOMENTUM EQUATION	42
	C. ENERGY EQUATION	43
	D. EQUATIONS IN NONDIMENSIONAL VECTOR FORM	45

E.	THIN LAYER APPROXIMATION	48
IV.	FLOW FIELD COMPUTATION	51
A.	METHODOLOGY	51
B.	BODY GEOMETRY AND GRID GENERATION	52
1.	Case I. Hemisphere-Ogive-Cylinder	53
2.	Case II. Ellipsoid-Ogive-Cylinder	55
3.	Case III. Hemisphere-Cylinder	55
C.	GRID ADAPTATION	55
D.	RESULTS AND DISCUSSION	59
E.	VALIDATION	71
V.	INFRARED SEEKER DETECTION PERFORMANCE DEGRADATION	75
A.	SENSOR PERFORMANCE PARAMETERS	75
1.	Basic Figures of Merit	75
2.	Noise Equivalent Temperature Difference (NETD)	77
3.	Noise Equivalent Quantum Flux for a CCD Array	79
B.	SIGNAL-TO-NOISE RATIO DEGRADATION DUE TO DOME EMISSION	83
C.	TARGET ACQUISITION RANGE DEGRADATION DUE TO DOME EMISSION	86
1.	Range Equation for Non-Imaging Systems	86
2.	Range Equation for Imaging Systems	89
D.	DETECTOR NONUNIFORMITY NOISE	96
1.	Fixed Pattern Noise	96
2.	Responsivity Variation	97
3.	Residual Nonuniformity	97

E.	COMPUTATION OF THE DETECTION RANGE	97
F.	RESULTS AND DISCUSSION	100
VI.	COMPUTATION OF PHOTON NOISE FROM HOT DOME	115
A.	RADIATION TRANSFER	115
B.	COMPUTATION METHOD	120
1.	System Ray-Transfer Matrix	120
2.	Calculation of the System Ray-Transfer Matrix	121
3.	Computation of the Entrance Pupil's Location	124
C.	RESULTS AND DISCUSSION	127
VII.	CONCLUSIONS	135
APPENDIX A.	CALCULATION OF DOME THICKNESS	137
APPENDIX B.	PROGRAM TO EXTRACT FLOW VARIABLES	143
APPENDIX C.	OVERFLOW INPUT/OUTPUT FILE SPECIFICATIONS	147
APPENDIX D.	LOWTRAN ATMOSPHERIC PROPAGATION MODEL	149
APPENDIX E.	SINGLE LENS DESIGN	153
APPENDIX F.	"POLE-FIT" EMISSIVITY MODEL	155
APPENDIX G.	RESULTS FROM ELECTROMAGNETIC THEORY	157

APPENDIX H.	RADIATION TRANSFER SOURCE CODE	163
LIST OF REFERENCES		169
INITIAL DISTRIBUTION LIST		171

ACKNOWLEDGEMENT

I would like to thank my thesis advisors for their support, guidance and encouragement that made this work possible. I am particularly indebted to Prof. Alfred Cooper who spent a considerable time in this project and supported me since the very beginning. I will always cherish his friendship. My thanks to the support of Prof. Max Platzner who taught me how to "never forget the basic principles" specially when we are dealing with a complex topic. I wish to thank Prof. John Ekaterinaris for all the help in the fluid dynamic computations and especially his patience, particularly upon my visit to NASA Ames Research Center. I wish to thank also Prof. Scott Davis by his support and excellent teaching. I am very grateful to Mr. Stanley Smith from the Naval-Air Warfare Center who helped me with several suggestions and some codes. I am grateful too to Dr. Claude Klein from Raytheon who sent me some of his papers and gave me some advice. I would like to thank Dr. Craig Lee who gave me a good insight of the problem in a early stage upon a visit to Texas Instruments. I should mention Prof. Garth Hobson, Dr. Emanuel Coelho and Mr. Tony Cricelli.

Finally I would like to extend thanks for the friendship of the wonderful people of Monterey Peninsula that made my stay an unforgettable experience and to the Portuguese Navy that made this project possible.

I. INTRODUCTION

Flight at high supersonic speeds through the atmosphere is characterized by high aerokinetic heating rates and gas compression in front of the missile. Large density variation and heating of the window significantly affects the performance of a vehicular infrared (IR) sensor, leading to major design problems of IR seeking missiles. Presently, IR windows that operate in the low supersonic flight regime exist and are in operation. However, future IR and dual mode tactical missiles will require IR systems which are capable of effective operation in much more severe flight environments. The durability and survivability of the dome plays a major role in defining the flight envelopes of these missiles.

For the case of a classical IR seeker installed at the tip of the missile nose, the outermost effect of the flow field on the optical performance is due to the large density jump across the bow shock wave in front of the IR window. This density gradient refracts optical rays and acts as a lens. Gas behind the shock is highly compressed and heated. Density variations in this compressed flow downstream of the shock create refractive index variations and have the effect of a gradient index lens. The principal optical effects are resolution (blur and defocus) and boresight error. Another effect of the compressed flow is aerodynamic heating of the window itself. As the IR dome heats up, its self-emission may adversely impact the operation of the seeker system in a high-speed flight situation. The added background-induced noise will lower the effective performance of the system in terms of detection range,

resolution and tracking capability. High resolution is desirable for detection (including clutter rejection), tracking accuracy, and recognition. The boresight error can affect performance in several ways. Boresight fluctuations (caused by turbulence, shock interaction, or coolant mixing) can blur images and induce angle noise in the tracking system. Changes in boresight caused by body motion (e.g. changing shock position or window distortion) appear as position errors or tracking rate errors that adversely affect sensors used in guidance and navigation.

Significant radiation from the compressed gas comes from heating by its passage through a strong shock wave. This effect, however, is only significant at higher Mach numbers ($\approx M > 7$), when the perfect gas assumption breaks down and chemical reactions must be considered.

A mission analysis [1] for the future tactical missile generation revealed a requirement for high supersonic speeds of operation. This will produce very high aerodynamic pressures and thermal stresses on the optical window that protects the IR detection system. Severe environmental conditions encountered at very high aerodynamic speeds has forced the development of new exotic materials, capable of withstanding such high temperatures and erosion. Traditionally, the shape of most IR windows or domes that protect the IR seeker has been a truncated hemisphere. Although this configuration has some advantages from the optics point of view, because of easier fabrication and design, it imposes a considerable aerodynamic drag penalty on the vehicle [2]. Therefore, an ellipsoidal window is proposed. Such window design would decrease

the aerodynamic drag of the vehicle, increasing its range. In addition, it is expected that it will delay boundary layer transition and reduce aerothermodynamically imposed stresses within the IR window material [3]. As a result, the self-emission photon radiation from the window into the detector will decrease [2] [4], and the detection range will improve.

The temperature field on the window is obtained numerically, using the OVERFLOW flow solver. Comparison with available data was conducted to validate to some degree the computation, and to give confidence in the temperature results obtained. Using this data, the aero-thermal effects which affect the imaging performance of an IR seeker were evaluated.

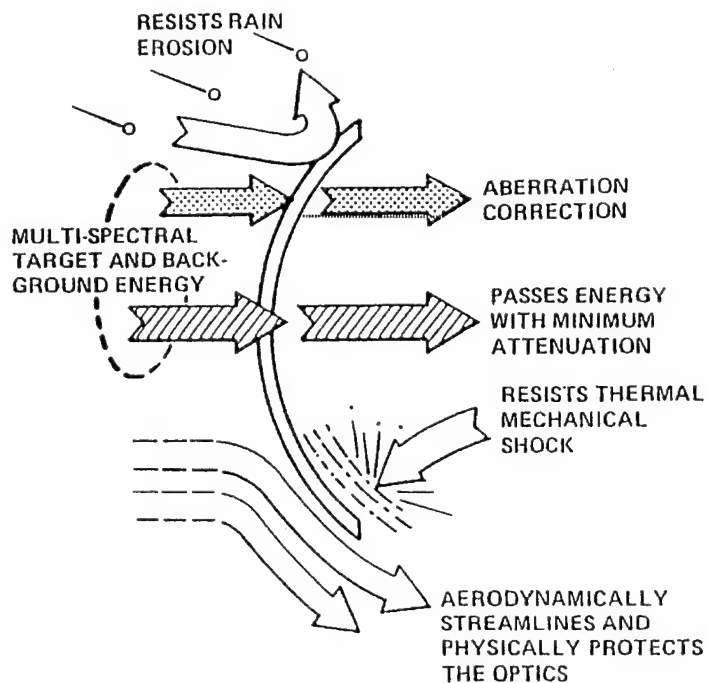


Figure 1-1. Infrared Dome Design Constraints

II. BACKGROUND

A. BLUNT BODY STRUCTURE

A typical blunt-body, supersonic flow field is shown in Fig.2-1. This figure shows the general structure of the flow field in front of the window mounted at the nose of a supersonic vehicle. The shock wave is detached and normal shock relations may be used to estimate the change in density along the stagnation streamline. A complete flow field and shock-structure solution depends on body geometry and flight Mach number. Such solutions are complex because of mixed subsonic ($M < 1$) and supersonic ($M > 1$) regions in the flowfield. The governing equations are mathematically elliptical in the subsonic region and hyperbolic in the supersonic region. Time-dependent numerical techniques are used to determine flow fields surrounding blunt bodies[5]. An empirical formula for the shock stand-off distance, Δ , at the tip of a conical body with a hemispherical nose is

$$\Delta/R = 0.143e^{[3.24/M_\infty^2]} \quad (2-1)$$

where R is the nose radius. This equation shows that the shock standoff distance decreases with Mach number. In this formula it is assumed that the detached shock wave is a hyperbola that is asymptotic to the free stream Mach angle. The equation for the coordinates of the shock around a hemisphere-cone [6] is

$$x = R \cdot \Delta \cdot R_c \cot^2 \theta \left[\left(1 + \frac{y^2 \tan^2 \theta}{R_c^2} \right)^{1/2} - 1 \right]. \quad (2-2)$$

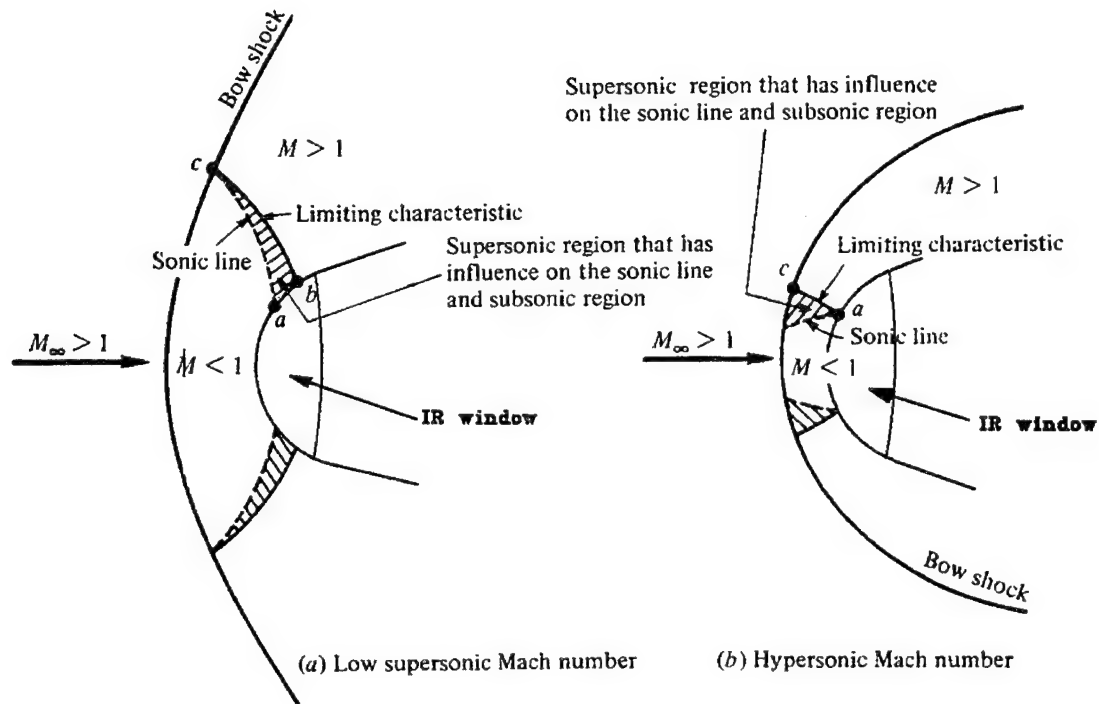


Figure 2-1. Illustration of the flow field in front of the missile's nose.

B. AERODYNAMIC HEATING AND HEAT TRANSFER

1. The Heat Transfer Process

A vehicle operating at supersonic conditions is heated by heat generated within the boundary layer that surrounds it. Heat is produced by the conversion of kinetic energy through flow deceleration in the boundary layer, as shown in Fig.2-2. Heat is transferred to the body surface by conduction which is represented by Fourier's law of heat conduction given by [7]

$$\dot{q} = -k \left(\frac{\partial T}{\partial Y} \right)_{Y=0} \quad (2-3)$$

where the temperature gradient in the boundary layer is evaluated at the wall.

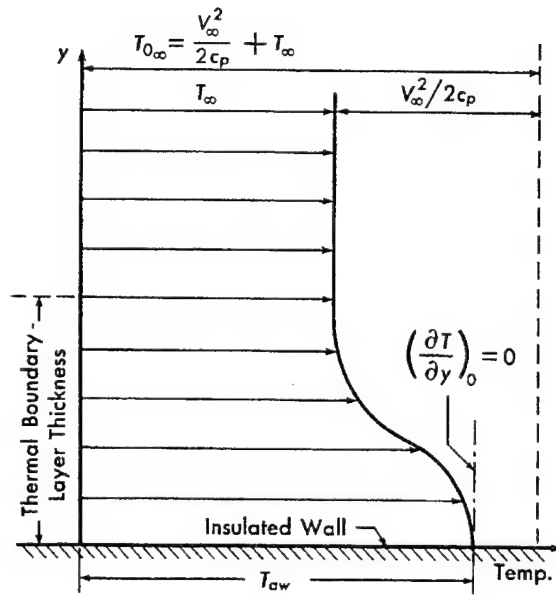


Figure 2-2. Thermal boundary layer temperature distribution near insulated wall [8].

Thermal diffusion by conduction is a complex three-dimensional problem. The solution of this problem requires the formulation of an energy balance which considers the thermal energy stored at each point in the structure as well the thermal energy conducted. In rectilinear coordinates this energy balance is given as follows:

$$\frac{\partial T}{\partial t} \cdot \alpha \left(\frac{\partial^2 T}{\partial x^2} + \frac{\partial^2 T}{\partial y^2} + \frac{\partial^2 T}{\partial z^2} \right) \quad (2-4)$$

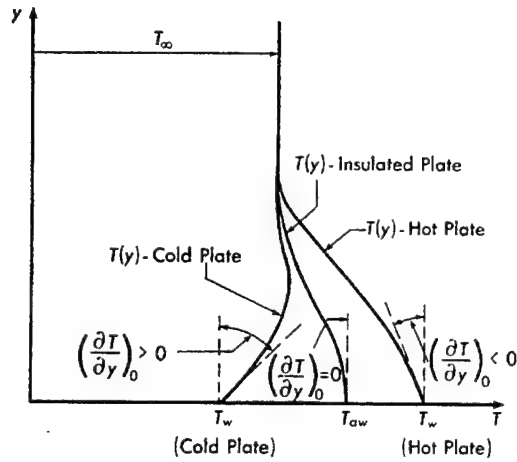


Figure 2-3. Effect of heating and cooling on temperature distribution [8].

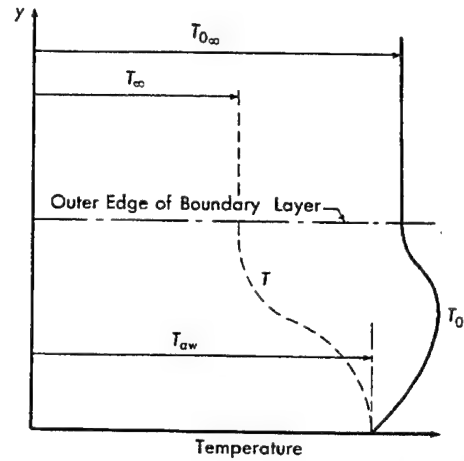


Figure 2-4. Distribution of temperature near insulated wall [8].

In practice heat transfer is computed using finite differences and finite element methods for heat conduction. At elevated temperatures a surface will lose heat to its surroundings by radiation according to the Stefan-Boltzmann law, given by

$$q_{rad} = \epsilon \sigma (T_w^4 - T_{BG}^4) \quad (2-5)$$

where $\sigma = 5.67 \times 10^{-8} \text{ Wm}^{-2} \text{ K}^{-4}$ and ϵ is the surface emissivity having values between 0 and 1 depending on the material, T_{BG} is the background temperature at which the background radiates back to the surface. There is also the possibility of radiating from the skin of the vehicle to its own internal structure. While the form of the Stefan-Boltzmann law is the same, the temperatures of the radiating surfaces and non-gray absorption and emission must be considered.

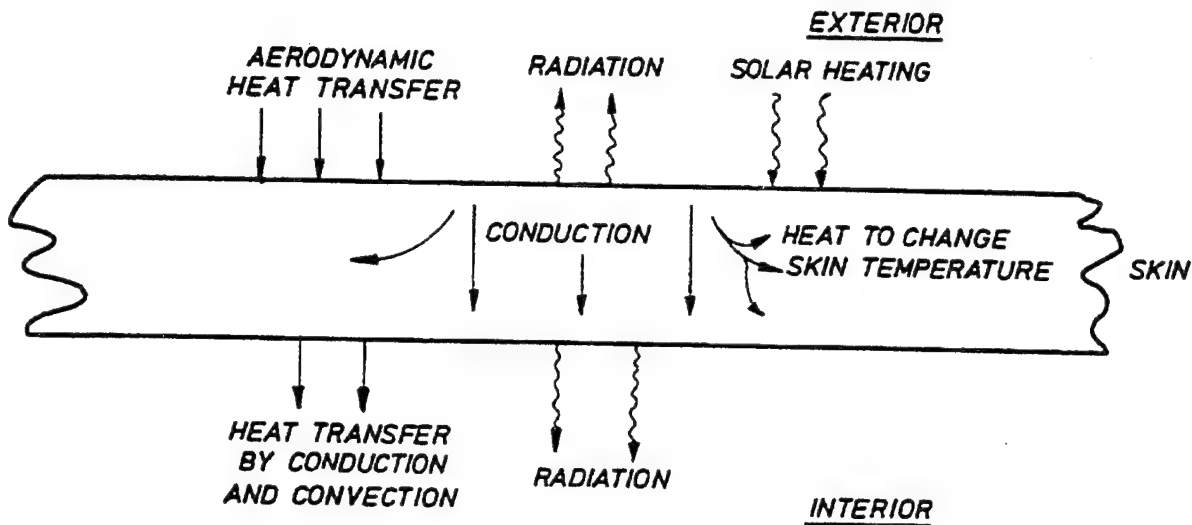


Figure 2-5. Heat transfer modes.

2. Recovery Temperature

It is important to note that in gases the adiabatic wall temperature is always less than the free-stream stagnation temperature, T_{∞} . This condition is in contrast to what one may expect from the well-known temperature-Mach number relation

$$\frac{T_1}{T_2} = \frac{1. [(\gamma-1)/2] M_2^2}{1. [(\gamma-1)/2] M_1^2} \quad (2-6)$$

Viscous effects within the boundary layer decrease the velocity from the freestream value at the outer edge of the boundary layer to zero at the surface. Pure compression heating would give a stagnation temperature of

$$T_{O_{\infty}} = T_{\infty} \left(1 + \frac{\gamma-1}{2} M_{\infty}^2 \right) \quad (2-7)$$

at the surface (that is, in Eq. 2-6 let $T_1 = T_{O_{\infty}}$ and $T_2 = T_{\infty}$. Then

$M_1 = 0$ and $M_2 = M_\infty$). T_{∞} is the value of temperature where the velocity is zero, i.e., at the stagnation point. On the other hand, in continuum flow the velocity at the wall is zero, but as already stated, the adiabatic wall temperature is always less than the free-stream stagnation temperature T_{∞} .

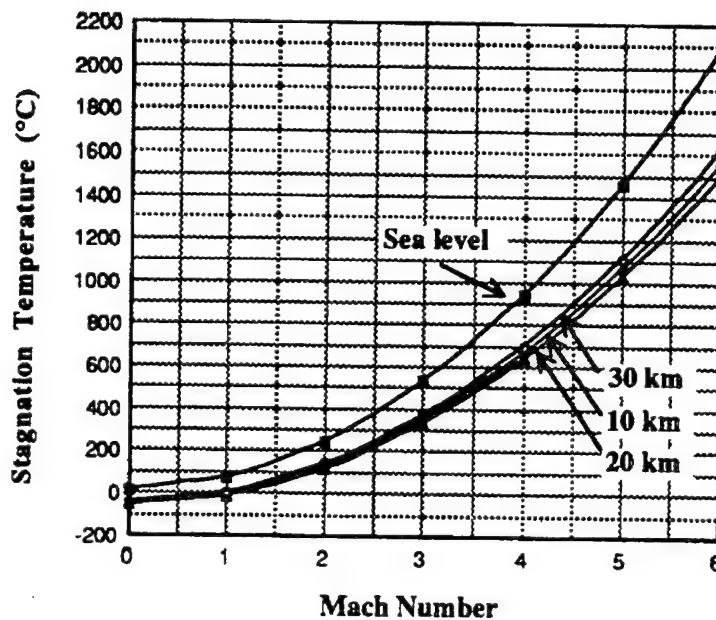


Figure 2-6. Stagnation temperature versus Mach number at several altitudes[9].

In practice, heat is conducted outwards through the boundary layer. Viscous dissipation produces additional heat and the actual temperature reached at the surface (assuming no heat transfer into the surface) is called the *recovery temperature*[8]. Therefore, for practical computations, it is convenient to define a quantity known as the recovery factor, r , which is a measure of the fraction of the local free-stream dynamic-temperature rise recovered at the wall:

$$T_{aw} = T_{\infty} \left(1 + r \frac{\gamma - 1}{2} M_{\infty}^2 \right) \quad (2-8)$$

Using the simple energy equation

$$c_p T_{aw} = \frac{V_{\infty}^2}{2} + c_p T_{o\infty} \quad (2-9)$$

where c_p is the specific heat at a constant pressure and V_{∞} is the free-stream velocity, other forms of the recovery factor may be written as

$$r = \frac{T_{aw} - T_{\infty}}{V_{\infty}^2 / 2c_p} = \frac{T_{aw} - T_{\infty}}{T_{o\infty} - T_{\infty}} = \frac{2}{(\gamma - 1) M_{\infty}^2} \left(\frac{T_{aw}}{T_{\infty}} - 1 \right) \quad (2-10)$$

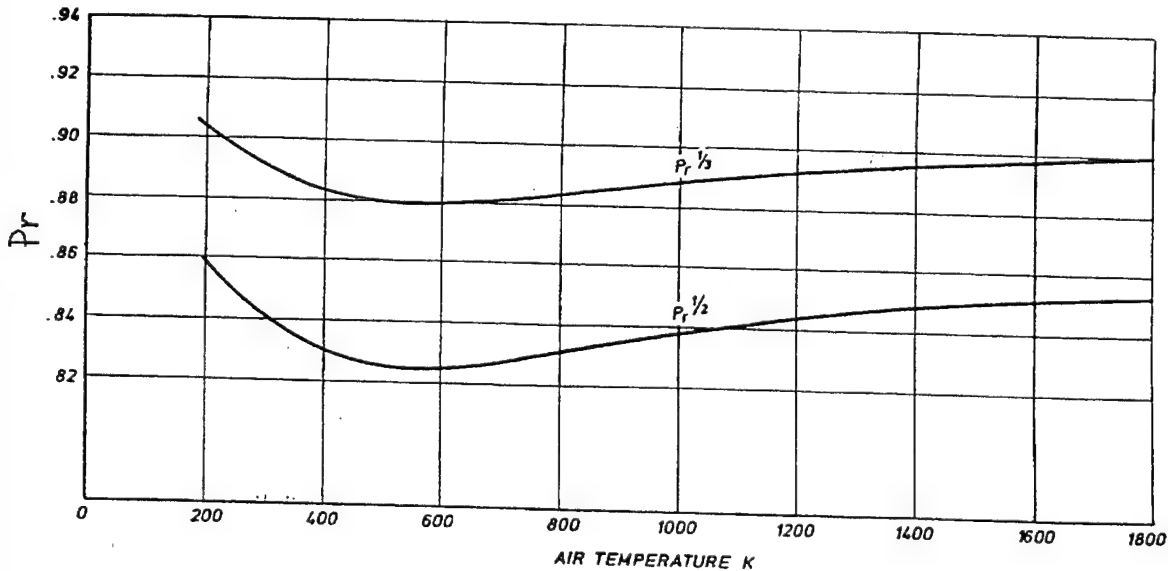


Figure 2-7. Prandtl number plot for several operational conditions.

It is obvious that if the entire plate is adiabatic, energy considerations dictate that the mean stagnation temperature with respect to mass flow must be equal to the free-stream stagnation temperature T_{ow} . Since the wall temperature is less than T_{∞} , it follows that the distribution of stagnation temperature within the boundary layer must be of the form shown in Fig.2-4, with some portion of the boundary layer having a stagnation temperature greater than T_{∞} .

The value of the recovery factor depends upon Prandtl number Pr which is a ratio measuring the effects of conduction and dissipation mentioned above. The Prandtl number is defined by

$$Pr = \frac{\mu C_p}{k} \approx 0.71 \text{ for air at N.P.T.} \quad (2-11)$$

where μ is the coefficient of viscosity and k is the thermal conductivity. These coefficients are strongly temperature dependent and graphs showing this dependence are drawn in Fig.2-7. It can be shown that the recovery factor is approximated in terms of the Prandtl number:

$$r = Pr^n \quad (2-12)$$

where $n=1/2$ for laminar flow and $n=1/3$ for turbulent flow. While this is a useful approximation, the recovery is also a function of the pressure gradient and local Mach number.

The adiabatic wall temperature is then given by an equation such as

$$T_r = T_e + r \left(\frac{U_e^2}{2C_p} \right) \quad (2-13)$$

where U_e is the velocity at the edge of the boundary layer and c_p is the specific heat.

In missile flight the dome is subjected to aerodynamic heating resulting from the convective heat-transfer process described by the equation

$$h = \frac{q}{T_r - T_w} \quad (2-14)$$

where T_w is the wall temperature and T_r the recovery(adiabatic) wall temperature. The adiabatic wall temperature is that temperature at which the heat-transfer to the wall is zero, i.e., where the temperature gradient in the boundary wall is zero, as shown in Fig.2-3. The heat-transfer coefficient is the ratio of the heating rate to the thermal driving potential.

The heat transfer coefficient h in Eq.(2-14) varies considerably with flight conditions. It is often more convenient to work with a non-dimensional heat transfer coefficient called the Stanton number defined by:

$$St = \frac{h}{\rho_e u_e c_p} \quad (2-15)$$

Stanton number and skin friction coefficient are linked by the Reynolds analogy

$$St = \frac{C_f S}{2} \quad (2-16)$$

where C_f is the skin-friction coefficient and S is the analogy factor.

3. Heat Transfer to a Hemisphere

The aerodynamic flow over a hemispherical nose is laminar at the stagnation point. As the air accelerates in passing from the stagnation point to the base of the hemisphere, it can go through transition, and the boundary layer generally becomes turbulent. This, happens at Reynolds numbers around 4×10^5 [2].

For the laminar case, Sibulkin has shown that locally the Stanton number on a hemisphere stagnation point can be written

$$St = 0.763 \left(\frac{c_p \mu}{k} \right)^{0.6} \left(\frac{\beta D}{u} \right) \left(\frac{\rho u_\infty D}{\mu} \right) \quad (2-17)$$

where D is the diameter of the hemisphere, β is the velocity gradient and μ is the viscosity.

All of the fluid properties are evaluated at the local conditions just outside the boundary layer. In the case of stagnation this corresponds to stagnation temperature and Pitot pressure. This reduces Eq.(2-17) to[2]

$$St = \frac{9.37}{\sqrt{Re} \sqrt{u/D}} \left(\frac{M^2}{M^2.5} \right)^{0.25} \left(1. \frac{M^2}{5} \right)^{0.38} \quad (2-18)$$

where $(c_p \mu / k_\infty)_{s.p.}$ is the stagnation Prandtl number (approximately 0.72 for normal flight conditions), $\rho_\infty u D / \mu_\infty$ is the free-stream Reynolds number based on hemisphere diameter. The subscript o refers to total or stagnation values.

From Ref [1],

$$St = 0.763 \left(\frac{\beta D}{u} \right)^{1/2} \left(\frac{\rho_\infty u D}{\mu_\infty} \right)^{-1/2} \left(\frac{c_p \mu}{k_\infty} \right)^{-0.6}_{s.p.} \left(\frac{\rho_o}{\rho_\infty} \right)^{1/2} \left(\frac{\mu_o}{\mu_\infty} \right)^{1/2} \quad (2-19)$$

The subscript o denotes the total or stagnation value after the air passes through the shock wave. If it is assumed that $\mu \propto T^{0.76}$ and the perfect gas equations are used then Eq.(2-18) reduces to the general laminar Stanton number equation. This gives the heat-transfer rate at the stagnation point where the recovery factor, r ,

$$h_{st} \sqrt{2R} = 1.7 c_p \sqrt{\rho_\infty \mu_\infty} M_\infty (1.0.2 M_\infty^2)^{0.1} \quad (2-20)$$

equals 1. The laminar heat-transfer rate decreases away from the stagnation point. At the stagnation point another semi-empirical formula can be used to calculate the heat transfer[4]

From this formula C. Klein showed that the most severe thermal environment in terms of temperatures does not correlate with the highest thermal-flux situation[4].

When the boundary layer is turbulent, the Stanton number has a maximum at about 40° from the stagnation point, then decreases

further aft.

As shown from the Eq.(2-7) at supersonic speeds the temperatures reached are quite high, which raises the issue of suitability of certain materials as IR transmissive materials in a high temperature environment. However, it must be determined first whether the time frames are such that the surface temperatures can approach stagnation-type limits. For that purpose, one may consider the dimensionless Biot number

$$Bi = \frac{hL}{k_w} \quad (2-21)$$

which characterizes the transfer of heat across the boundary layer in relation to the dome's ability to transport heat. Here L represents the dome thickness. If the wall is thermodynamically thin, i.e., $Bi \ll 1$ and the radiation and conduction losses are negligible, then the aerodynamic heat-transfer rate can be equated to the rate of enthalpy increase within the wall, or

$$h(T_f - T_w) = \rho_w b_w c_{pw} \left(\frac{dT_w}{dt} \right) \quad (2-22)$$

where ρ_w represents the window density and c_{pw} the heat capacity of the window.

If there is a step change in the aerodynamic conditions, e.g. velocity (thus a step change in h and T_f), the solution is

$$\frac{T_r - T}{T_r - T_i} = \exp \left[- \left(\frac{h}{\rho_w c_{p_w} L} \right) t \right] \quad (2-23)$$

where T_i equals the initial temperature at $t = 0$. At higher Mach numbers (higher window temperatures), the radiation heat transfer plays a significant part. If this is to be considered, the heat-balance equation becomes

$$h(T_r - T_w) = \rho_w L c_{p_w} \frac{dT_w}{dt} + \sigma \epsilon(T) T_w^4 \quad (2-24)$$

The Eq. (2-24) can be solved for a series of constant temperatures to yield a more accurate temperature history. The true equilibrium temperature ($dT/dt=0$) can also be found from the same equation.

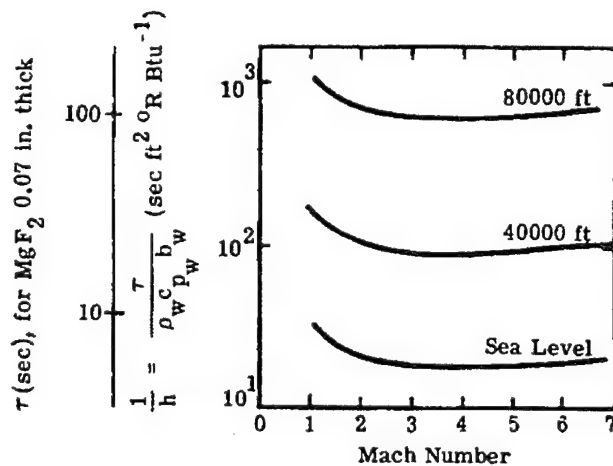


Figure 2-8. Time constant for aerodynamic heating[2].

Eq.(2-25) is used to give an indication of the relative rate of temperature increase. The equation for a time constant, τ , is

$$\tau = \frac{\rho_w c_p L}{h_{st}} \quad (2-25)$$

and gives the time to reach equilibrium

$$\frac{T_r - T}{T_r - T_i} = \frac{1}{e} \approx 0.368 \quad (2-26)$$

in the absence of radiation. In Fig.2-8 the generalized time constant for an arbitrary set of conditions, and a typical material, MgF_2 , 0.07 in. thick, is used to get a specific time constant. For 1 mm thick diamond domes, the heat transfer coefficient at the stagnation point leads to very small Biot numbers, which in turn suggests thermal time constants of the order of 1 sec at very high altitudes. In these conditions, for flight times of about 10 seconds or more, diamond missile domes will indeed reach the recovery temperature[4].

C. AEROSTRUCTURE OF THE INFRARED DOME

As will be discussed in later sections, the self emission of the dome window, due to the high temperatures induced by aerokinetic heating, is an aero-optical effect that will have a major influence on the sensor performance in a high speed flight situation. Dome emission is going to depend on the emissivity of the dome material among other variables. An accurate prediction of the dome emissivity

should consider the thickness of the dome. Therefore a discussion of the calculation of IR dome thickness is relevant. The dome's ability to withstand the thermal shock induced by transient heating on a fly-out trajectory is one of the major problems encountered in the design of high supersonic IR seeker domes. The subject of thermal shock resistance of IR domes has been very well characterized and analysed by Dr. Claude Klein. The following sub-sections summarize some of his published work on the subject[4][10][25].

1. Thermal Shock Resistance of the IR Dome

One of the most constraining factors in the design of IR missile window domes is the one attributed to brittle fracture caused by thermal shock[10]; the fracture is induced by tensile stresses on the "cold" side corresponding to the inner surface of the dome. These stresses are caused by the sudden temperature gradients generated by aerodynamic heating, which in conjunction with thermal expansion, produce compressions on the outer surface and tensions on the inside.

Starting with the expression for the maximum stress experienced by a clamped plate, or a complete sphere,

$$|\sigma_{\max}| = \frac{\alpha E}{2(1-\nu)} \Delta T, \quad (2-27)$$

if there is a linear temperature variation across the thickness and if both are free to expand:

$$\Delta T = |T_{ow} - T_w| \quad (2-28)$$

where ΔT refers to the temperature difference between the outer and

where ΔT refers to the temperature difference between the outer and inner surfaces. In a transient situation, ΔT is a strong function of time and depends critically upon the heat-transport process as characterized by the Biot number, Bi . If the condition $Bi < 1$ applies, ΔT peaks when the backface temperature starts to rise, which occurs long before the front reaches the stagnation temperature, and, thus, leads to

$$\Delta T_p = (T_{st} - T_{iw}) (Bi)_{st}. \quad (2-29)$$

In a first approximation, therefore, a thermally-thin dome will be subjected to a peak stress that amounts to [10]

$$|\sigma_{\max}|_p = \frac{\alpha E}{2(1 - \nu)} (Bi)_{st} (T_{st} - T_{iw}) \quad (2-30)$$

where $(Bi)_{st}$ refers to the Biot number at the stagnation point, T_{st} is the relevant stagnation temperature, and T_{iw} must be set equal to the wall temperature at the onset of the shock. Assessing the thermal shock resistance (TSR) then boils down to comparing $|\sigma_{\max}|_p$ with the allowable flexural stress, $\sigma_f/4$, which is best done by defining TSR as follows:

$$TSR = 10 \log \left[\frac{\sigma_f/4}{|\sigma_{\max}|_p} \right] \quad (2-31)$$

if the results are to be quantified. The stress ratio can be expressed as a product of three terms,

$$\frac{\sigma_f/4}{|\sigma_{\max}|_p} \cdot \frac{\sigma_f (1-\nu) k}{\alpha E} \cdot \frac{1}{h_{st} L} \cdot \frac{1/2}{T_{st} - T_{iw}} \quad (2-32)$$

The first term involves intrinsic material properties only, the second term depends upon both the diameter of the dome (through the heat transfer coefficient) and its thickness, while the third term reflects the severity of the aerothermal environment.

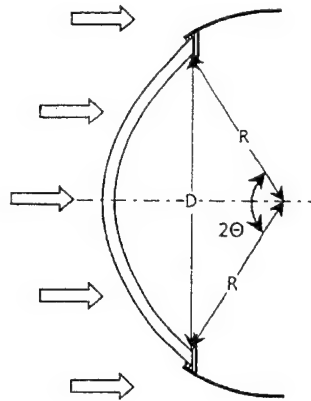


Figure 2-9. Schematic of a dome configuration[10].

2. Pressure Induced Stresses

At Mach numbers $M_{\infty} \geq 3$, the pressure distribution on a spheroidal shell varies essentially as the cosine square of the stagnation angle, which implies that, for worst-case type calculations, we may assume that the aerodynamic pressure on a truncated hemisphere is uniform and equal to the stagnation pressure p_{st} . In high supersonic flight, a fully vented IR dome as in Fig. 2-9, must, therefore, be able to withstand a pressure load[10]

$$\Delta p = p_{st} - p_{\infty} = p_{\infty} [(p_{st}/p_{\infty}) - 1] , \quad (2-33)$$

where p_{st}/p_{∞} refers to the pressure ratio across the bow shock and along the stagnation streamline:

$$\frac{p_{st}}{p_{\infty}} = \left[\left(\frac{\gamma+1}{2} \right) M_{\infty}^2 \right]^{\frac{\gamma}{\gamma-1}} \left[\left(\frac{2\gamma}{\gamma+1} \right) M_{\infty}^2 - \frac{\gamma-1}{\gamma+1} \right]^{\frac{1}{\gamma-1}} . \quad (2-34)$$

The external pressures give rise to a complex stress pattern that reflects the nature of the edge attachment, i.e., the stiffness of the dome interface with the support ring. Two limiting cases will be considered[10]; (a) the simply supported shell that is free to bend when subjected to the action of a uniform normal pressure, and (b) the shell with built-in (or clamped) edges that is restrained from moving in the "radial" direction. For simply supported shells, the maximum stress induced by bending, σ_{max} , is tensile and obeys the equation

$$\frac{\sigma_{max}}{\Delta p} = \frac{R}{2L} \left[\left(1.6 + 2.44 \sqrt{\frac{R}{L}} \sin(\theta) \right) \cos(\theta) - 1 \right] , \quad (2-35)$$

provided the dome aspect ratio, L/R , satisfies the condition

$$\frac{\sin^2(\theta)}{12} \leq \frac{L}{R} \leq \frac{\sin^2(\theta)}{1.2} , \quad (2-36)$$

where θ designates the hemisphere truncation angle (see Fig.2-9). For edge-constrained shells, the predominant stress is compressive and localized at the base of the dome, near the interface. It

relates to the aspect ratio of the dome in a very simple relation

$$\frac{\sin^2(\theta)}{12} \leq \frac{L}{R} \leq \frac{\sin^2(\theta)}{3} , \quad (2-37)$$

if the condition

$$\frac{\sigma_{max}}{\Delta p} \leq 1.2 \frac{R}{L} \quad (2-38)$$

is met. Evaluating Eq.(2-35) for several angles θ shows that, on a relative scale, the bending stress depends solely on the wall thickness (the stress increases as the thickness decreases) and can be approximated by means of the relation

$$\frac{\sigma_{max}}{\Delta p} \approx 0.581 \left(\frac{L}{R} \right)^{3/2} \quad (2-39)$$

as long as the conditions (2-37) are satisfied. It is also seen that this stress represents a worst case in the sense that constraining the edge displacement would decrease the stresses, especially for low aspect ratio domes. Because of the thermal expansion mismatch at the interface of the infrared dome and its support structure, a "floating" attachment scheme that decouples the dome from the missile body would be desirable, and such optimized attachment should result in pressure-induced tensile stresses as given by Eq.(2-39). The maximum tensile stresses failure criterion, *i.e.*,

$$\sigma_{max} \leq \frac{\sigma_f}{SF} \quad (2-40)$$

where σ_f refers to the nominal flexure strength of the dome material,

and SF is an appropriate safety factor, then yields the minimum thickness required to prevent fracture. Since currently available IR transmitting dome materials are brittle ceramics, they may exhibit a wide range of fracture probabilities under apparently identical loadings, which suggests safety factors of at least four (4) if σ_f is the characteristic flexural strength derived from Weibull statistical analysis. It is concluded that the dome thickness required for withstanding a pressure load Δp with good probability of survival can be obtained from the following equation:

$$\frac{L_{min}}{R} = 1.75 \left(\frac{\Delta p}{\sigma_f} \right)^{2/3} \quad (2-41)$$

D. RADIATION PROPERTIES OF SURFACES

In analysing the interchange of radiant energy among surfaces, it is necessary to know their emission, reflection, and absorption characteristics. Besides the obvious need for transparency, a critical requirement for an IR window in a hot environment is that it emits little radiation that would obscure the scene being viewed. In the next sections the emission properties of windows will be explored.

1. Radiometry

In describing the directional transport of energy, it is convenient to deal with the *radiant energy* (in joules) contained within a small solid angle $d\omega$. This naturally leads to the concept of the *radiant intensity*. The *radiant flux*, ϕ (in watts) emitted per unit solid angle(ω) by a point source in a given direction is

called *radiant intensity*, I , and is given by[19]

$$I = \frac{d\Phi}{d\omega} \quad [W/sr] . \quad (2-42)$$

Another useful radiometric term is the *radiant flux density* at a surface, measured in watts per square meter. It may be either emitted from a surface, in which case it is called *radiant exitance*, M , or incident onto a surface, in which case is called *irradiance*, E .

The inverse-square law of radiation from a point source is derived by calculating the irradiance of a point source on a spherical surface surrounding the point, of solid angle 4π sr and surface area $4\pi r^2$. Hence

$$E = \frac{\Phi}{A} = \frac{4\pi I}{4\pi r^2} = \frac{I}{r^2} . \quad (2-43)$$

The *radiance*, L , represents the radiant energy per unit time and unit surface area that passes through a solid angle $d\omega$ inclined at an angle θ with respect to the surface normal. This situation is represented in Fig. 2-10. The radiance is given by

$$L = \frac{dI}{(dA \cos\theta)} \quad [W/m^2 \cdot sr] . \quad (2-44)$$

In the case of spectral quantities (wavelength-dependent distribution), a subscript λ is affixed to the radiometric quantities, whereas for total radiation these subscripts are omitted. In general, the direction of the intensity is specified by angles θ and ϕ of a spherical surface as shown in Fig. 2-10. In the

case of a *Lambertian* surface, the intensity for a certain radius of the surface varies in accordance with the following relation,

$$I(\theta) = I(0) \cos \theta . \quad (2-45)$$

In this case the radiance is independent of the viewing angle, and the surface is said to be perfectly diffuse. The intensity distributions are related to the corresponding hemispherical radiation fluxes by integration over the hemisphere surrounding the surface. As an example, for a flat surface, the radiant power Φ leaving the surface is connected with the radiant intensity at the surface as follows:

$$\Phi = \int_{\text{hem}} I(\theta) \cos \theta \, d\omega \quad [W] \quad (2-46)$$

in which the subscript 'hem' denotes the hemisphere. Similar relationships apply for the incident and reflected radiant fluxes.

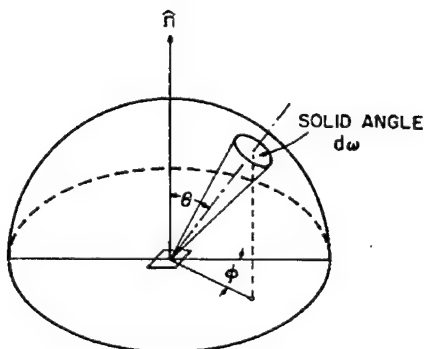


Figure 2-10. Angle Notation.

2. Blackbody Radiation

The ideal blackbody is a perfectly efficient and diffuse emitter of radiant energy. No body at the same temperature can emit more radiation at any wavelength or into any direction than can a blackbody at the same temperature. It follows that a blackbody is also a perfect absorber: all radiation incident on a blackbody will be absorbed regardless of wavelength or angle of incidence. The spectral radiant exitance M_λ of a blackbody is given by the Planck equation,

$$M_\lambda = \frac{2\pi hc^2}{\lambda^5} \left[\frac{1}{e^{hc/\lambda kT} - 1} \right] \quad (2-47)$$

where the physical constants h , c , and k represent the Planck constant, the speed of light, and the Boltzmann constant respectively. After substituting the values of these constants in the Planck equation, the result is

$$M_\lambda = \frac{3.745 \times 10^4}{\lambda^5} \left[\frac{1}{e^{14388 / \lambda T} - 1} \right] \quad [W \cdot cm^2 \cdot \mu m^{-1}] \quad (2-48)$$

where λ is in micrometers and T is in kelvins. The spectral radiant exitance for three background temperatures is plotted in Fig. 2-11.

The peak exitance, λ_{max} shifts toward shorter wavelengths with increasing temperature according to the *Wien displacement law*, expressed as

$$\lambda_{max} T = \frac{hc}{5k} = 2.88 \times 10^3 \quad [\mu m \cdot K] \quad (2-49)$$

Integration of the spectral radiant exitance of Eq.(2-47) over all

wavelengths gives the *total radiant exitance* given by

$$M \cdot \sigma T^4 \quad (2-50)$$

known as the *Stefan-Boltzmann law*, with σ as the Stefan-Boltzmann constant, equal to $5.67 \times 10^{-8} \text{W/m}^2 \cdot \text{K}^4$.

The *emissivity* ε expresses quantitatively the fact that real surfaces always emit less radiation than a blackbody. The blackbody emissivity is expressed as the ratio of the total radiant exitance of the body to the total radiant exitance of a blackbody at the same temperature,

$$\varepsilon(T) = \frac{M}{M_{BB}} \quad (2-51)$$

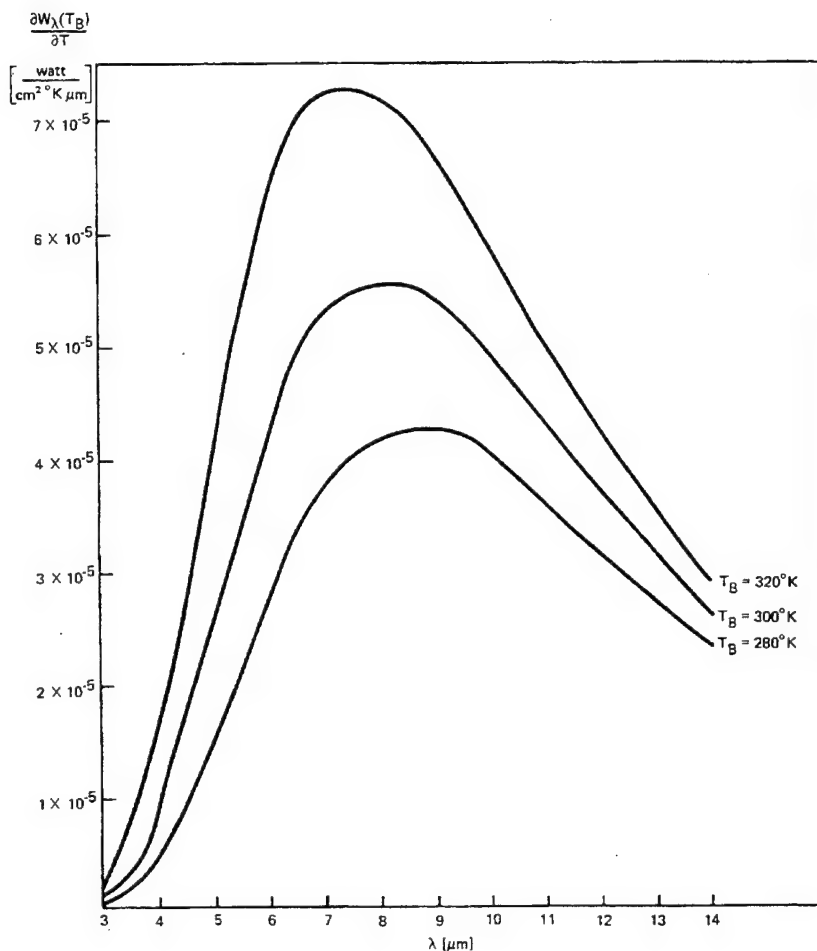


Figure 2-11. Blackbody radiation spectral distribution at three background temperatures[20].

3. Directional Emissivity

The angular emissivity is defined as the ratio of the radiance in a particular direction to the radiance of a blackbody in that same direction. In general, for arbitrary surface conditions, the distribution of the emitted radiance L depends on two angles θ and ϕ as shown in Fig. 2-10. On the other hand, the blackbody radiance

L_{BB} is uniform. Consequently, one can write

$$\varepsilon(T, \theta, \phi) = \frac{L}{L_{BB}} = \varepsilon . \quad (2-52)$$

Eq.(2-52) states that, for a diffuse surface, the directional emissivity is *independent of angle* and is equal to the hemispherical emissivity.

The directional emissivity characteristics of real surfaces are revealed by measurements performed on a variety of materials by E. Schmidt and E. Eckert[11]. One of their measured distributions is reproduced in Fig. 2-11. The figures are in the form of polar diagrams in which the concentric circles are contours of constant emissivity ε and the radial lines are contours of constant angle θ . The surfaces employed in the experiments were presumably isotropic, and no dependence on the angle ϕ is indicated. The temperatures of the various test surfaces were typically a few hundred degrees Fahrenheit. The directional emissivity results were determined from total radiation measurements.

Figure 2-11 shows that, for nonmetals, the directional emissivity remains essentially uniform for inclination angles between 0° and $50-60^\circ$; then it drops off quite rapidly to zero. In the region of near uniformity, the emissivity values are in the range from 0.8 to 0.95, which is typical for dielectrics.

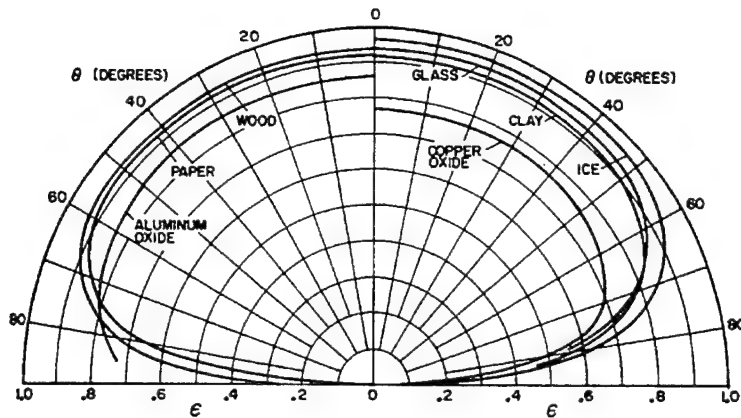


Figure 2-12. Distribution of the total directional emittance for several dielectrics[11].

The directional emissivity characteristics displayed by metallic surfaces are somewhat different from those just discussed. In the range of angles between 0° and $30-40^\circ$, ε remains quite uniform. However, at larger angular inclinations ε increases quite sharply. The percentage increase is more pronounced when the level of emissivity is low. At angles approaching 90° the directional emissivity should approach zero.

The directional absorptivity is the fraction of the radiant energy incident on the surface from a specific direction that is absorbed. In accordance with Kirchhoff's law, the directional monochromatic absorptivity and the directional monochromatic emissivity are equal provided that the incident beam is uniformly polarized. That is,

$$\alpha_{\lambda}(\theta, \phi) = \varepsilon_{\lambda}(\theta, \phi) . \quad (2-53)$$

4. Optical Properties of Dielectric Window Materials

In the infrared, there are two main contributors to the complex index of refraction of insulating ceramics. They are electronic transitions and lattice vibrations or phonons (a quantized packet of vibrational energy)[12]. The electronic transitions contribute to the real part of the index of refraction only in the form of a frequency-independent parameter with weak temperature dependence. Most of the frequency and temperature dependence of the complex index of refraction at mid-infrared frequencies comes from phonons.

Single-phonon absorption processes are due to the excitation of a phonon upon the absorption of a photon. These processes are very strong, since the photons can couple directly to the fundamental lattice vibrations of a material. Multiphonon absorption processes are due the excitation of more than one phonon upon absorption of a photon. These processes become important in the transparent regions of a material where one-phonon absorption processes do not dominate. Difference bands of multiphonon absorption occur in the millimeter spectral region, and sum bands occur in the infrared region. Sum band processes typically dominate infrared emissivity[12].

The behavior of the absorption coefficient and refractive index of a typical optical material is indicated schematically in Fig. 2-12. In general, materials absorb light strongly in the infrared and ultraviolet regions, near wavenumbers of 10^3 and 10^5 cm^{-1} , respectively, in the upper part of Fig. 2-13 [12]. Infrared

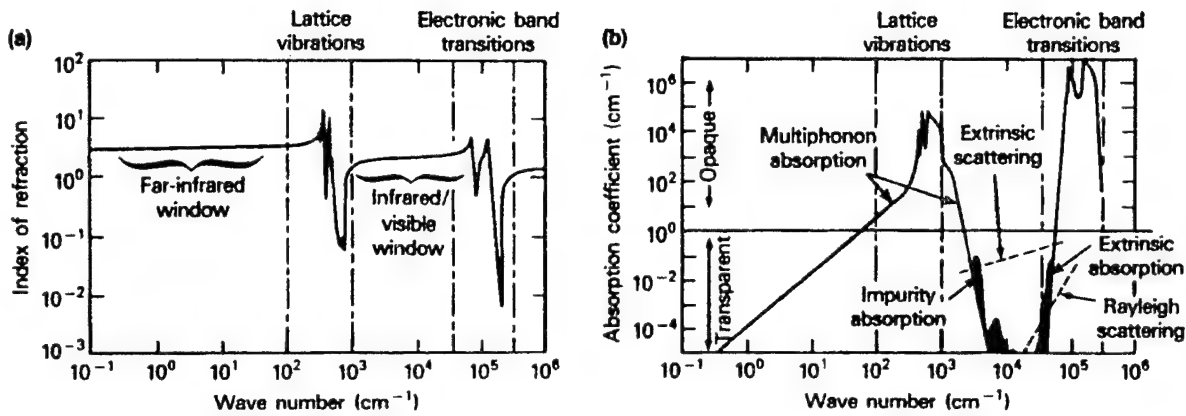


Figure 2-13. Absorption coefficient and refractive index of a typical optical window material. Adapted from Thomas[9].

radiation stimulates vibrations of the atoms in a solid at the characteristic *Reststrahlen* frequencies. Ultraviolet radiation promotes electrons from filled bands to higher energy unfilled bands. Between the two strong absorption regions is a window in which the material is transparent. The infrared edge of the window is called the *multiphonon region* because the transitions responsible for the weak absorption arise from multiple excitations of one or more vibrational modes (phonons). The ultraviolet edge of the window is called the Urbach tail.

The optical properties of non-magnetic dielectric window materials can be specified completely by the complex index of refraction, $n(\nu, T)$ or complex permittivity, $\epsilon(\nu, T)$ where ν is the wavenumber (reciprocal wavelength) and T is temperature[12]. The relationship between n and ϵ is

$$\mathbf{n}(\nu, T) = \sqrt{\epsilon(\nu, T)} = n(\nu, T) - ik(\nu, T), \quad (2-54)$$

where

$$\epsilon(\nu) = (n^2 - k^2) - 2ink - \epsilon_1 - i\epsilon_2, \quad (2-55)$$

n is the index of refraction, and k is the index of extinction.

The magnitude of the reflectance of the medium (at normal incidence) is

$$|R| = \frac{(n-1)^2 + k^2}{(n+1)^2 + k^2}. \quad (2-56)$$

The absorption coefficient is defined by

$$\beta_a(\nu, T) = 4\pi k(\nu, T). \quad (2-57)$$

The radiance from a material, $L_M(\nu, T)$, is expressed as

$$L_M(\nu, T) = \epsilon(\theta, \nu, T) L_{BB}(\nu, T) \quad (2-58)$$

where $\epsilon(\theta, \nu, T)$ is the spectral emissivity of the material, $L_{BB}(\nu, T)$ is the radiance of a blackbody, T is the temperature, ν is the spectral frequency and θ is the angle of incidence (i.e. the angle between the surface normal and the incident ray). In general, the emissivity is composed of two components: a specular and a diffuse component. For our purposes, the diffuse component is negligible

since the materials have smooth flat surfaces and negligible bulk scattering.

Based on the Stefan-Boltzmann law and Kirchoff's law of radiation, the specular component of emissivity can be expressed as[12]

$$\varepsilon_v(\theta, \nu, T) = \frac{(1 - R(\theta, \nu, T)) (1 - e^{-\beta_s(\nu, T)t/\cos\theta})}{1 - R(\theta, \nu, T)e^{-\beta_s(\nu, T)t/\cos\theta}}, \quad (2-59)$$

where R is the single-surface Fresnel power reflectance for unpolarized light, and t is the window thickness. In general ε_v and R have angular dependencies consisting of sine and cosine functions. Near normal incidence (i.e. near $\theta=0^\circ$), the angular dependencies of ε_v and R can be neglected, since the sine and cosine are approximately constant.

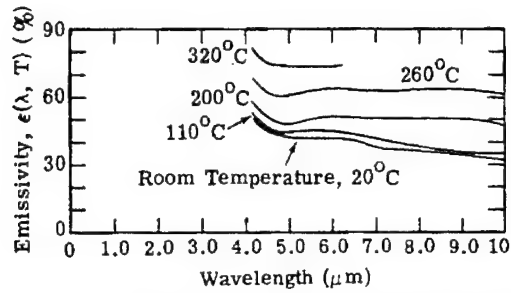
Usually, a measurement of $|R|$ is not sufficient to characterise ε . Therefore, it is convenient to describe the form of the complex permittivity. The classical pole-fit model represents the fundamental lattice vibrations or single-phonon transitions in a material. This feature is important in representing the index of refraction at all optical frequencies, but the absorption coefficient obtained from the model is valid only in the vicinity of the one-phonon frequencies. The absorption coefficient needs to be known in the region of transparency as well, requiring a description of multiphonon absorption bands in which more than one-phonon excitation occurs upon the absorption of a single photon.

E. DOME EMISSION AND EMISSIVITY AT HIGH TEMPERATURES

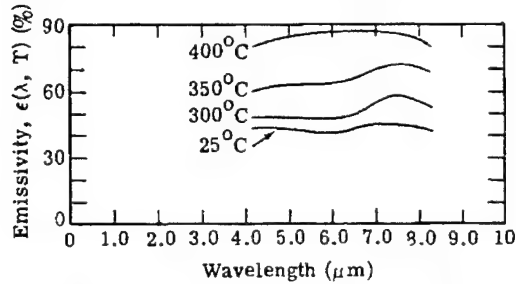
As the IR dome heats up, it will emit graybody radiation over the entire electromagnetic spectrum, which may adversely impact the operation of the seeker system in a high-speed flight situation [2][4][13]. It is recognized that saturation of the detectors by radiation from aerodynamically heated domes is not a major issue but the added background-induced noise will lower the signal-to-noise ratio for detection, decreasing the effective performance of the system in terms of detection range as well as tracking ability. An accurate prediction of the dome emission requires a good knowledge of the dome emissivity properties at the high operating temperature. The emissivity can be obtained by models or by experimental data.

The effect of temperature on the emissivity properties of several dome materials is shown in Fig. 2-14. The absorption edge of an infrared window material shifts to a shorter wavelength as the temperature increases (Fig. 2-14). This occurs as the weak absorptions present in this region begin to dominate.

When temperature of a material increases (see Fig. 2-15), so does its emissivity. Fig. 2-16 shows the effect predicted for sapphire[9]. As shown in Fig. 2-15 the sapphire window at 1000°C (1273 K) emits 7.4 times as much radiant energy as the same window at 500°C (773 K) if the emissivity is independent of T [9]. Near the absorption edge the emissivity increases with temperature, so the actual emission is even more than 7.4 times the lower temperature value.



(a) Germanium (single crystal, 1.14 mm thick)



(b) Silicon (single crystal, 4.16 mm thick)

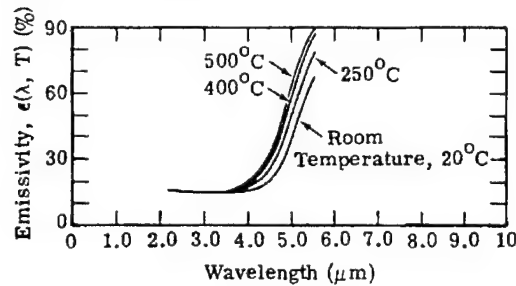


Figure 2-14. Emissivity of several dome materials[2].

At elevated temperatures, it is emission, not absorption, that limits the performance of an optical window.

Figure 2-17 shows the measured high-temperature spectral emissivity of a sapphire sample(Michael Thomas, APL[12]).

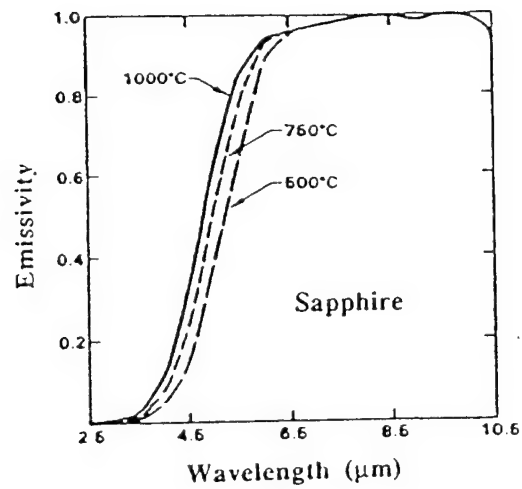


Figure 2-15. Saphire absorption coefficient as a function of temperature[9].

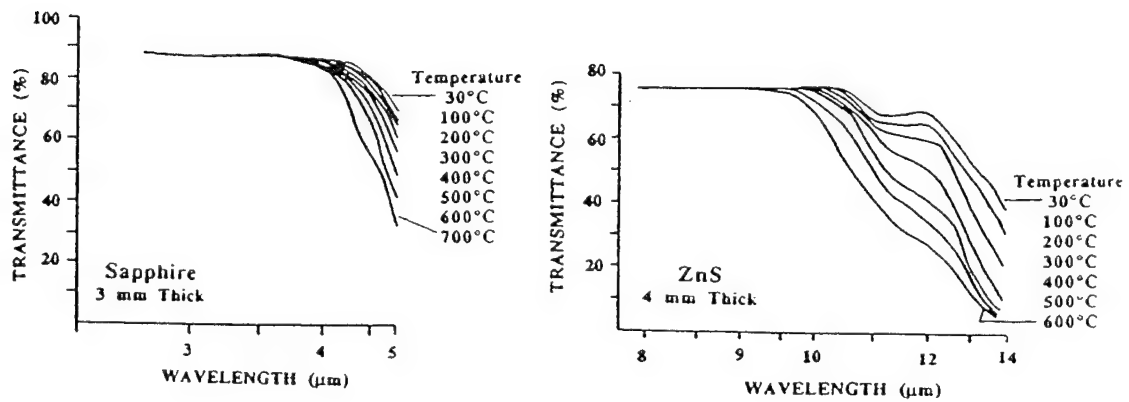


Figure 2-16. Temperature dependence of infrared transmission of zinc sulfide and sapphire[9].

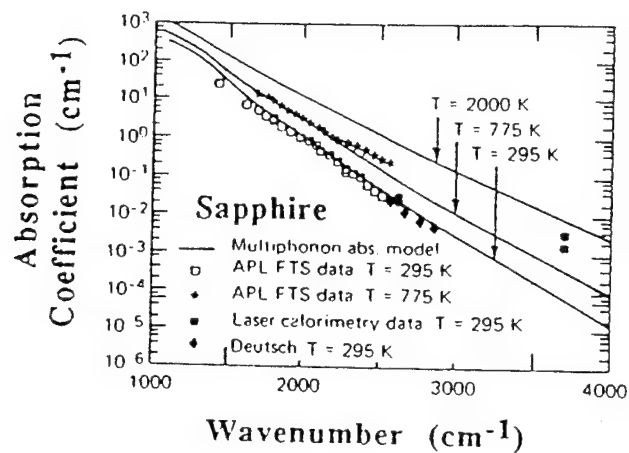


Figure 2-17. Emissivity of 0.20 cm thick sapphire calculated from measured absorption[9].

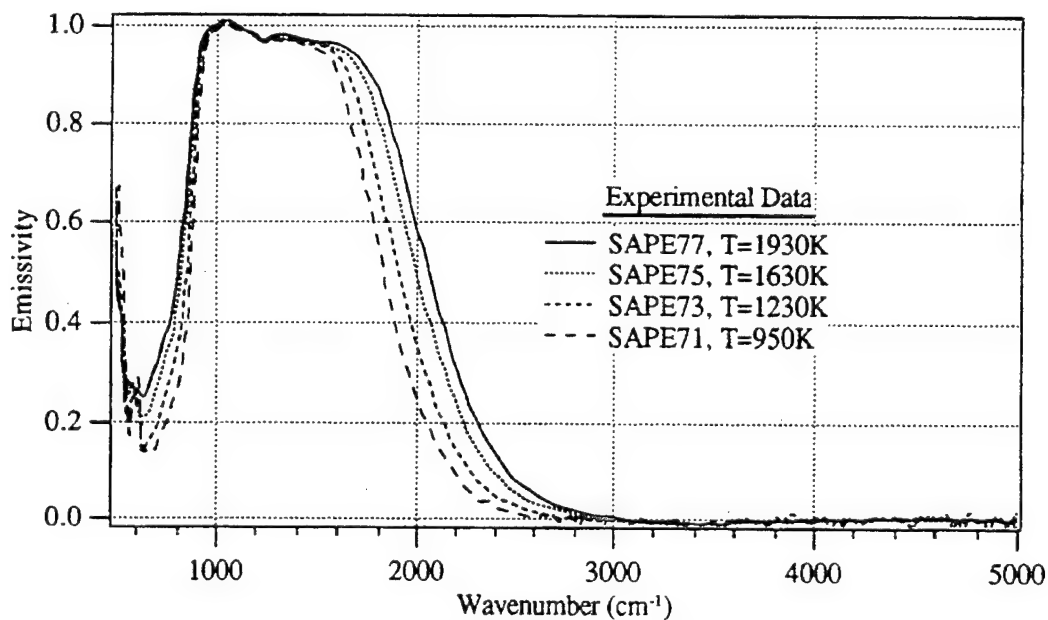


Figure 2-18. High-temperature spectral emissivity of a hemex grade sapphire o-ray sample (12.7 mm diameter, 1.0 mm thick) over the temperature range of 950 K to 1930K. [12].

III. GOVERNING EQUATIONS OF FLUID MECHANICS

In order to compute compressible viscous flow around a body, the continuity, momentum and energy equations must be solved simultaneously. Here the vector and the conservative-law form of the compressible Reynolds-averaged Navier-Stokes equation is presented.

A. CONTINUITY EQUATION

The continuity equation expresses the Conservation of Mass law. This law applied to a fluid passing through an infinitesimal control volume fixed in space yields the following equation of continuity

$$\frac{\partial \rho}{\partial t} + \nabla \cdot (\rho \mathbf{v}) = 0 \quad (3-1)$$

Here ρ is the fluid density and \mathbf{v} is the fluid velocity vector. Eq.(3-1) states that the net mass flux through a control volume surface must be equal to the time rate of change inside the control volume. For a three-dimensional Cartesian system, where u, v, w represent the x, y, z components of the velocity vector, Eq.(3-1) becomes

$$\frac{\partial \rho}{\partial t} + \frac{\partial}{\partial x} (\rho u) + \frac{\partial}{\partial y} (\rho v) + \frac{\partial}{\partial z} (\rho w) = 0 \quad (3-2)$$

B. MOMENTUM EQUATION

The momentum equation expresses Newton's second law as applied to a fluid element passing through an infinitesimal, fixed control volume in space. The momentum equation is:

$$\frac{\partial}{\partial t} (\rho \mathbf{v}) + \nabla \cdot \rho \mathbf{v} \mathbf{v} = \rho \mathbf{f} + \nabla \cdot \Pi_{ij} \quad (3-3)$$

The first term in Eq.(3-2) represents the time rate of change of momentum per unit volume in the control volume. The second term is a vector representing the momentum convection, per unit volume, through the control surface. The first term on the right-hand side is the body force per unit volume and Π_{ij} is the stress tensor given in compact tensor notation by

$$\Pi_{ij} = -p\delta_{ij} + \mu \left(\frac{\partial u_i}{\partial x_j} + \frac{\partial u_j}{\partial x_i} \right) + \delta_{ij} \lambda \frac{\partial u_k}{\partial x_k} \quad (i, j, k = 1, 2, 3) \quad (3-4)$$

where δ_{ij} is the Kronecker delta symbol ($\delta_{ij} = 1$ if $i = j$ and $\delta_{ij} = 0$ if $i \neq j$); u_1, u_2, u_3 represent the three components of the velocity vector \mathbf{v} ; μ is the coefficient of viscosity (dynamic viscosity) and λ is the second coefficient of viscosity.

By substituting Eq.(3-4) into Eq.(3-3) and writing the Cartesian component velocities in the directions x, y, z as u, v and w , for clarity, the Navier-Stokes equation is obtained. In component form the Navier-Stokes equations are:

$$\frac{\partial u}{\partial t} \cdot \rho f_x - \frac{\partial p}{\partial x} \cdot \frac{\partial}{\partial x} \left[\frac{2}{3} \mu \left(2 \frac{\partial u}{\partial x} - \frac{\partial v}{\partial y} - \frac{\partial w}{\partial z} \right) \right] \cdot \frac{\partial}{\partial y} \left[\mu \left(\frac{\partial u}{\partial y} - \frac{\partial v}{\partial x} \right) \right] \cdot \frac{\partial}{\partial z} \left[\mu \left(\frac{\partial w}{\partial x} - \frac{\partial u}{\partial z} \right) \right] \quad (3-5)$$

$$\frac{\partial v}{\partial t} \cdot \rho f_y - \frac{\partial p}{\partial y} \cdot \frac{\partial}{\partial x} \left[\mu \left(\frac{\partial v}{\partial x} - \frac{\partial u}{\partial y} \right) \right] \cdot \frac{\partial}{\partial y} \left[\frac{2}{3} \mu \left(2 \frac{\partial v}{\partial y} - \frac{\partial u}{\partial x} - \frac{\partial w}{\partial z} \right) \right] \cdot \frac{\partial}{\partial z} \left[\mu \left(\frac{\partial v}{\partial z} - \frac{\partial w}{\partial y} \right) \right] \quad (3-6)$$

$$\frac{\partial w}{\partial t} \cdot \rho f_z - \frac{\partial p}{\partial z} \cdot \frac{\partial}{\partial x} \left[\mu \left(\frac{\partial w}{\partial x} - \frac{\partial u}{\partial z} \right) \right] \cdot \frac{\partial}{\partial y} \left[\mu \left(\frac{\partial v}{\partial z} - \frac{\partial w}{\partial y} \right) \right] \cdot \frac{\partial}{\partial z} \left[\frac{2}{3} \mu \left(2 \frac{\partial w}{\partial z} - \frac{\partial u}{\partial x} - \frac{\partial v}{\partial y} \right) \right] \quad (3-7)$$

C. ENERGY EQUATION

The energy equation is obtained by applying the First Law of Thermodynamics to a fluid passing through an infinitesimal, fixed control volume

$$\frac{\partial e_t}{\partial t} \cdot \nabla \cdot e_t \cdot \mathbf{v} \cdot \frac{\partial Q}{\partial t} - \nabla \cdot \mathbf{q} \cdot \rho \mathbf{f} \cdot \mathbf{v} \cdot \nabla \cdot (\Pi \cdot \mathbf{v}) \quad (3-8)$$

where e_t is the total energy per unit volume. The first term in left hand-side of Eq.(3-8) represents the rate increase of total energy per unit volume in the control volume while the second term represents the rate of total energy flux per unit volume through the control surface. The first term on the right hand-side is the rate of heat produced by external agents where Q is the heat added to the system. $\nabla \cdot \mathbf{q}$ is the rate of heat conduction through the surface. Fourier's law for heat transfer by conduction states that the heat

transfer q can be expressed as

$$q = -k \nabla T \quad (3-9)$$

where k is the coefficient of thermal conductivity and T is the temperature. \mathbf{f} represents the body forces per unit mass. $\rho \mathbf{f} \cdot \mathbf{v}$ is the work done on the control volume by body surfaces, and $\nabla \cdot (\Pi_{ij} \cdot \mathbf{v})$ is the work done on the control volume by surface forces.

The conservation of energy for a three-dimensional Cartesian coordinate system becomes

$$\begin{aligned} \frac{\partial e_t}{\partial t} - \frac{\partial q}{\partial t} - \rho (f_x u + f_y v + f_z w) + \frac{\partial}{\partial x} (e_t u + p u - u \tau_{xx} - v \tau_{xy} - w \tau_{xz} q \\ + \frac{\partial}{\partial y} (e_t v + p v - u \tau_{xy} - v \tau_{yy} + w \tau_{yz} + q_y) \\ + \frac{\partial}{\partial z} (e_t w + p w - u \tau_{xz} - v \tau_{yz} - w \tau_{zz} + q_z) = 0 \end{aligned} \quad (3-10)$$

where

$$\begin{aligned} \tau_{xx} &= \frac{2}{3} \mu \left(2 \frac{\partial u}{\partial x} - \frac{\partial v}{\partial y} - \frac{\partial w}{\partial z} \right) \\ \tau_{yy} &= \frac{2}{3} \mu \left(2 \frac{\partial v}{\partial y} - \frac{\partial u}{\partial x} - \frac{\partial w}{\partial z} \right) \\ \tau_{zz} &= \frac{2}{3} \mu \left(2 \frac{\partial w}{\partial z} - \frac{\partial v}{\partial y} - \frac{\partial u}{\partial x} \right) \\ \tau_{xz} &= \tau_{zx} = \mu \left(2 \frac{\partial w}{\partial x} + \frac{\partial u}{\partial z} \right) \\ \tau_{xy} &= \tau_{yz} = \mu \left(2 \frac{\partial u}{\partial y} + \frac{\partial v}{\partial x} \right) \\ \tau_{yz} &= \tau_{zy} = \mu \left(2 \frac{\partial v}{\partial z} + \frac{\partial w}{\partial y} \right) \end{aligned} \quad (3-11)$$

D. EQUATIONS IN NONDIMENSIONAL VECTOR FORM

In order to facilitate the numerical implementation the governing fluid dynamic equations are written for a body fitted coordinate system. The equations are transformed to a generalized body fitted coordinate system using the following transformations

$$\xi = \xi(x, y, z), \quad \eta = \eta(x, y, z), \quad \zeta = \zeta(x, y, z) \quad (3-12)$$

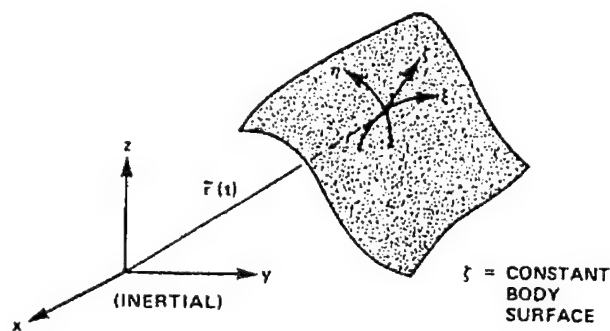
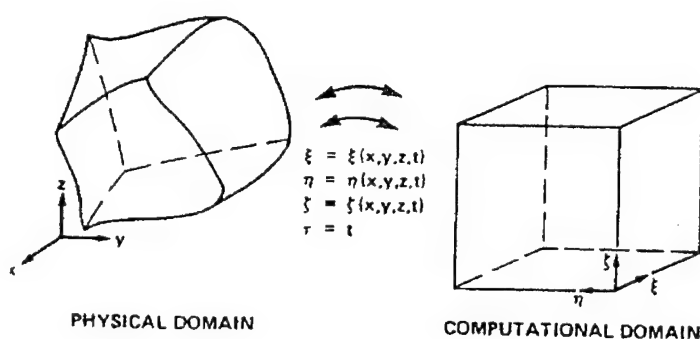


Figure 3-1. Transformations and body coordinate system[15].

The strong conservation law is retained for a curvilinear coordinate system ξ, η, ζ and the governing equations become[15]

$$\partial_t \hat{q} + \partial_{\xi} (\hat{E} + \hat{E}_v) + \partial_{\eta} (\hat{F} + \hat{F}_v) + \partial_{\zeta} (\hat{G} + \hat{G}_v) = 0 \quad (3-13)$$

where

$$\hat{q} \cdot J^{-1} \begin{bmatrix} \rho \\ \rho u \\ \rho v \\ \rho w \\ e_t \end{bmatrix}, \quad \hat{E} \cdot J^{-1} \begin{bmatrix} \rho U \\ \rho u U + \xi_x p \\ \rho v U + \xi_y p \\ \rho w U + \xi_z p \\ (e_t \cdot p) U + \xi_t p \end{bmatrix}, \quad \hat{F} \cdot J^{-1} \begin{bmatrix} \rho V \\ \rho u V + \eta_x p \\ \rho v V + \eta_y p \\ \rho w V + \eta_z p \\ (e_t \cdot p) V + \eta_t p \end{bmatrix}, \quad \hat{G} \cdot J^{-1} \begin{bmatrix} \rho W \\ \rho u W + \zeta_x p \\ \rho v W + \zeta_y p \\ \rho w W + \zeta_z p \\ (e_t \cdot p) W + \zeta_t p \end{bmatrix} \quad (3-14)$$

and

$$\begin{aligned} U &= \xi_t \cdot \xi_x u + \xi_y v + \xi_z w \\ V &= \eta_t \cdot \eta_x u + \eta_y v + \eta_z w \\ W &= \zeta_t \cdot \zeta_x u + \zeta_y v + \zeta_z w \end{aligned} \quad (3-15)$$

where U , V , and W are contravariant velocities written without metric normalization.

The viscous terms are given by

$$\hat{E}_v \cdot J^{-1} \begin{bmatrix} 0 \\ \xi_x \tau_{xx} + \xi_y \tau_{xy} + \xi_z \tau_{xz} \\ \xi_x \tau_{yx} + \xi_y \tau_{yy} + \xi_z \tau_{yz} \\ \xi_x \tau_{zx} + \xi_y \tau_{zy} + \xi_z \tau_{zz} \\ \xi_x \beta_x + \xi_y \beta_y + \xi_z \beta_z \end{bmatrix}, \quad \hat{F}_v \cdot J^{-1} \begin{bmatrix} 0 \\ \eta_x \tau_{xx} + \eta_y \tau_{xy} + \eta_z \tau_{xz} \\ \eta_x \tau_{yx} + \eta_y \tau_{yy} + \eta_z \tau_{yz} \\ \eta_x \tau_{zx} + \eta_y \tau_{zy} + \eta_z \tau_{zz} \\ \eta_x \beta_x + \eta_y \beta_y + \eta_z \beta_z \end{bmatrix}, \quad \hat{G}_v \cdot J^{-1} \begin{bmatrix} 0 \\ \zeta_x \tau_{xx} + \zeta_y \tau_{xy} + \zeta_z \tau_{xz} \\ \zeta_x \tau_{yx} + \zeta_y \tau_{yy} + \zeta_z \tau_{yz} \\ \zeta_x \tau_{zx} + \zeta_y \tau_{zy} + \zeta_z \tau_{zz} \\ \zeta_x \beta_x + \zeta_y \beta_y + \zeta_z \beta_z \end{bmatrix} \quad (3-16)$$

and

$$\begin{aligned}
\tau_{xx} &= \lambda (u_x \cdot v_y \cdot w_z) \cdot 2\mu u_x \\
\tau_{xy} &= \tau_{yx} = \mu (u_y \cdot v_x) \\
\tau_{xz} &= \tau_{zx} = \mu (u_z \cdot w_x) \\
\tau_{yy} &= \lambda (u_x \cdot v_y \cdot w_z) \cdot 2\mu v_y \\
\tau_{yz} &= \tau_{zy} = \mu (v_z \cdot w_y) \\
\tau_{zz} &= \lambda (u_x \cdot v_y \cdot w_z) \cdot 2\mu w_z \\
\beta_x &= \gamma K Pr^{-1} \partial_x e_I + u \tau_{xx} + v \tau_{xy} + w \tau_{xz} \\
\beta_y &= \gamma K Pr^{-1} \partial_y e_I + u \tau_{yx} + v \tau_{yy} + w \tau_{yz} \\
\beta_z &= \gamma K Pr^{-1} \partial_z e_I + u \tau_{zx} + v \tau_{zy} + w \tau_{zz} \\
e_I &= e_t \rho^{-1} - \frac{1}{2} (u^2 + v^2 + w^2)
\end{aligned} \tag{3-17}$$

Here Cartesian derivatives are expanded in terms of ξ , η , ζ coordinates by the chain rule relations as

$$u_x = \xi_x u_\xi + \eta_x u_\eta + \zeta_x u_\zeta \tag{3-18}$$

The Cartesian velocity components u , v , w are non-dimensionalized with respect to a_∞ (the free-stream speed of sound), density, ρ , is referenced to ρ_∞ and total energy, e , to $\rho_\infty a_\infty^2$. Pressure is given by

$$p = (\gamma - 1) \left[e_t - \frac{1}{2} \rho (u^2 + v^2 + w^2) \right] \tag{3-19}$$

and throughout γ is the ratio of specific heats. Also, κ is the coefficient of thermal conductivity, μ is the dynamic viscosity, while λ from the Stokes' hypothesis is $-(2/3)\mu$.

The metric terms and the Jacobian of the transformation are obtained from chain rule expansion of x_ξ , y_ξ , etc., and solved for ξ_x , ξ_y , etc. These terms are given by.

$$\begin{aligned}
 \xi_x &= J(y_\eta z_\zeta - y_\zeta z_\eta) & \eta_x &= J(z_\xi y_\zeta - y_\xi z_\zeta) \\
 \xi_y &= J(z_\eta x_\zeta - x_\eta z_\zeta) & \eta_y &= J(x_\xi z_\zeta - x_\zeta z_\xi) \\
 \xi_z &= J(x_\eta y_\zeta - y_\eta x_\zeta) & \eta_z &= J(y_\xi x_\zeta - x_\xi y_\zeta) \\
 \zeta_x &= J(y_\xi z_\eta - z_\xi y_\eta) & \xi_t &= -x_t \xi_x - y_t \xi_y - z_t \xi_z \\
 \zeta_y &= J(x_\eta z_\xi - x_\xi z_\eta) & \eta_t &= -x_t \eta_x - y_t \eta_y - z_t \eta_z \\
 \zeta_z &= J(x_\xi y_\eta - y_\xi x_\eta) & \zeta_t &= -x_t \zeta_x - y_t \zeta_y - z_t \zeta_z
 \end{aligned} \tag{3-20}$$

and

$$J^{-1} = x_\xi y_\eta z_\zeta - x_\zeta y_\xi z_\eta - x_\eta y_\zeta z_\xi - x_\xi y_\zeta z_\eta - x_\eta y_\xi z_\zeta - x_\zeta y_\eta z_\xi \tag{3-21}$$

E. THIN LAYER APPROXIMATION

In order to accurately compute the normal gradients in the boundary layer, it is necessary to make the normal grid spacing very fine close to the body surface. In the streamwise direction the flow gradients are not large, when compared to those in the normal direction, and the resolution of the grid can be lower. This results in a mesh where the cells have a high aspect ratio close to the body and a smaller aspect ratio when approaching the outer boundary of the computational domain. This procedure is going to save considerable computer storage and computation time without sacrificing the accuracy of the computation.

In a thin-layer approximation all viscous derivatives in the ξ and η direction (along the body) are neglected, while terms in normal direction ζ are retained, (see Fig.3-1). Eq.(3-1) thus simplifies to

$$\partial_{\tau} \hat{G} + \partial_{\xi} \hat{E} + \partial_{\eta} \hat{F} + \partial \hat{G} = Re^{-1} \partial_{\zeta} \hat{S} \quad (3-22)$$

where

$$\hat{S} \cdot J^{-1} \begin{bmatrix} 0 \\ \mu (\zeta_x^2 \zeta_y^2 \zeta_z^2) u_{\zeta} (\mu/3) (\zeta_x u_{\zeta} \zeta_y v_{\zeta} \zeta_z w_{\zeta}) \zeta_x \\ \mu (\zeta_x^2 \zeta_y^2 \zeta_z^2) v_{\zeta} (\mu/3) (\zeta_x u_{\zeta} \zeta_y v_{\zeta} \zeta_z w_{\zeta}) \zeta_y \\ \mu (\zeta_x^2 \zeta_y^2 \zeta_z^2) w_{\zeta} (\mu/3) (\zeta_x u_{\zeta} \zeta_y v_{\zeta} \zeta_z w_{\zeta}) \zeta_z \\ (\zeta_x^2 \zeta_y^2 \zeta_z^2) [0.5 \mu (u^2 \cdot v^2 \cdot w^2)_{\zeta} KPr^{-1} (\gamma \cdot 1)^{-1} (a^2)_{\zeta}] \\ (\mu/3) ((\mu/3) (\zeta_x u_{\zeta} \zeta_y v_{\zeta} \zeta_z w_{\zeta}) (\zeta_x u_{\zeta} \zeta_y v_{\zeta} \zeta_z w_{\zeta})) \end{bmatrix} \quad (3-23)$$

Unlike the boundary-layer model the thin layer accounts for pressure variations in the normal direction and does not require matching an inviscid layer with a viscous layer.

The eddy viscosities were computed using the algebraic Baldwin-Lomax eddy viscosity model.

IV. FLOW FIELD COMPUTATION

The flow field was computed in order to obtain the temperature variation on the surface of the dome, corresponding to the IR window. The aerodynamic heating of the infrared window is responsible for a degradation of the seeker infrared sensor performance at supersonic speeds.

A. METHODOLOGY

For the space discretization the Steger-Warming flux vector splitting is used along the streamwise direction. Along the circumferential and normal directions central differences with added numerical dissipation are used. The integration is performed with a two-factor partially flux split implicit algorithm. A combination of second and fourth order differences have been used for smoothing along the central-differencing directions. Fourth-order dissipation terms are added explicitly to the equations to damp high frequency growth and thus serve to control nonlinear instability. The resulting implicit code is second-order accurate in space.

A body-fitted grid, clustered in the radial direction was employed to resolve the viscous layer adjacent to the body surface. This grid was obtained by means of a hyperbolic grid generator.

The flow field was computed using the OVERFLOW Version 1.6t code developed at NASA Ames Research Center running in a STARDENT workstation installed at the Computational Fluid Dynamics Laboratory (Naval Postgraduate School). After a solution was obtained, the original grid points were redistributed (adapted) based on the

initial flowfield solution, and a new solution was computed using the adapted grid. This procedure increases the accuracy of the flow prediction by decreasing the effects of flowfield discretization. This procedure is particularly important, in supersonic flow computations, where the existence of strong gradients and shocks require careful distribution of grid points to minimize errors and produce more accurate flow field predictions.

B. BODY GEOMETRY AND GRID GENERATION

The flowfield was computed around three distinct body geometries, namely two nose shapes (cases I & II) and a test geometry(case III). The case III geometry had the shape of a hemisphere-cylinder. The computed shock stand-off distances and surface pressure distribution of this latter configuration was compared with experimental data to give confidence in the computations.

Several C-O type grids were generated, corresponding to the hemispherical-ogive (case I) and to the ellipsoidal-ogive (case II) forebody. Longitudinal cross sections of the computational grids for the case I and case II are shown in Fig. 4-3 and Fig. 4-4 respectively. The case I body consists of a truncated hemisphere forebody(1.9024 cm long) attached to a 3:1 tangent ogive (12.728 cm long) attached to a 4 caliber tangent cylindrical afterbody. The case II body consists of a truncated ellipsoidal forebody(2.6943 cm long) attached to a 3:1 tangent ogive (12.728 cm long) attached to a 4 caliber tangent cylindrical afterbody. The hemispherical and ellipsoidal portions of the nose correspond to the

IR window locations respectively. The origin of the physical coordinates is at the nose tip for both cases. The three-dimensional body fitted grids were generated using the HYPGEN code. After a flow solution was found an adaptative grid code[17], SAGE, based on the algebraic, solution-adaptive scheme of Nakahashi and Deiwert, was used, in order to enhance the resolution for better capture of the shock front. A third inviscid grid was designed to compute the flow around a hemisphere-cylinder(case III).- corresponding to the test case. The geometrical shapes of the bodies considered are as follows,

1. Case I. Hemisphere-Ogive-Cylinder (Fig. 4-1)

This nose configuration corresponding to the hemispherical dome is defined using the following relation

$$\begin{aligned} r &= \sqrt{3.3166^2 - (z - 3.3166)^2}, & 0 \leq z \leq 1.9024 \\ r &= \frac{2}{3}(z - 3.3697) - \frac{(z - 3.3697)^2}{54}, & 1.9024 \leq z \leq 14.6303 \\ r &= 6.0000, & z \geq 14.6303 \end{aligned} \quad (4-1)$$

The origin of the coordinate system is located at the tip of the nose. Fig. 4-3 shows the computational grid used for the calculations. The resolution of the grid is increased around the shock wave where the flow gradients are large.

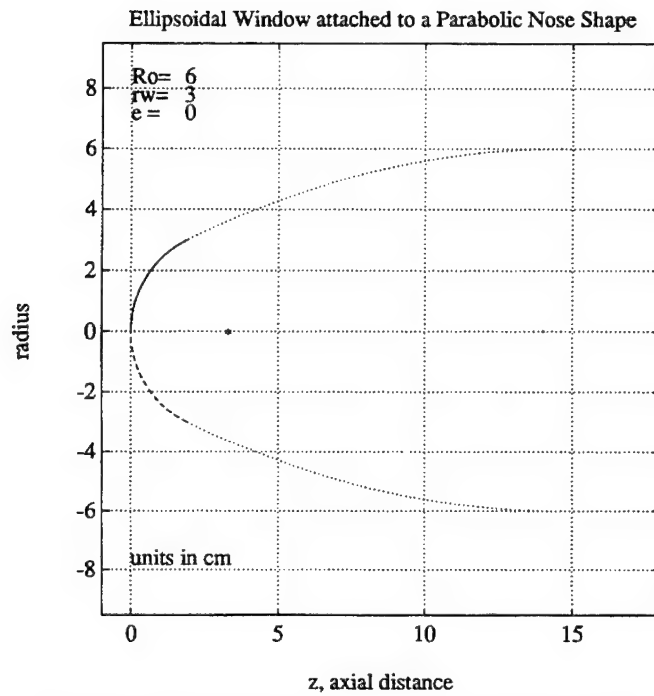


Figure 4-1. Hemisphere-Ogive nose configuration.

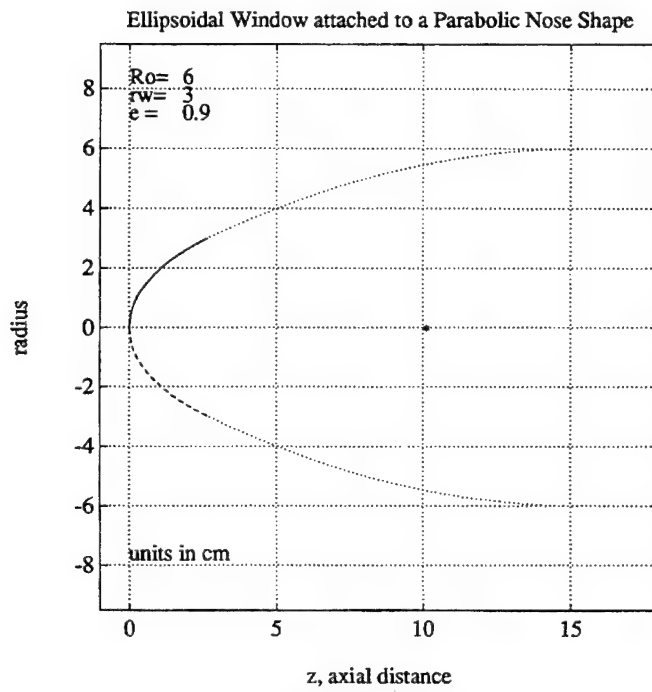


Figure 4-2. Ellipsoid-Ogive nose configuration.

2. Case II. Ellipsoid-Ogive-Cylinder

This nose configuration corresponding to the ellipsoidal dome is defined using the following relations:

$$\text{ellipsoid excentricity} = 0.9$$

$$\begin{aligned} r &= 4.489 \sqrt{1 - \frac{(z-10.1376)^2}{(10.1376)^2}}, & 0 \leq z \leq 2.6943 \\ r &= \frac{2}{3}(z-2.577) - \frac{(z-2.577)^2}{54}, & 2.6943 \leq z \leq 15.4223 \\ r &= 6.0000, & z \geq 15.4223 \end{aligned} \quad (4-2)$$

Figure 4-4 shows the 77x93x31 computational grid used for the calculations.

3. Case III. Hemisphere-Cylinder (Fig. 4-2)

This body configuration corresponds to the test case. Its shape is defined by the following relations:

$$\begin{aligned} r &= \sqrt{36.00^2 - (z-6.00)^2} & 0 \leq z \leq 6.00 \\ r &= 6.00, & z \geq 6.00 \end{aligned} \quad (4-3)$$

C. GRID ADAPTATION

Grid adaptation procedures in general either redistribute points or refine distribution (by adding points) to reduce solution errors by minimizing grid discretization errors. Gnoffo[17] first introduced a method for the redistribution of grid points based on local flow gradients. This method is analogous to finding the equilibrium position of a system of springs that connect each node with adjacent nodes and whose spring forces (or tension constant)

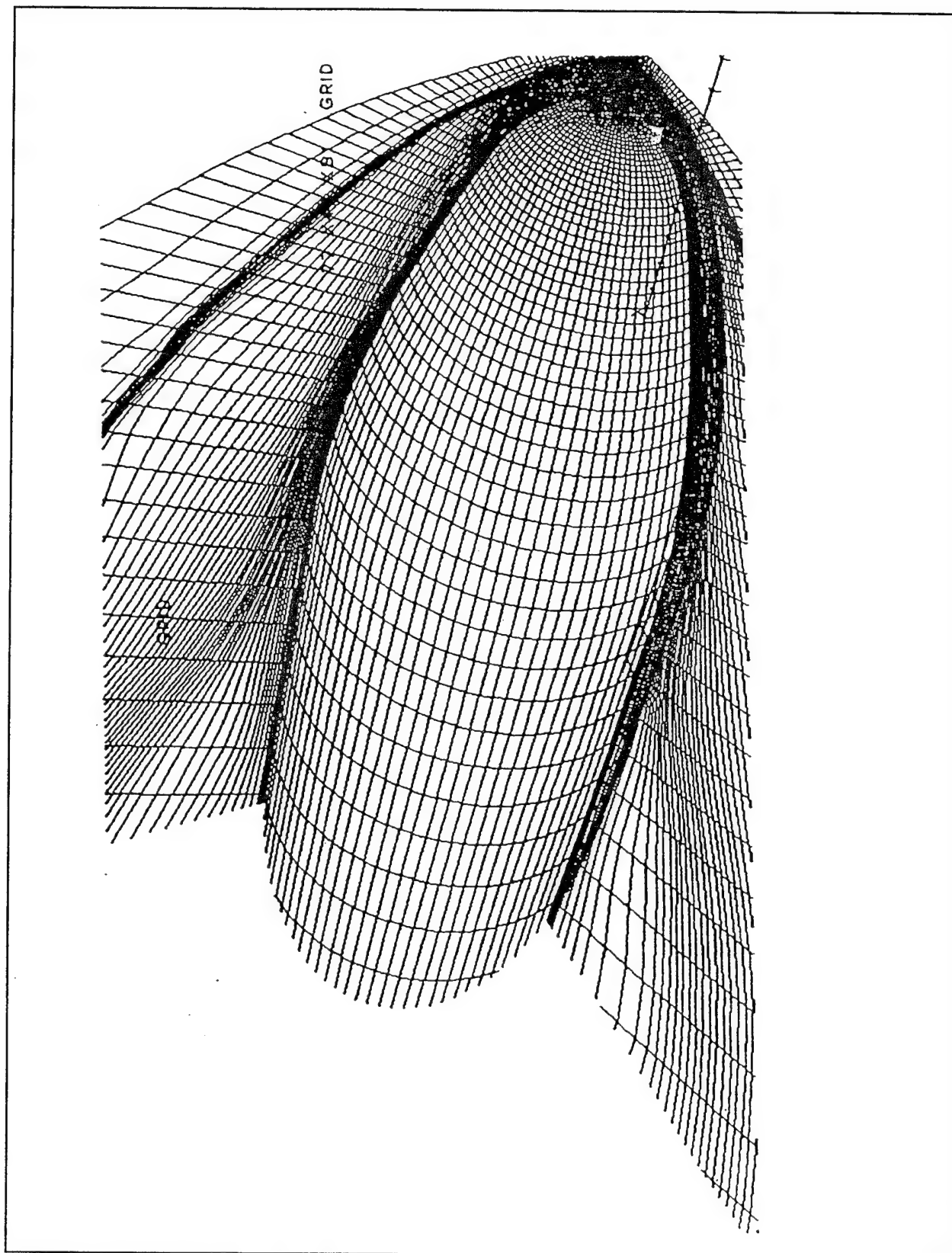


Figure 4-3. 77x48x81 viscous computational adapted grid for the Hemisphere-Ogive-Cylinder.

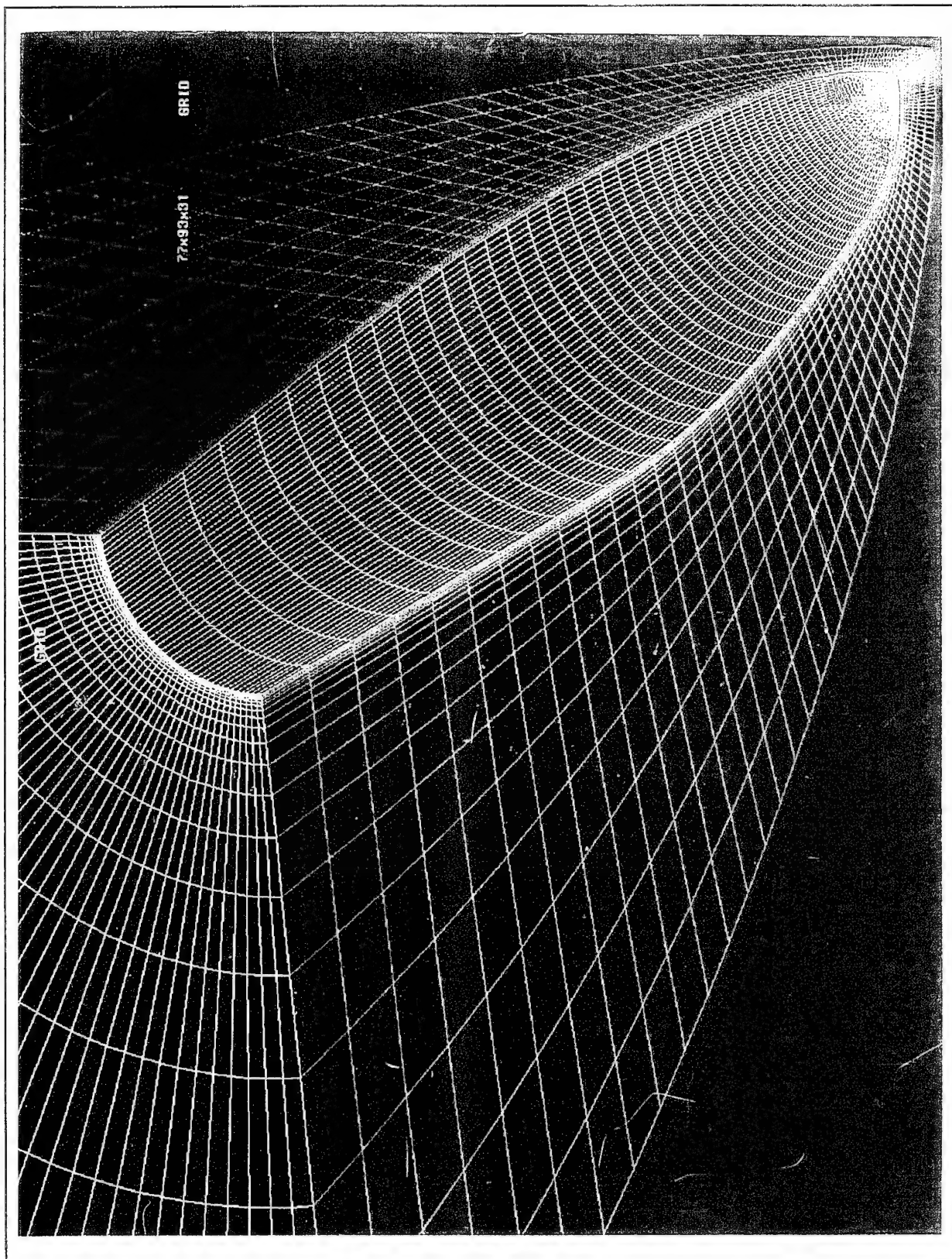


Figure 4-4. Three dimensional Hemisphere-Ogive-Cylinder computational mesh.

is proportional to the local error or weight function. The multidimensional problem of grid adaptation is split into a series of one-dimensional (1-D) problems along the computation coordinate lines. The reduced 1-D problem then requires a tridiagonal solver to find the location of grid points along a given coordinate line. Multidirectional adaptation is achieved by the sequential application of the method in each coordinate direction (Fig. 4-5).

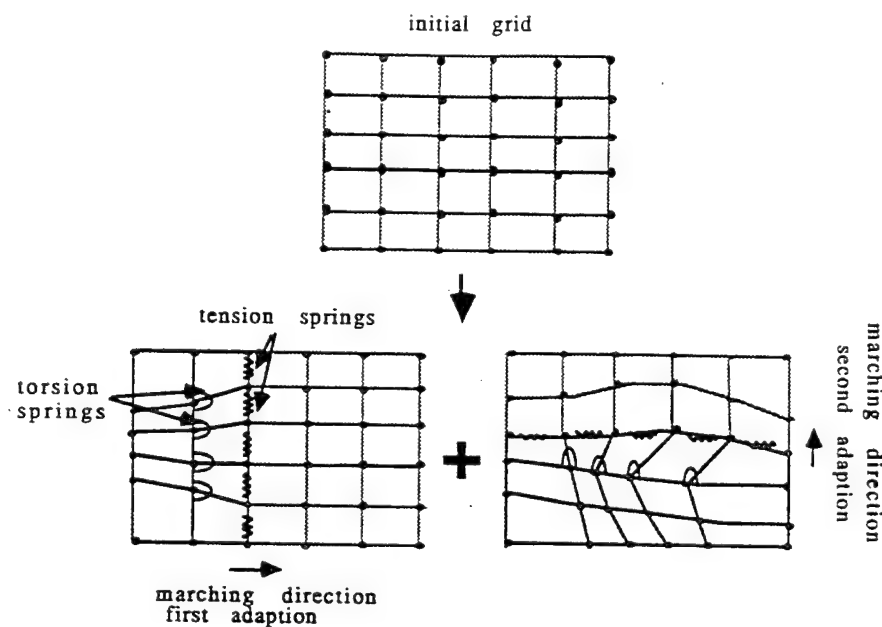


Figure 4-5. Splitting of 2-D adaptation into two 1-directional adaptations[17].

In the adaptive grid procedure outlined by Nakahashi and Deiwert (1985) the tension force directs the redistribution of points to the strong gradient regions. To maintain smoothness and a measure of orthogonality of grid lines, torsional forces are introduced that relate information between the family of lines adjacent to one another[16]. The smoothness and orthogonality constraints are direction-dependent, since they relate only the coordinate lines that are being adapted to the neighboring lines that have already

been adapted. This implies that the solutions are nonunique and depend on the order and direction of adaptation. Nonuniqueness of the adapted grid is acceptable since it makes possible an overall and local error reduction through grid redistribution.

D. RESULTS AND DISCUSSION

Table 4-1 shows the computed values of absolute temperature, normalized temperature and coefficient of pressure along the stagnation streamline obtained by the solution of the thin-layer Navier-Stokes equations about the hemisphere-ogive-cylinder nose (Case I) at zero incidence at Mach 4. A 77x7x35 grid point inviscid grid was used. The solution was considered converged after 1500 steps. Figs.4-6 and Fig.4-7 show the plot of these flow quantities versus distance from the stagnation point. The bow shock stand-off distance taken from the computed flow field is approximately 0.36cm, corresponding to a $\Delta/R=.11$. From the plot of Fig. 4-7 we can see that the temperature jump across the shock is 4.15 compared with the value of 4.04 obtained from normal shock tables.

Table 4-2 shows the computed values of absolute temperature, normalized temperature and coefficient of pressure on the surface of the nose along a streamline for the hemisphere-ogive at Mach 4 for the same conditions of Table 4-1. Fig. 4-8 shows the computed temperature profile of the dome surface temperature. The computed normalized stagnation temperature is 4.6 comparing with 4.2 obtained using Eq.(2-7). Fig. 4-9 shows the computed dome pressure distribution. Fig. 4-10 shows the OVERFLOW input file used to

generate the values of Tables 4-1 and 4-2. Fig. 4-11 shows the three-dimensional flow-field around the missile afterbody. The IR dome corresponds to the white portion of the nose tip. Fig. 4-12 shows the density field in front of the IR dome.

The flow field has cylindrical symmetry at zero angle-of-attack. With missile incidence the flow is no longer axisymmetric. Figs. 4-13 and 4-14 show the Mach number distribution and the dome temperature field in the dome for an angle of attack of 5° . Fig. 4-15 gives the density field. It was obtained using the viscous adapted grid of Fig.4-5.

In the computation of the flow it was assumed that the dome had reached thermal equilibrium and the wall was adiabatic. In order to obtain the equilibrium temperature the dome should be divided into elements and a procedure like the one outlined in Eq.(2-24) should be carried out to consider radiation and conduction losses. The heat transfer coefficient at stagnation is given by Eq.(2-20). For other elements that make an off-axis angle (angle between the longitudinal axis of the missile and the line between the dome element and the dome center of curvature), θ , the value of h_{st} should be multiplied by $\cos(\theta)^{3/2}$. In this study the dome material was assumed to be sapphire or CVD(Chemical Vapour Deposition) Diamond. These materials make it possible to fabricate IR domes with a high thermal shock resistance(see Appendix A) suitable for the MWIR(Medium Wave Infrared) and LWIR(Long Wave Infrared) spectral bands respectively. In Appendix A it is shown that for a diamond window at Mach 4 a dome thickness of 1mm is enough to withstand the flight conditions. Therefore we can expect that conduction losses are not going to be

very high since the area of the attachment is small. Also, since the emissivity of these materials is small we can expect small radiation losses. In this case, considering the wall adiabatic might be a good approximation.

Table 4-1. Computed streamline flow field properties ($Mach=4.0$, $\alpha=0$).

z	x	y	T(K)	T/Tinf	Cp
0.0000000E+00	0.0000000E+00	0.0000000E+00	1251.995	4.333828	1.769331
-1.4072160E-02	0.0000000E+00	0.0000000E+00	1251.995	4.333828	1.769331
-2.8457001E-02	0.0000000E+00	0.0000000E+00	1244.208	4.306874	1.758680
-4.3183811E-02	0.0000000E+00	0.0000000E+00	1237.092	4.282242	1.753231
-5.8293991E-02	0.0000000E+00	0.0000000E+00	1232.358	4.265854	1.735707
-7.3827960E-02	0.0000000E+00	0.0000000E+00	1231.002	4.261161	1.726179
-8.9831688E-02	0.0000000E+00	0.0000000E+00	1228.993	4.254206	1.708787
-0.1063549	0.0000000E+00	0.0000000E+00	1227.959	4.250627	1.697652
-0.1234523	0.0000000E+00	0.0000000E+00	1226.781	4.246548	1.688257
-0.1411849	0.0000000E+00	0.0000000E+00	1226.759	4.246473	1.686138
-0.1596204	0.0000000E+00	0.0000000E+00	1225.986	4.243798	1.679476
-0.1788342	0.0000000E+00	0.0000000E+00	1225.059	4.240590	1.674541
-0.1989112	0.0000000E+00	0.0000000E+00	1221.979	4.229926	1.657630
-0.2199472	0.0000000E+00	0.0000000E+00	1219.554	4.221533	1.653118
-0.2420507	0.0000000E+00	0.0000000E+00	1212.904	4.198514	1.616354
-0.2653450	0.0000000E+00	0.0000000E+00	1207.786	4.180799	1.610427
-0.2899718	0.0000000E+00	0.0000000E+00	1177.408	4.075641	1.431967
-0.3160940	0.0000000E+00	0.0000000E+00	997.7296	3.453679	0.7734069
-0.3439003	0.0000000E+00	0.0000000E+00	696.3934	2.410592	0.3077108
-0.3736109	0.0000000E+00	0.0000000E+00	473.6082	1.639413	0.1148101
-0.4054836	0.0000000E+00	0.0000000E+00	337.6206	1.168687	2.9509827
-0.4398234	0.0000000E+00	0.0000000E+00	291.7347	1.009851	2.8921142
-0.4769938	0.0000000E+00	0.0000000E+00	288.1387	0.9974033	-8.0908835
-0.5174306	0.0000000E+00	0.0000000E+00	289.3298	1.001526	5.1899254
-0.5616624	0.0000000E+00	0.0000000E+00	288.7061	0.9993671	-2.2675097
-0.6103359	0.0000000E+00	0.0000000E+00	288.9403	1.000178	6.7792833
-0.6642512	0.0000000E+00	0.0000000E+00	288.3846	0.9999849	-5.8636069
-0.7244109	0.0000000E+00	0.0000000E+00	288.8838	0.9999823	-5.1110983
-0.7920877	0.0000000E+00	0.0000000E+00	288.3910	1.000007	2.2649765
-0.8689228	0.0000000E+00	0.0000000E+00	288.3875	0.9999951	-6.2584877
-0.9570694	0.0000000E+00	0.0000000E+00	288.3888	0.9999998	1.6391277
-1.059409	0.0000000E+00	0.0000000E+00	288.3887	0.9999993	-1.0430813
-1.179889	0.0000000E+00	0.0000000E+00	288.3891	1.000001	-1.4901161
-1.324077	0.0000000E+00	0.0000000E+00	288.3890	1.000000	-2.2351742
-1.500000	0.0000000E+00	0.0000000E+00	288.3888	0.9999998	-1.4901161

Table 4-2. Computed hemispherical dome temperature profile (Mach=4.0, $\alpha=0$) (adiabatic wall).

z	x	y	T(K)	T/Tratio	Cp
0.0000000E+00	0.0000000E+00	0.0000000E+00	1251.995	4.333828	1.769331
9.9657424E-05	-1.5062407E-02	1.5062407E-02	1267.223	4.386541	1.962640
3.1045929E-04	-3.0966893E-02	3.0966893E-02	1299.271	4.497478	1.752715
6.7767297E-04	-4.7760621E-02	4.7760621E-02	1280.968	4.434122	1.695181
1.2542109E-03	-6.5493003E-02	6.5493003E-02	1249.678	4.325809	1.720564
2.0872049E-03	-8.4215783E-02	8.4215783E-02	1257.582	4.353167	1.724007
3.2189630E-03	-0.1039834	0.1039834	1249.013	4.323505	1.722371
4.6833940E-03	-0.1248538	0.1248538	1246.343	4.314264	1.724451
6.5123211E-03	-0.1468881	0.1468881	1244.572	4.308134	1.734758
8.7461583E-03	-0.1701505	0.1701505	1242.742	4.301799	1.720822
1.1447350E-02	-0.1947079	0.1947079	1241.205	4.296480	1.720025
1.4705360E-02	-0.2206291	0.2206291	1239.578	4.290847	1.714795
1.8604770E-02	-0.2479863	0.2479863	1237.847	4.284853	1.712322
2.3207851E-02	-0.2768574	0.2768574	1236.551	4.280367	1.705234
2.8605610E-02	-0.3073223	0.3073223	1233.810	4.270882	1.693714
3.4932461E-02	-0.3394611	0.3394611	1230.839	4.260595	1.682505
4.2309761E-02	-0.3733589	0.3733589	1225.294	4.241401	1.664191
5.0861739E-02	-0.4091049	0.4091049	1219.603	4.221704	1.645974
6.0756631E-02	-0.4467875	0.4467875	1213.211	4.199575	1.623081
7.2170392E-02	-0.4864984	0.4864984	1207.618	4.180215	1.600384
8.5286379E-02	-0.5283324	0.5283324	1202.201	4.161465	1.575645
0.1003310	-0.5723819	0.5723819	1196.849	4.142937	1.548760
0.1175769	-0.6187352	0.6187352	1190.913	4.122391	1.517524
0.1372850	-0.6674858	0.6674858	1184.456	4.100039	1.482646
0.1597211	-0.7187309	0.7187309	1177.089	4.074539	1.442449
0.1852678	-0.7725453	0.7725453	1168.978	4.046461	1.397681
0.2143953	-0.8289816	0.8289816	1160.507	4.017141	1.350345
0.2474633	-0.8881212	0.8881212	1151.573	3.986216	1.300280
0.2845651	-0.9501302	0.9501302	1141.344	3.950806	1.244585
0.3262986	-1.015036	1.015036	1129.308	3.909142	1.180110
0.3741227	-1.082561	1.082561	1117.331	3.867683	1.113770
0.4285642	-1.152694	1.152694	1107.076	3.832187	1.052923
0.4898345	-1.225565	1.225565	1096.837	3.796744	0.9921541
0.5583310	-1.301251	1.301251	1085.214	3.756512	0.9268997
0.6348174	-1.379679	1.379679	1070.954	3.707150	0.8532277
0.7209599	-1.460286	1.460286	1054.802	3.651238	0.7726322
0.8182739	-1.542456	1.542456	1039.500	3.598270	0.6957317
0.9271546	-1.626161	1.626161	1024.936	3.547855	0.6245722
1.048522	-1.711070	1.711070	1009.356	3.493925	0.5531548
1.184194	-1.796106	1.796106	993.5675	3.439272	0.4834213
1.335237	-1.880588	1.880588	977.4219	3.383384	0.4184332
1.502349	-1.964151	1.964151	958.0651	3.316379	0.3508716

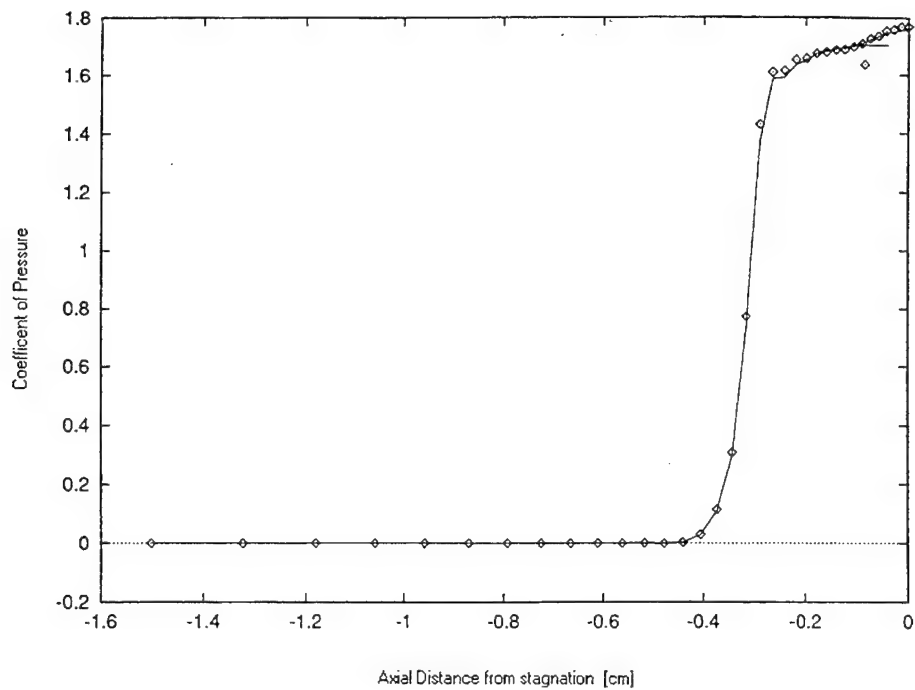


Figure 4-6. Plot of the coefficient of Pressure along the stagnation streamline for the computed flow field around the hemisphere-ogive-cylinder.

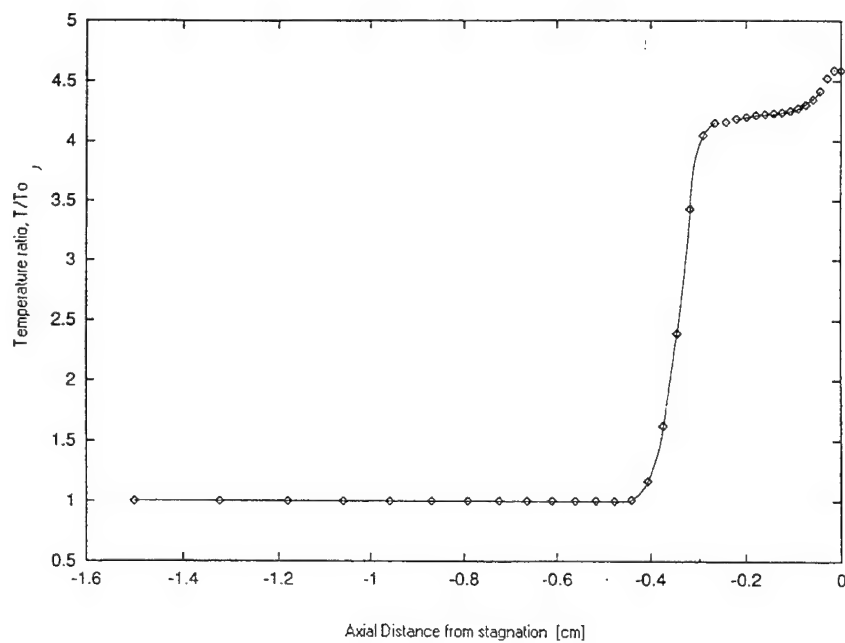


Figure 4-7. Plot of the normalized temperature along the stagnation streamline for the computed flow field for the hemisphere-ogive-cylinder.

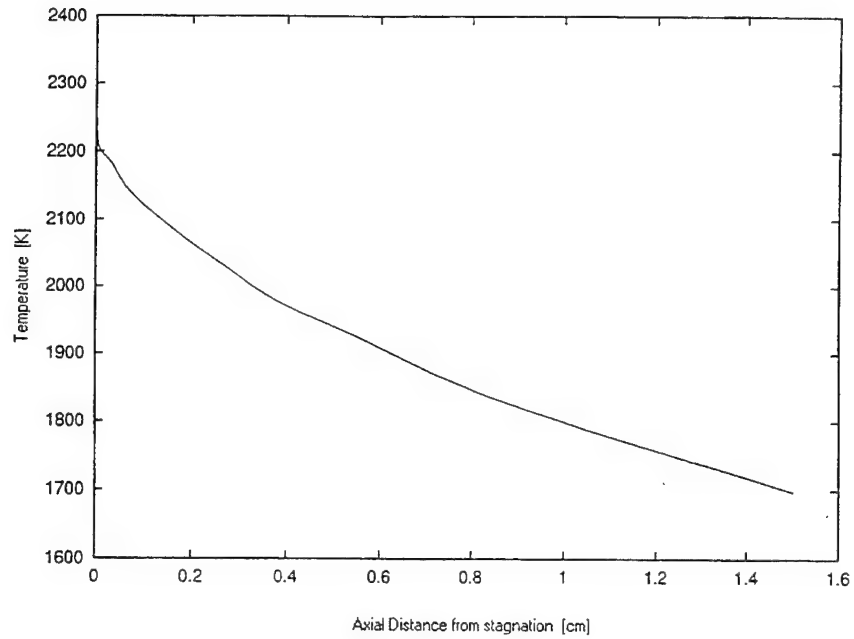


Figure 4-8. Dome temperature plot (adiabatic wall) for hemisphere-ogive-cylinder. Units are measured in centimeters along the missile longitudinal axis.

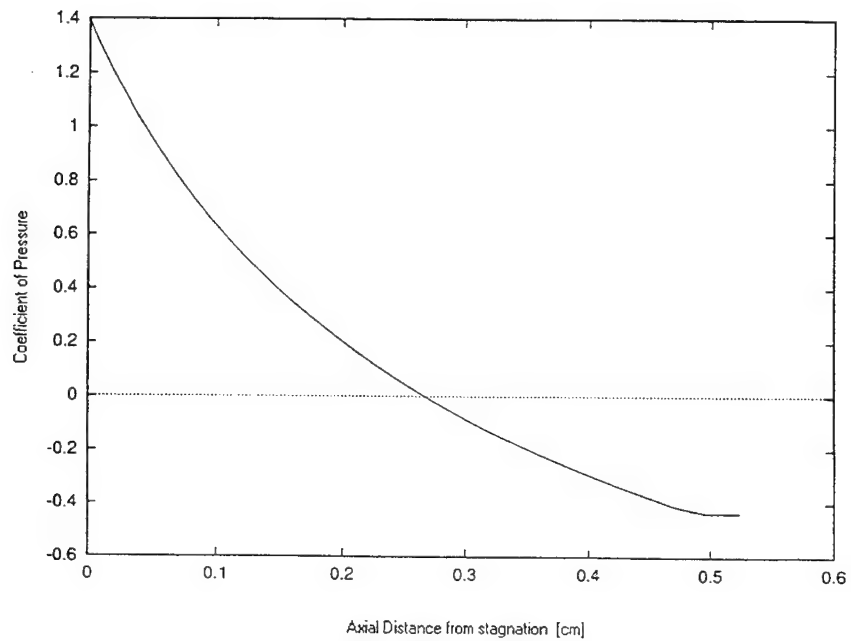


Figure 4-9. Plot of the Coefficient of Pressure over the dome for the computed flow field of Fig. 4-12. Units are measured in centimeters along the missile longitudinal axis.

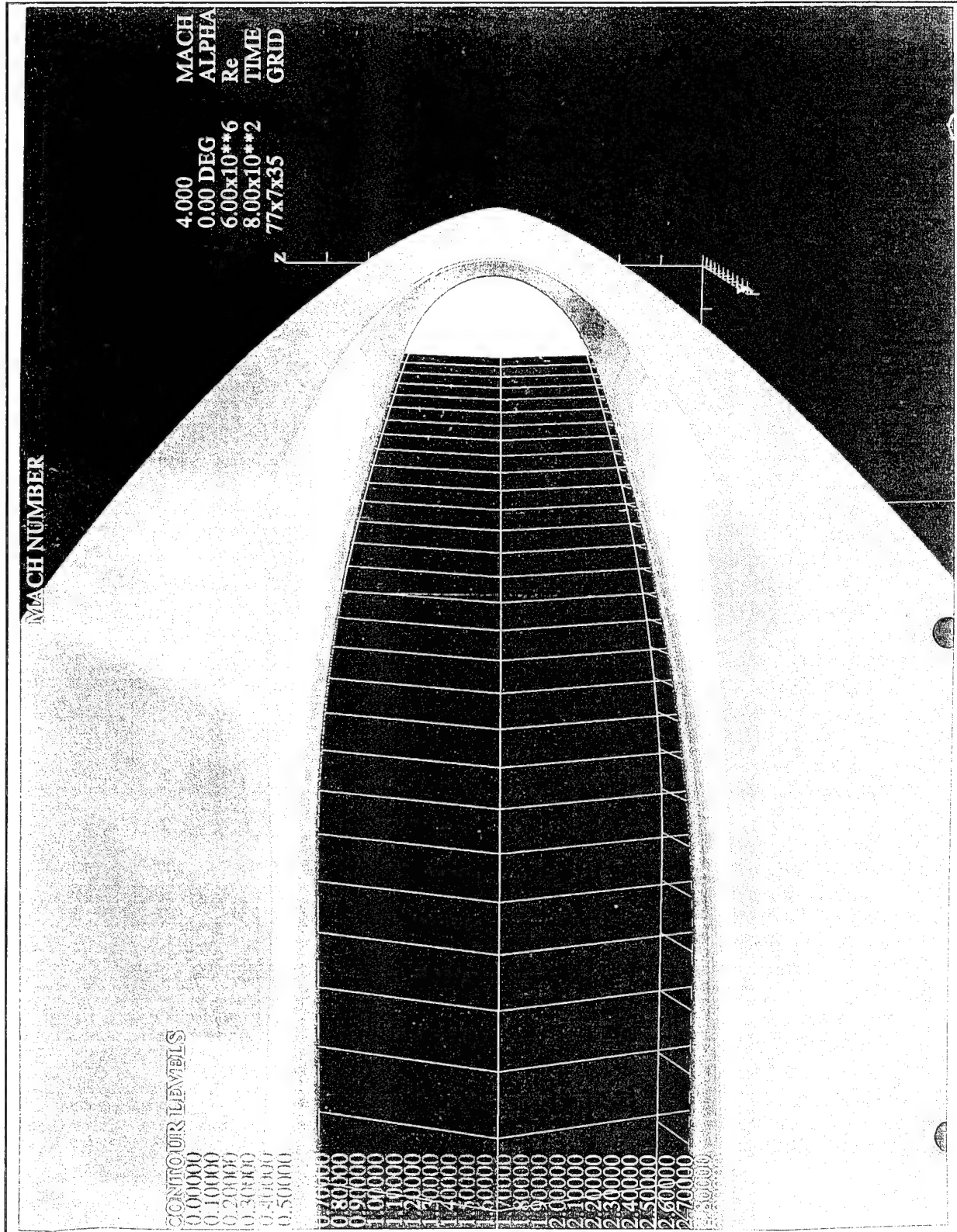
```

$GLOBAL
  CHIMRA= .F.,   NSTEPS= 600,   RESTRT= .T.,   NSAVE = 50,
  NQT   = 0,
$SEND
$FLOINP
  ALPHA = 0.0,   FSMACH= 4.00,   REY   = 6.00E6,   TINF = 520.000,
$SEND
$VARGAM
$SEND
$GRDNAM
  NAME = 'Hemisphi-ogiv- Cylinder 77x7x35 (A=0.0 deg, M=4.00, Re=6.00 mil.)',
$SEND
$NITERS
$SEND
$METPRM
  IRHS = 0,   ILHS = 2,   IDISS = 2,
$SEND
$TIMACU
  DT    = 0.20,   ITIME= 1,   TFOSO = 1.00,
$SEND
$SMOACU
  ISPECJ= 2,   DIS2J = 2.00,   DIS4J = 0.02,
  ISPECK= 2,   DIS2K = 2.00,   DIS4K = 0.02,
  ISPECL= 2,   DIS2L = 2.00,   DIS4L = 0.02,
  SMOO  = 1.00,
  EPSE  = 0.35,
$SEND
$VISINP
  VISCJ = .F.,   VISCK = .F.,   VISCL = .T.,
  NTURB = 1,
  ITTYP = 1,
  ITDIR = 3,
  JTLS  = 1,
  JTLE  = 77,
  KTLS  = 1,
  KTLE  = 7,
  LTLS  = 1,
  LTLE  = 35,
  TLPAR1= 0.3,
$SEND
$BCINP
  NBC   = 6,
  IBTYP = 15,   12,   12,   5,   32,   30,
  IBDIR = 1,    2,   -2,   3,   -3,   -1,
  JBCE  = 1,    1,    1,    1,    1,   77,
  JBCE  = 1,   77,   77,   77,   77,   77,
  KBCE  = 1,    1,    7,    1,    1,    1,
  KBCE  = 7,    1,    7,    7,    7,    7,
  LBCE  = 1,    1,    1,    1,   35,    1,
  LBCE  = 35,   35,   35,    1,   35,   35,
$SEND
$SCEINP
$SEND

```

Figure 4-10. Sample OVERFLOW Input File.

Figure 4-11. Thin-Layer Navier-Stokes Mach Number flow field solution for the Hemisphere-Ogive body
(Mach=4.0, 77x7x35 computational grid).



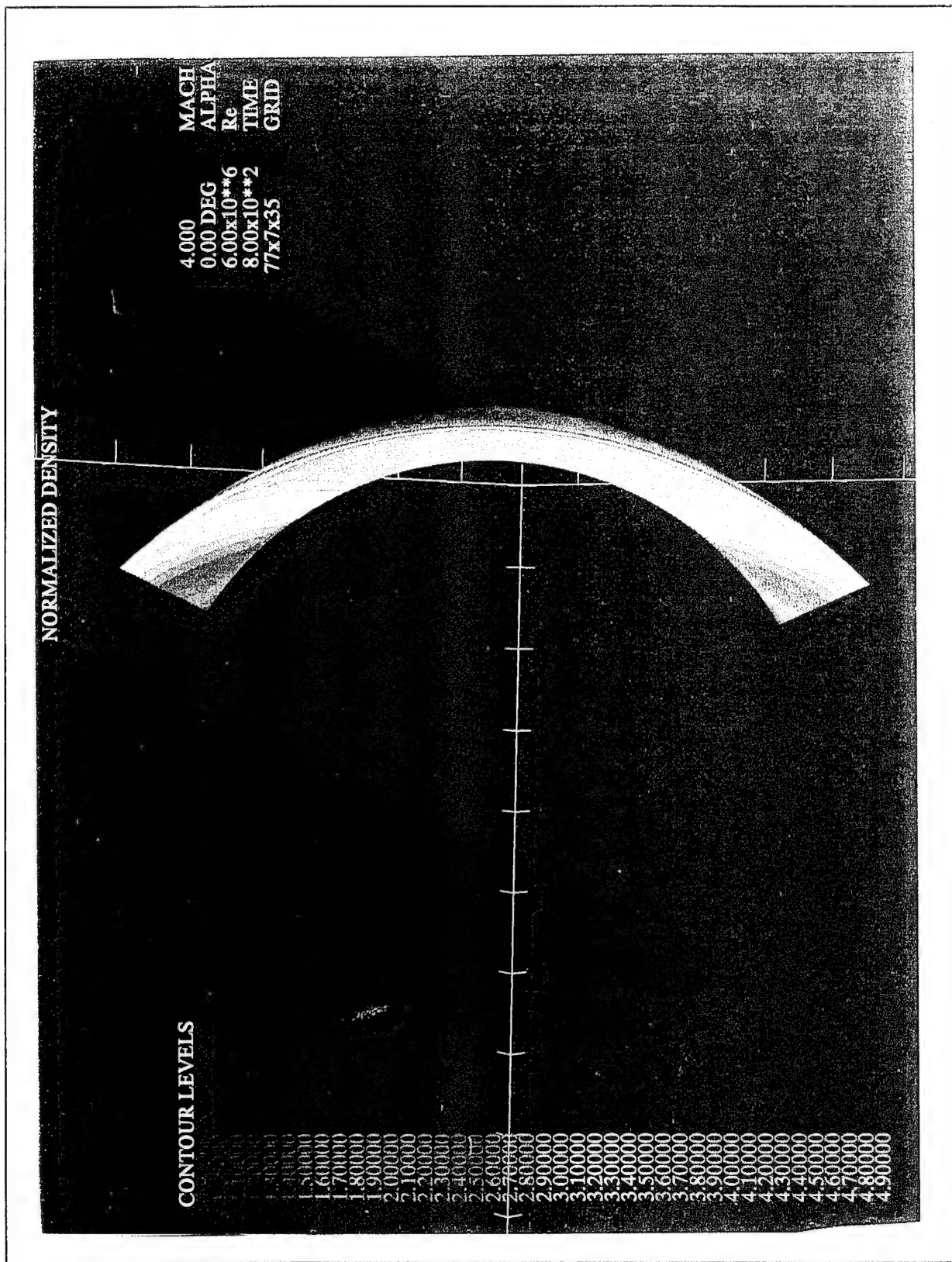
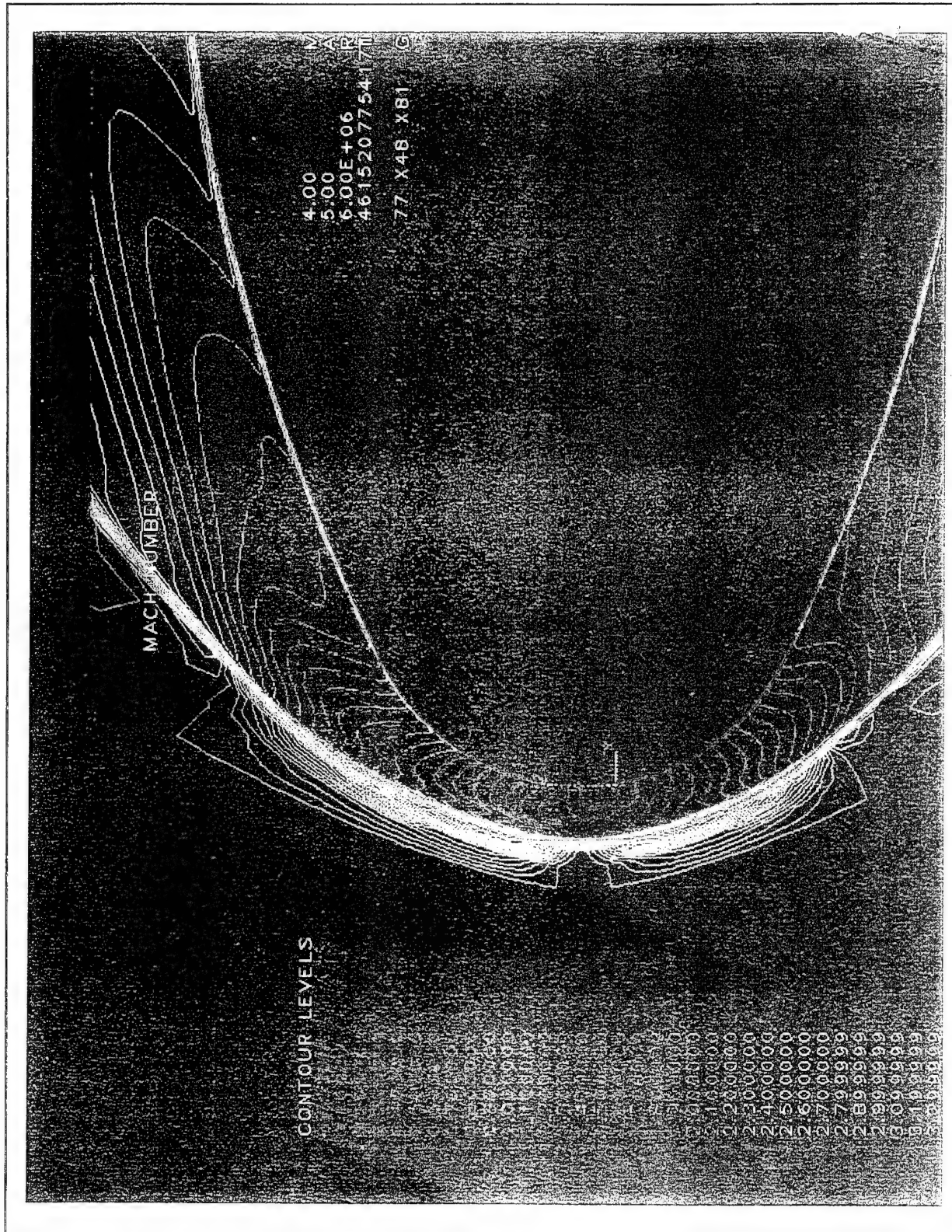


Figure 4-12. Gradient of index "lens" created by the compressed gas in front of the dome at Mach=4.0.

Figure 4-13. Thin-Layer Navier-Stokes Mach Number flow field solution for the Hemisphere-Ogive body at 5° angle-of-attack (Mach=4.0, 77x48x81 adapted grid).



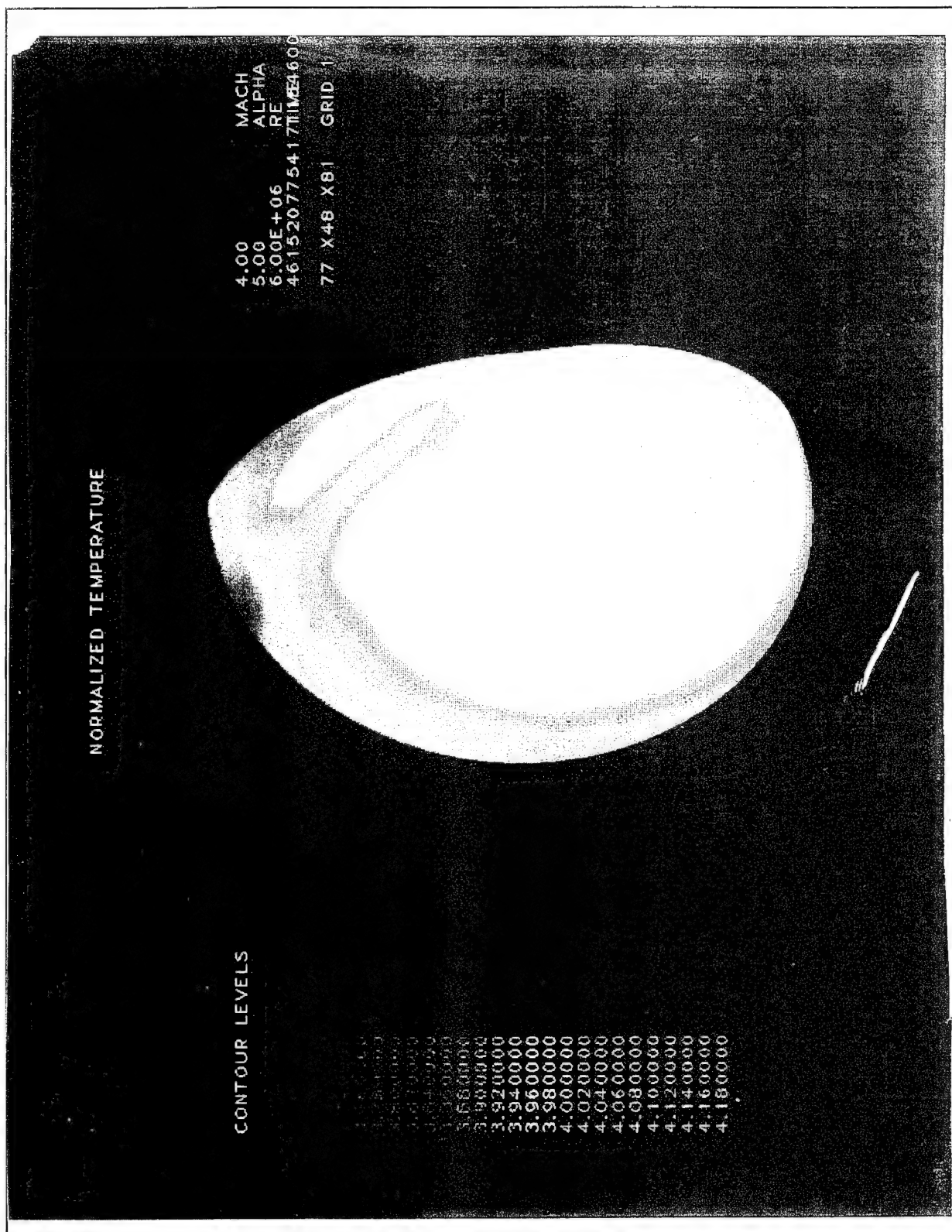
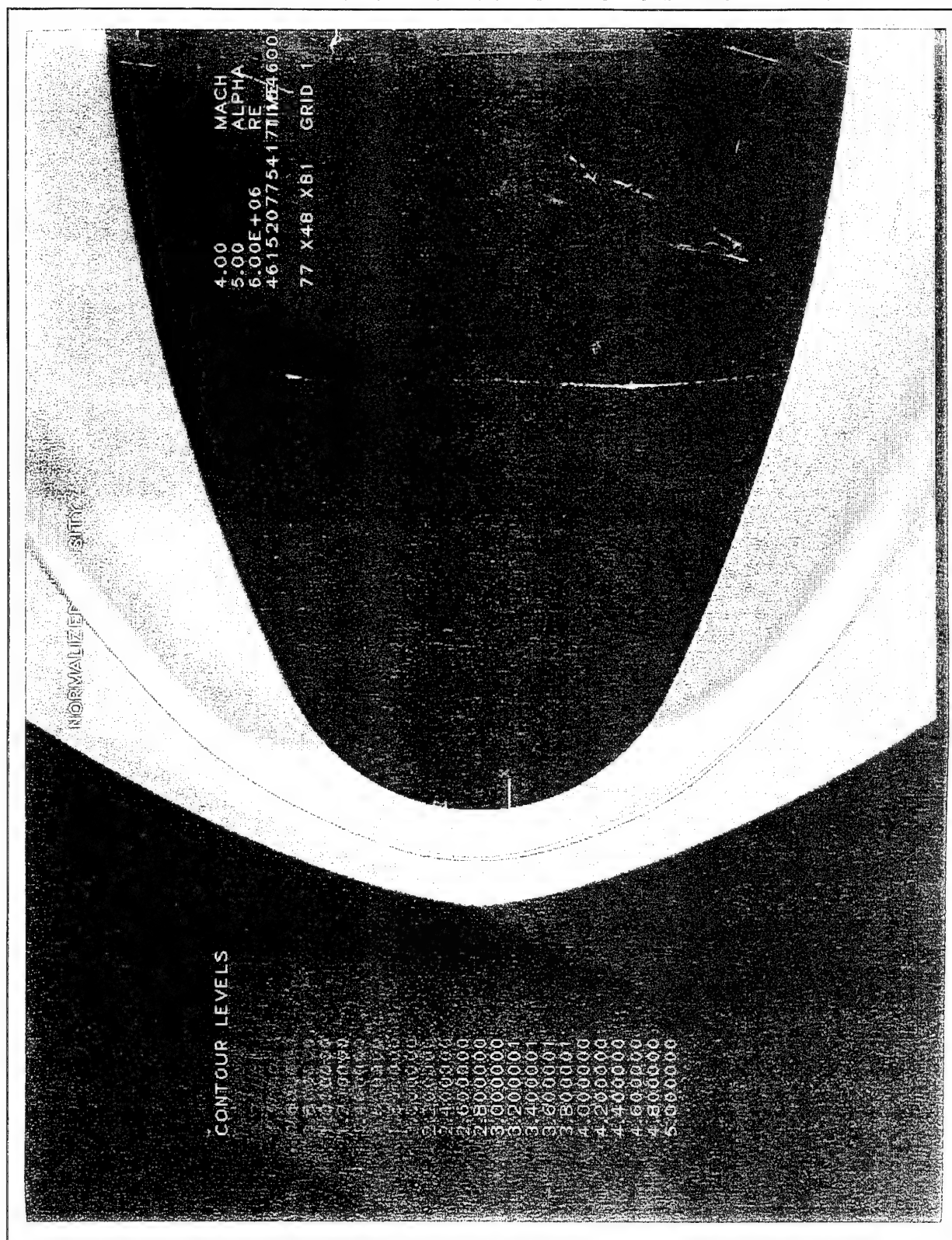


Figure 4-14. Hemispherical dome temperature field for a Mach 4 seeker with 5° angle-of-attack obtained by solving the Thin-Layer Navier-Stokes equations.

Figure 4-15. Thin-Layer Navier-Stokes density flow field solution for the Hemisphere-Ogive body at 5° angle-of-attack ($Mach=4.0$, $77 \times 48 \times 81$ adapted grid).



E. VALIDATION

In order to validate the computation, a comparison between the predicted flow field about the missile nose and experiments was tried. After an exhaustive library search no data suitable for comparison with the computation was found in the open literature. Most experiments were performed at hypersonic speeds. The only suitable experimental data to compare with the flow field computation were ones for a hemisphere-cylinder at $M_\infty = 1.2$ and a $Re = 5.4 \times 10^6$ ft. For this comparison a $61 \times 7 \times 41$ inviscid grid was created. The experimental data was taken from shadowgraphs obtained in the AEDC Aerodynamic Wind Tunnel (1T)[18].

A plot of the shock standoff distance at both the body axis and the wind axis for a hemisphere-cylinder at Mach 1.2 is shown in Fig. 4-17. The normalized standoff distance, Δ/R for zero incidence is -1.26. The flow was computed using a $61 \times 7 \times 41$ inviscid grid. The computed normalized standoff distance was -1.0. The poor result is considered to be due to lack of resolution of the grid near the shock front. Due to restrictions of time another grid was not generated to try another comparison. Fig. 4-16 shows the computed Mach number distributions using the inviscid Euler solution.

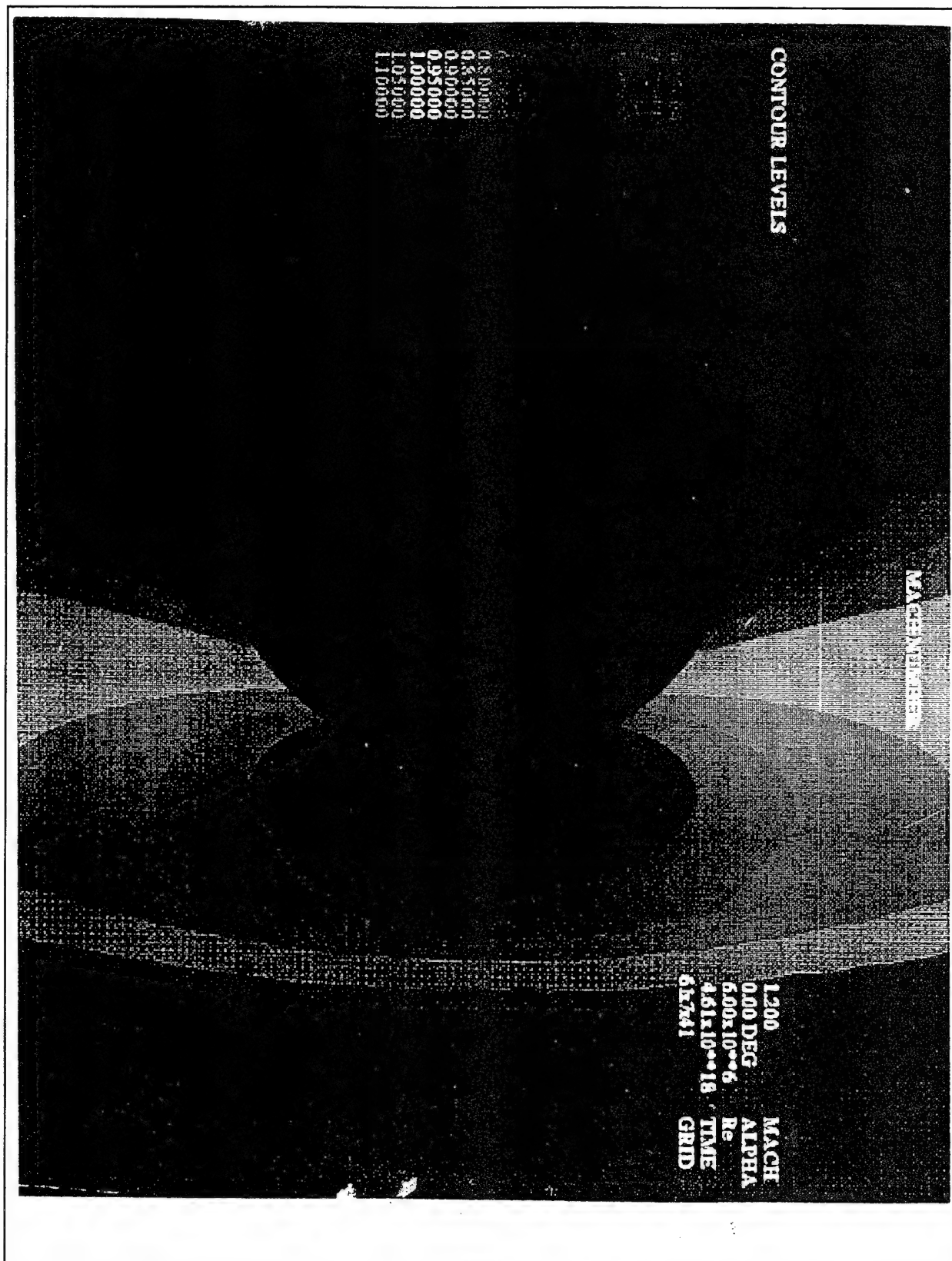


Figure 4-16. Hemisphere-Cylinder Euler solution of the Mach Number flow field (61x7x41 grid).

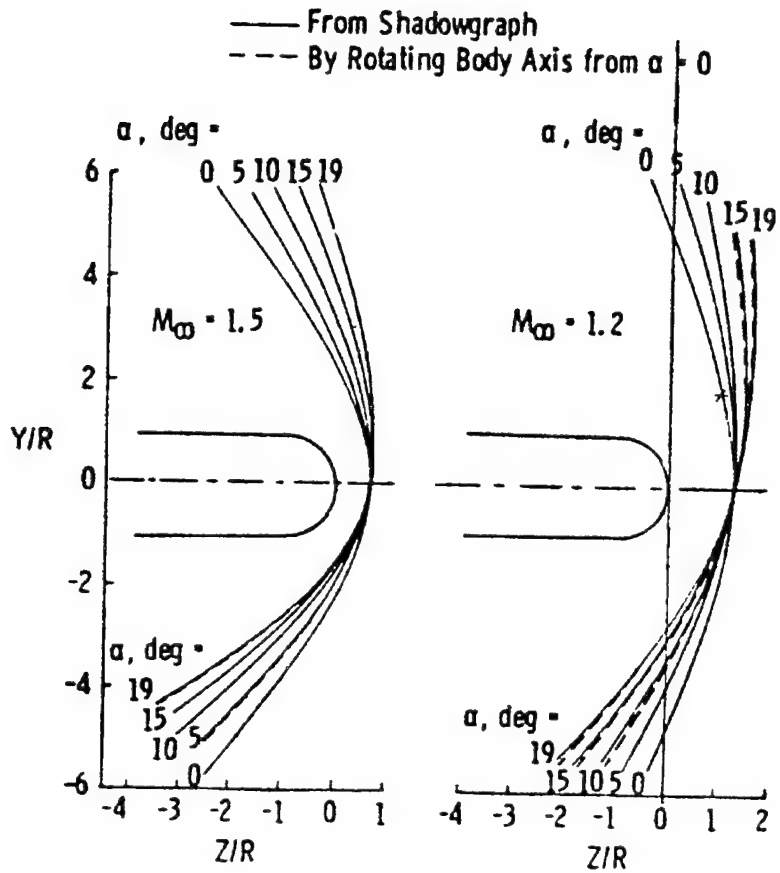


Figure 4-17. Shock standoff distances about Hemisphere-Cylinder at incidence from shadowgraphs[18].

V. INFRARED SEEKER DETECTION PERFORMANCE DEGRADATION

The major effect of the increase in dome temperature on the IR seeker sensing performance at high supersonic speeds is considered to be thermal emission to the detectors. This increased dome radiation contributes to the noise and thus increases the Noise Equivalent Irradiance (*NEI*) to the detector or Noise Equivalent Quantum Flux (*NEQF*) to the detector array, decreasing the effective detectivity of the vehicular sensor and thus decreasing the detection range of the seeker.

Initially the basic figure of merit parameters will be introduced. Then a discussion of the range equations for non-imaging and imaging sensors in a high speed flight environment will follow. Several computations of detection ranges for a staring sensor are carried out for a range of mean dome temperatures, representing a range of missile speeds up to Mach 4.

A. SENSOR PERFORMANCE PARAMETERS

It is convenient to introduce the seeker sensor figures of merit before starting an analysis of the seeker performance.

1. Basic Figures of Merit

A basic figure of merit that applies to all detectors with electrical output is responsivity. Responsivity is the ratio of the output (usually in amperes or volts) to the radiant input (in watts). The spectral voltage responsivity of a detector at a given wavelength λ is the measured voltage output, V_s , divided by the spectral radiant power incident on the detector, $\Phi_e(\lambda)$ [29]:

$$\mathfrak{R}_v(\lambda, f) = \frac{V_s}{\Phi_e(\lambda)} \quad (5-1)$$

where f is the modulation frequency.

The noise equivalent power (NEP) of a detector is the required power incident on the detector to produce an average signal output equal to the rms noise output. Stated another way, the NEP is the signal power level that produces a signal-to-noise ratio of 1. The voltage signal output is

$$V_s = \mathfrak{R}_v \Phi_e \quad (5-2)$$

so the signal-to-noise ratio is

$$S/N = \frac{\mathfrak{R}_v \Phi_e}{V_{RMS}} \quad (5-3)$$

The NEP is the incident radiant power, Φ_e , for a signal-to-noise ratio of 1:

$$1 = \frac{\mathfrak{R}_v NEP}{V_{RMS}} \quad (5-4)$$

Solving for NEP gives

$$NEP = \frac{V_{RMS}}{\mathfrak{R}_v} \quad (5-5)$$

where V_{RMS} is the root-mean-square noise voltage in volts and \mathfrak{R}_v is the voltage responsivity in volts per watt.

The detectivity D of a detector is defined as the reciprocal of the noise equivalent power:

$$D = \frac{1}{NEP} \quad [W^{-1}]. \quad (5-6)$$

A more useful performance parameter is the normalized detectivity D^* (pronounced dee-star) which normalizes D to the detector area A_d and noise bandwidth, Δf , as follows,

$$D^* = D \sqrt{A_d \Delta f} = \frac{\sqrt{A_d \Delta f}}{NEP}, \quad (5-7)$$

given in units of $cm \cdot Hz^{1/2}/W$.

The NEP can be divided by the area of the collecting aperture, A_o , leading to a parameter called *noise equivalent irradiance* (NEI) [27],

$$NEI = \frac{NEP}{A_o}. \quad (5-8)$$

2. Noise Equivalent Temperature Difference (NETD)

The most widely used radiometric measure of the ability of a military mid-IR system to discriminate small signals in noise is the *Noise-Equivalent Temperature Difference* or *Noise-Equivalent Differential Temperature*. As defined by J. M. Lloyd [22], "The *NETD* is the blackbody target-to-background temperature difference in a standard test pattern which produces a peak-signal to rms-noise ratio (*SNR*) of one at the output of a reference electronic filter when the system views the test pattern".

In terms of system parameters the ratio of the differential

signal voltage to the detector rms noise voltage in the detector can be expressed, for a rectangular detector, as[22]

$$\frac{\Delta V_s}{V_n} \cdot \Delta T \frac{\alpha \beta A_o}{\pi \sqrt{ab} \Delta f_R} \int_0^\infty \frac{\partial M_\lambda}{\partial T} D^*(\lambda) \tau_o(\lambda) d\lambda \quad (5-9)$$

where α, β = detector angular subtenses [radian]
 a, b = detector dimensions [cm]
 $D^*(\lambda)$ = specific detectivity as a function of wavelength, evaluated at the electrical frequency at which the noise voltage spectrum of the detector is normalized to unity [cm Hz^{1/2} / W]
 Δf_R = equivalent noise bandwidth [Hz] of the NETD test reference filter
 A_o = effective area of the collecting aperture [cm²]
 $M_\lambda(\lambda)$ = spectral radiant exitance [W/μm·cm²]
 $\tau_o(\lambda)$ = spectral transmittance of the optics.

The NETD is defined as the temperature difference for unity SNR, so we can set $\Delta V_s/V_n = 1$ and solve for the resulting ΔT , which is by definition the NETD:

$$NETD = \frac{\pi \sqrt{ab} \Delta f_R}{\alpha \beta A_o \int_0^\infty \frac{\partial M_\lambda}{\partial T} D^*(\lambda) \tau_o(\lambda) d\lambda} \quad (5-10)$$

The spectral radiant exitance, M_λ , is defined by Planck's blackbody radiation law

$$M_{\lambda}(\lambda, T) = \left(\frac{2\pi h c^2}{\lambda^5} \right) \left(\frac{1}{e^{hc/\lambda kT} - 1} \right) \left[\frac{W}{\mu m \text{ cm}^2} \right]. \quad (5-11)$$

This last equation is more conveniently expressed in units of $[W/cm^2\mu m]$ for λ in $[\mu m]$ as:

$$M_{\lambda}(\lambda, T) = \frac{c_1}{\lambda^5 (e^{c_2/\lambda T} - 1)} \quad (5-12)$$

where $c_1 = 3.7415 \times 10^4$ [watt $\mu m^4 / cm^2$]

$c_2 = 1.4388 \times 10^4$ [μm K].

The noise equivalent temperature difference, *NETD*, representing the total output temporal and pixel(spatial) noise at a given background temperature converted into an equivalent temperature difference at the background scene, is a very effective figure of merit for a staring focal plane array (FPA).

3. Noise Equivalent Quantum Flux for a CCD Array

To develop such an array figure of merit (FOM), an appropriate performance measure for a single pixel should be introduced first. The figure of merit for a charge couple device (CCD) array should take into consideration the filling efficiency of the array, spatial resolution limit, modulation transfer function, quantum efficiency and integration time[29]. A performance measure for a single pixel may be used as a normalization factor for the array modulation transfer function (MTF) response at zero spatial frequency. As a starting point the voltage responsivity \mathfrak{R}_V^p of a single pixel can be expressed as

$$\mathcal{R}_V = \frac{V_D}{E_p} \quad [V \text{ photon}^{-1} \text{ sec cm}^2] \quad (5-13)$$

where V_D is the voltage output of the device, and E_p is the uniform photon irradiance on the device [$\text{photon sec}^{-1} \text{ cm}^{-2}$]. If monochromatic irradiance is considered, the expression for the output voltage of a pixel can be rewritten as[29]

$$V_D = E_p(\lambda) \Delta x \Delta y t_{\text{integ}} \eta e (CE) \quad [V] \quad (5-14)$$

where $\Delta x \Delta y$ is the resolution element area, t_{integ} is the integration time, η , is the quantum efficiency, e is the electronic charge and CE is the conversion efficiency of the output preamplifier ($V/\text{electron}$). The quantum efficiency is defined as the probability that a photoelectron is produced when a photon is incident on the detector. Substituting V_D in the responsivity expression Eq.(5-13), the spectral array photon responsivity can be expressed as

$$\mathcal{R}_p^{\text{array}} = \frac{V_D}{E_p(\lambda)} = \Delta x \Delta y t_{\text{integ}} \eta e (CE) \quad [V \text{ photon}^{-1} \text{ cm}^2 \text{ sec}]. \quad (5-15)$$

The responsivity, $\mathcal{R}_p^{\text{array}}$, in Eq.(5-15) is valid for a pixel or for an array at zero spatial frequency. To include the resolution effects would require that the responsivity would be multiplied by the MTF of the array in two orthogonal directions, thus getting two expressions for spectral array photon responsivity in the x and y directions.

The noise equivalent quantum flux (NEQF) is the counterpart of the NEP for a focal plane array. The NEQF is defined as

$$NEQF \cdot \frac{\text{noise}}{\mathfrak{N}_p^{\text{array}}} \quad [\text{photons sec}^{-1} \text{ cm}^{-2}] \quad (5-16)$$

where $NEQF$ has units of photon $\text{sec}^{-1} \text{ cm}^{-2}$ and noise is in V.

The voltage noise of the device is caused by all the contributors shown in Fig. 5-1. A detailed discussion of the detector noise can be found in references[22][27][29]. Hence

$$\text{noise} \cdot \sqrt{\Delta n_n^2} CE \quad [V] \quad (5-17)$$

where Δn_n^2 is the sum of all the noises in quadrature in units of electrons (statistical independence).

Substituting Eq.(5-15) and Eq.(5-17) in Eq.(5-16) one finds

$$NEQF \cdot \frac{\sqrt{\Delta n^2}}{\Delta x \Delta y t_{\text{integ}} \eta} \quad [\text{photons cm}^{-2} \text{ sec}^{-1}] \quad (5-18)$$

This is the photon irradiance flux on the array that would give a signal-to-noise ratio of 1, and is a measure of the minimum photon irradiance level that can be detected. The threshold signal-to-noise level will still be required for detection. The value of η will depend on the operating conditions.

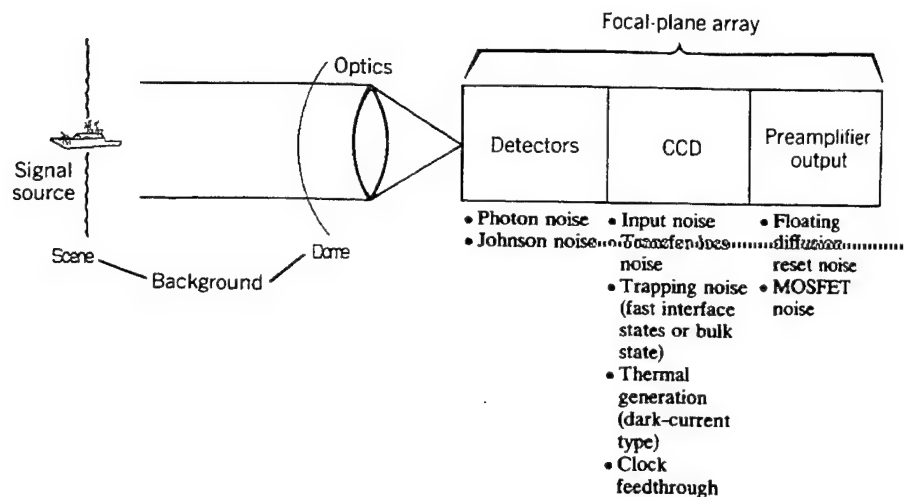


Figure 5-1. Noise sources in a IR seeker using a CCD.

In the case of *background-limited infrared photodetection operation* (BLIP) the dominant noise is shot or G-R noise associated with the photon irradiance. One can then write the NEQF as,

$$NEQF = \frac{\sqrt{2G^2\eta E_p \Delta x \Delta y t_{integ}}}{\Delta x \Delta y t_{integ} \eta} \quad (5-19)$$

$$NEQF = G \sqrt{\frac{2E_p}{\Delta x \Delta y t_{integ} \eta}} \quad (5-20)$$

where G is the photoconductive gain ($G=1$ for photovoltaic operation, and $0 < G < 1$ for photoconductor operation), and t_{integ} is the integration time.

A photoconductor which exhibits performance at theoretical limits is said to operate in the BLIP mode. In this case the

background photon flux and the atmospheric transmission determine the detector noise. In this circumstance the fluctuations in incident photon flux can be the dominant source of noise. For the case of an IR seeker where most of the field of view contains background and not signal photons, and where the background photon flux due to dome emission is significantly high, the term BLIP is truly appropriate. This is further enhanced by the fact that the IR sensor, in current systems, is cooled well below ambient temperature.

B. SIGNAL-TO-NOISE RATIO DEGRADATION DUE TO DOME EMISSION

In a high speed flight situation ($M_\infty > 1.2$) the missile heats up due to aerodynamic heating. As was discussed in Chapter I, the temperature rise is particularly severe in the stagnation regions as happens with the IR dome. As the dome heats up, it will emit gray-body radiation over the entire electromagnetic spectrum. This will degrade the IR sensor performance in terms of detection and tracking ability. The effect of background-induced noise from the hot dome on the sensor performance has been characterized and explained by some authors, in particular Dr. Claude Klein. This section and the nonimaging range equation subsection summarizes some of his work.

With the assumption that the seeker system has a wavelength-independent optical efficiency over the spectral bandpass, that the sensor subsystem is detector-noise limited, and that all detector elements operate in a BLIP mode, the peak-signal to rms-noise ratio obtained at the output terminals of the signal-processing unit can be expressed as follows[4]:

$$SNR = \frac{H_{eff}}{NEI} . \quad (5-21)$$

Here the symbol H_{eff} [W/cm²] designates the net effective irradiance originating from the target,

$$H_{eff} = \int_{\lambda_1}^{\lambda_2} (\lambda/\lambda_p) H_\lambda \tau_p d\lambda \quad (5-22)$$

where τ_p is the path transmittance and H_λ is the spectral irradiance originating from the target and measured at the collecting aperture. NEI is the noise-equivalent irradiance,

$$NEI = NEI_o \sqrt{\Phi/\Phi_o} \quad (5-23)$$

referred to the peak-response wavelength of the detector package, λ_p , and expressed in terms of the laboratory-measured NEI_o and the background photon-flux ratio Φ/Φ_o . Under laboratory conditions there is no sunlight, and the system is in thermal equilibrium (the seeker and its surroundings are at the same temperature). Under background-limited conditions (BLIP), the noise voltage is seen to be proportional to the square root of the flux of incident background photons (Poisson photon statistics), so that the signal-to-noise ratio (SNR) in the presence of hot IR dome radiation can be derived from the "dark-system" SNR simply in the form

$$SNR = \frac{SNR_o}{\sqrt{\Phi/\Phi_o}} . \quad (5-24)$$

The ratio Φ/Φ_o thus determines the performance degradation induced by environmental factors and must be evaluated with some care. Let one consider that the noise-generating photons originate from three distinct sources: the detector surroundings, the background scene, and the hot dome. In terms of spectral quantum irradiances, the total effective photon-flux density Φ thus amounts to

$$\Phi = \int_{\lambda_1}^{\lambda_2} (\Phi_{\lambda,B} + \Phi_{\lambda,D} + \Phi_{\lambda,S}) d\lambda \quad (5-25)$$

where the terms in the integrand refer to the spectral photon flux contributions from the background, dome and detector surroundings respectively. The temperature distribution on the dome in practical designs does not vary significantly. So the dome can be considered to be at a uniform, averaged temperature T_D . The spectral region of interest usually is narrow enough, implying that the emittance does not change significantly, so the photon flux can be expressed in the following compact manner[4],

$$\frac{\Phi}{\Phi_o} = \tau_o \frac{(1 - \bar{\epsilon}) Q(T_B) + (1/\tau_o - 1) Q(T_S) + \bar{\epsilon} Q(T_D)}{Q(T_o)} \quad (5-26)$$

Here $\bar{\epsilon}$ represents average dome emissivity, τ_o is the transmission of the optics (about 50% for state-of-the-art seekers), $Q(T)$ represents the effective quantum exitance at absolute temperature T defined as

$$Q = \int_{\lambda_1}^{\lambda_2} Q_{\lambda} d\lambda \quad [\text{photons/cm}^2 \cdot \text{sec}] \quad (5-27)$$

Under laboratory-type conditions, the effective background photon-flux density received by a radiation-shielded detector amounts to [26]

$$\Phi_o = (NA)^2 \tau_f \int_{\lambda_1}^{\lambda_2} Q_{\lambda} (T_o) d\lambda, \quad (5-28)$$

Here NA is the numerical aperture of the optical system and τ_f represents the (cold) filter transmittance, assuming ideal spatial shielding and spectral filtering.

C. TARGET ACQUISITION RANGE DEGRADATION DUE TO DOME EMISSION

1. Range Equation for Non-Imaging Systems

A point target of spectral radiant intensity J_{λ} gives rise to a spectral irradiance

$$H_{\lambda} = \frac{J_{\lambda} \tau_p}{R^2} \quad (5-29)$$

at the collecting aperture of the seeker system, where τ_p represents the overall path transmittance, including the IR dome losses, and R is the target-collector range. Hence, and in accordance with Eqs. (5-20) and (5-21), we have

$$J_{eff} = \int_{\lambda_1}^{\lambda_2} (\lambda/\lambda_p) J_{\lambda} \tau_p d\lambda \quad (5-30)$$

where J_{eff} refers to a net effective apparent target radiant intensity defined as follows:

$$SNR = \frac{J_{eff} / R^2}{NEI} . \quad (5-31)$$

The effective radiant intensity varies with slant range and IR dome temperature through the path transmittance τ_p . Target acquisition at a given probability of detection and a fixed false-alarm rate requires a minimum signal-to-noise ratio $(SNR)_{acq}$. It follows that the detection or acquisition range is a solution of Eq.(5-29). If R_o now designates the acquisition range for the "cold" system obtained under laboratory-type conditions, the degradation induced by heating up of the IR dome can be characterized by[25]

$$\frac{R}{R_o} = \left[\frac{1}{NEI / (NEI)_o} \right]^{1/2} , \quad (5-32)$$

(neglecting path transmittance variation). Using the relationship from Eq.(5-31)

$$R = \left[\frac{J_{eff}(R, T_d)}{(SNR)_{acq} (NEI)} \right]^{1/2} \quad (5-33)$$

so that using Eq.(5-21),

$$\frac{R}{R_o} = \frac{1}{(\Phi/\Phi_o)^{1/4}} , \quad (5-34)$$

since J_{eff} is a relatively weak function of both R and T_d , for scenarios of practical interest.

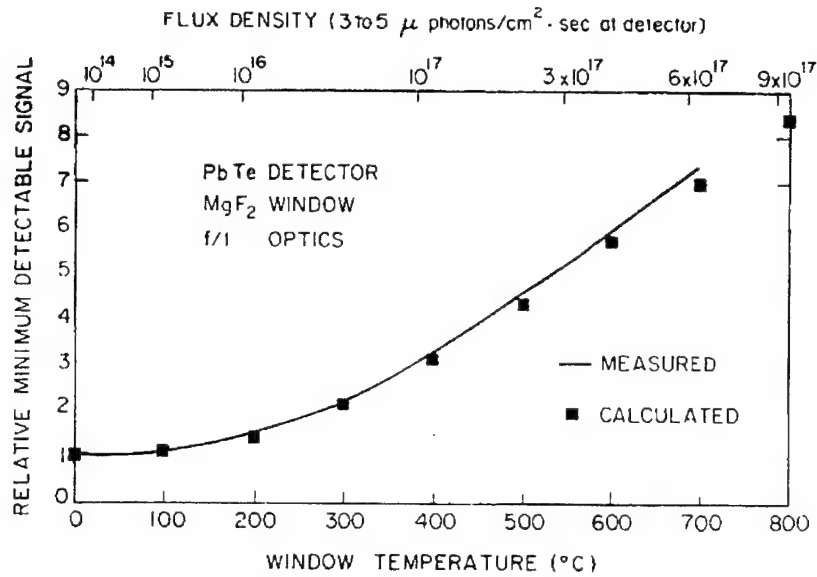


Figure 5-2 Photosaturation characteristics of a lead telluride detector subjected to background illumination originated from a hot magnesium fluoride window[26].

The dark-system NEI relates to design parameters in the following manner[25]:

$$(NEI)_o \sim \frac{[(\Delta f)_n A_d]^{1/2}}{A_o \tau_o \eta_e D^*(\lambda_p)} \quad (5-35)$$

where $D^*(\lambda_p)$ refers to the peak specific detectivity of the sensor package, under conditions of thermal equilibrium, at room temperature, and η_e is an electric response factor.

Figure 5-2 shows calculated and computed minimum detectable signal power relative to minimum detectable signal power in the absence of window radiation[26]. This example shows the strong effect of the dome emission on detection and tracking.

2. Range Equation for Imaging Systems

The *NETD* Eq.(5-10) is valid either for a BLIP or a non-BLIP detector. In this section the *NETD* for a BLIP detector irradiated by a hot window will be derived. As will be shown the range equation for an imaging system will be *NETD* dependent.

The theoretical limit for D^* for a photoconductor is

$$D^*(\lambda) = \frac{\lambda}{2hc} \left(\frac{\eta_q}{Q_B} \right)^{1/2}, \quad (5-36)$$

where η_q is the quantum efficiency and Q_B is the background quantum flux density [photons/cm²sec] incident on the detector. The severity of the IR seeker signal-to-noise-ratio limited application dictates that a cold filter, with appropriate spectral response, should be placed immediately preceding the detector. The Q_B is given then by

$$Q_B = \left[\frac{\Omega_{cs}}{\pi} \right] \int_0^{\lambda_p} \tau_{co} Q_\lambda(T_B) d\lambda, \quad (5-37)$$

where it assumed that the detector is a Lambertian receiver with an effective collecting solid angle of π , and where Ω_{cs} is the ideal effective angle to which the detector cold shield reduces reception of background radiation, and τ_{co} is the transmittance of the cold filter. At this point, it is convenient to define the several individual transmittances that affect the sensor performance. The total spectral optical transmittance τ_o can be decomposed in the following product

$$\tau_{o,\lambda} \cdot \tau_{co,\lambda} \cdot \tau_{uc,\lambda} \cdot \tau_{d,\lambda} (T_D) \quad (5-38)$$

where $\tau_{uc,\lambda}$ is the spectral transmittance of the uncooled optics and $\tau_{d,\lambda}(T_D)$ is the average spectral transmittance of the dome at an averaged absolute temperature T_D .

In this analysis it is assumed that the detector is a photoconductor having theoretical performance such that

$$D^*(\lambda) = \frac{\lambda D^*(\lambda_p)}{\lambda_p} \quad \text{for } \lambda \leq \lambda_p \\ = 0 \quad \text{for } \lambda > \lambda_p . \quad (5-39)$$

Substituting for Q_B in the D^* Eq.(5-36) gives

$$D^*(\lambda) = \frac{\lambda}{2hc} \left[\frac{\pi}{\Omega_{CS}} \right]^{1/2} \frac{\eta_q^{1/2}}{\left[\int_0^{\lambda_p} \tau_{co} Q_\lambda (T_B) d\lambda \right]^{1/2}} . \quad (5-40)$$

A normalized detectivity parameter, $D^{**}_{BLIP}(\lambda)$, for unity quantum efficiency and for an effective cold shielded angle of π steradians is defined by[22]

$$D^{**}_{BLIP}(\lambda) = \frac{\lambda}{2hc} \frac{1}{\left[\int_0^{\lambda_p} \tau_{co} Q_\lambda (T_B) d\lambda \right]^{1/2}} . \quad (5-41)$$

Expressing $D^*(\lambda)$ in terms of $D^{**}(\lambda)$

$$D^*(\lambda) = \left[\frac{\Pi}{\Omega_{CS}} \right]^{1/2} \eta_q^{1/2} D_{BLIP}^{**}(\lambda) \quad (5-42)$$

Substituting for $D^*(\lambda_p)$ in the NETD equation yields

$$NETD = \frac{\Pi^{1/2} \sqrt{ab \Delta f_R \Omega_{CS}}}{\alpha \beta A_o \tau_o \eta_q^{1/2} D_{BLIP}^{**}(\lambda_p)} \frac{\Delta M}{\Delta T} \quad (5-43)$$

Here $\Delta M/\Delta T$ is defined as

$$\frac{\Delta M}{\Delta T} = \int_{\lambda_1}^{\lambda_2} \frac{\partial M_\lambda(T_B)}{\partial T} \frac{D^*(\lambda)}{D^*(\lambda_p)} d\lambda \quad (5-44)$$

where

$$\frac{\partial M_\lambda(T_B)}{\partial T} = M_{BB,\lambda} \frac{c_2 e^{c_2/\lambda T}}{\lambda T^2 (e^{c_2/\lambda T} - 1)} \quad (5-45)$$

gives the effective change in spectral radiant emittance with temperature. ΔT is the temperature difference between the target and the background. Using the relation in Eq.(5-39), Eq.(5-44) can be simplified to

$$\frac{\Delta M}{\Delta T} = \int_{\lambda_1}^{\lambda_2} \frac{\partial M_\lambda(T_B)}{\partial T} \frac{\lambda}{\lambda_p} d\lambda \quad (5-46)$$

The cold shield efficiency η_{CS} is defined in terms of the actual cold shield angle Ω_p , as

$$\eta_{CS} = \frac{\Omega_p}{\Omega_{CS}} \quad (5-47)$$

where $\Omega_{CS} = a \cdot b / f^2$.

The perfect cold shield is defined as one which limits reception of background radiation to the cone defined by the optical system aperture ratio, F_n (f/number). Thus for an optical system with circular aperture of diameter D_o and focal length f

$$\Omega_p = \frac{\pi D_o^2}{4f^2} \quad (5-48)$$

and substituting in Eq.(5-43) gives [22]

$$NETD = \frac{2 \sqrt{\Delta f_R}}{\sqrt{\alpha\beta} D_o \tau_o \eta_{CS}^{1/2} \eta_q^{1/2} D_{BLIP}''(\lambda_p)} \frac{\Delta M}{\Delta T} \quad (5-49)$$

Applying the same definition to D^* gives

$$D^*(\lambda) = 2 F_n (\eta_{CS} \eta_q)^{1/2} D_{BLIP}''(\lambda) \quad (5-50)$$

The Eq.(5-49) can be rewritten

$$NETD = \frac{4 F_n \sqrt{\Delta f_R}}{\sqrt{\alpha\beta} D_o \tau_o D^*(\lambda_p)} \frac{\Delta M}{\Delta T} \quad (5-51)$$

To account for the effect of the hot dome on the *NETD* the background quantum flux density from the dome emission should be added to the background quantum flux density from the scene background in the D^* Eq.(5-36). With the cold shield, the background quantum flux density that irradiates the detector has two

contributions:

$$Q_B = Q_{BB} + Q_D \quad (5-52)$$

where Q_{BB} is the quantum flux density originated by a uniform blackbody background corresponding to the scene at temperature T_{BB} , Q_D is the portion of the background quantum flux density originated by the dome with a uniform mean temperature T_D . These quantities are defined as follows [25]:

$$Q_{BB} = \left[\frac{\Omega_{CS}}{\Pi} \right] \int_{\lambda_1}^{\lambda_2} \tau_{CO} \frac{c_3}{\lambda^4 (e^{c_2/\lambda T_{BB}} - 1)} d\lambda \quad (5-53)$$

$$Q_D = \left[\frac{\Omega_{CS}}{\Pi} \right] \int_{\lambda_1}^{\lambda_2} \tau_{CO} \bar{\epsilon} \frac{c_3}{\lambda^4 (e^{c_2/\lambda T_D} - 1)} d\lambda \quad (5-54)$$

with radiometric constant c_2 as defined before and $c_3 = 1.8837 \times 10^{23} \mu\text{m}^3/\text{sec} \cdot \text{cm}^2$, $\bar{\epsilon}$ is the mean dome emissivity with an averaged temperature, T_D . λ_1 and λ_2 are the cut-on and cut-off wavelengths of the filter. Substituting in Eq.(5-38) yields

$$D(\lambda) = \frac{\lambda}{2\Pi c} \left[\frac{\Pi}{\Omega_{CS}} \right]^{1/2} \frac{\eta_q^{1/2}}{\left[\int_{\lambda_1}^{\lambda_2} \tau_{oc} (Q_{BB,\lambda} + Q_{D,\lambda}) d\lambda \right]^{1/2}} \quad (5-55)$$

which can be used to express $NETD$ from Eq.(5-50) in terms of photon flux components.

Typically the optical system installed in the seeker is a

modified Cassegrain telescope. This will introduce some energy losses characterized by the circular aperture attenuation coefficient, $K(cir)$, and a Cassegrain obscuration coefficient $K(cas)$. If these losses are considered, the general $NETD$ becomes

$$NETD = \frac{8(hc)^{1/2}}{\pi^{1/2}c_2} \frac{Fn(\Omega_{CS})^{1/2}\tau_{CO}^{1/2}}{\sqrt{\alpha\beta}D_o\tau_o K(cas)K(cir)} \left(\frac{\Delta f_R}{\eta_q}\right)^{1/2} \frac{\left[\int_{\lambda_1}^{\lambda_2} \lambda [M_{BB,\lambda}(T_{BB}) + M_{D,\lambda}(T_D)] d\lambda\right]^{1/2}}{\int_{\lambda_1}^{\lambda_2} \frac{1}{T_{BB}^2} M_{BB,\lambda} \frac{e^{c_2/\lambda T_{BB}}}{e^{c_2/\lambda T_{BB}} - 1} d\lambda} \quad (5-56)$$

where τ_{oc} is the cold optics transmittance (under laboratory conditions), τ_o is the optics transmittance (during operation), $M_{BB,\lambda}$ and $M_{D,\lambda}$ are the spectral radiant exitances of the background and of the dome respectively. Expanding the terms of the integrands of Eq.(5-56) another format to the general $NETD$ equation can be found,

$$NETD = \frac{8(hc)^{1/2}}{\pi^{1/2}c_2} \frac{Fn\Omega_{CS}^{1/2}\tau_{CO}^{1/2}}{\sqrt{\alpha\beta}D_o\tau_o K(cas)K(cir)} \left(\frac{\Delta f_R}{\eta_q}\right)^{1/2} \frac{\left[\int_{\lambda_1}^{\lambda_2} \lambda \left[\frac{1}{\lambda^5 (e^{c_2/\lambda T_{BB}} - 1)} + \frac{\bar{\epsilon}}{\lambda^5 (e^{c_2/\lambda T_D} - 1)} \right] d\lambda\right]^{1/2}}{\int_{\lambda_1}^{\lambda_2} \frac{1}{T_{BB}^2} \frac{e^{c_2/\lambda T_{BB}}}{(e^{c_2/\lambda T_{BB}} - 1)^2} d\lambda} \quad (5-57)$$

The last two expressions for the $NETD$ take into consideration the influence of radiation by an aerodynamically heated dome on the sensor. The added "background"-induced noise will lower the effective performance of the system in terms of detection range and imaging capability.

The signal-to-noise ratio at maximum detection range is

$$(SNR)_{acq} \cdot \frac{\Delta T \cdot \tau_p(R)}{NETD} \quad (5-58)$$

where $\tau_p(R)$ is the total atmospheric path transmission for the system spectral bandpass and R is the detection range. Here ΔT is the differential temperature of the target with respect to background. If ΔT is normalized with respect to the SNR , defining[30]

$$K_T \equiv \frac{\text{Differential Temperature}}{(SNR)_{acq}} = \frac{\Delta T}{(SNR)_{acq}} \quad (5-59)$$

and substituted in Eq.(5-58) then after rearranging one obtains

$$\tau_p(R) \cdot \frac{NETD}{K_T} \cdot \quad (5-60)$$

To solve for range, the total transmittance of the optical path should be determined first. For a given set of meteorological and oceanographic conditions, the transmittance falls exponentially with range, as follows

$$\tau_p(R) \cdot \alpha e^{-\beta R} \quad (5-61)$$

where α and β are constants to be determined. Substituting Eq.(5-61) in Eq.(5-60), gives

$$\alpha e^{-\beta R} \cdot \frac{NETD}{K_T} \quad (5-62)$$

Solving for R yields the range equation for an imaging system

$$R = \frac{\ln \alpha - \ln(NETD) - \ln(K_T)}{\beta} \quad (5-63)$$

in the form utilized by S. Smith[30].

D. DETECTOR NONUNIFORMITY NOISE

This noise is associated with the variation in output from pixel to pixel, or the variations across the entire array. It can be caused by two effects: (a) fixed pattern noise and (b) responsivity variations. The influence of nonuniformity on FPA performance may impair the detector of achieving theoretical (BLIP) sensitivity.

Nonuniformity limitations on the $NETD$ in many systems are more damaging than temporal noise since a pattern-noise-limited image cannot be improved by frame-to-frame averaging, whereas the sensitivity of a temporal-noise-limited imager can be improved by such averaging.

1. Fixed Pattern Noise

Fixed pattern noise is a nonuniformity appearing across the array which does not change with irradiance[29]. Several effects contribute to fixed pattern noise. Thermally generated carriers are not uniform across the array. Local defects in the semiconductor crystal lattice cause a variation in dark-current generation across the array.

A major contributor to fixed pattern noise is the errors in the

fabrication process. The errors introduced by inaccurate pixel areas caused by masking misalignments can lead to 10% nonuniformities. The fixed pattern noise is usually compensated by image processing.

2. Responsivity Variation

Responsivity variation is a nonuniformity which has a variable effect as a function of irradiance. The responsivity variation from pixel to pixel is determined by doping variations across the device. Compensation for responsivity is more difficult than for fixed pattern noise- requiring "two point" calibration as a minimum.

3. Residual Nonuniformity

After compensation the residual non-uniformity can be considered as a source of noise. This noise can be considered as an added percentage of photon noise, because it is considered to be correlated, in the following manner,

$$n_u = g (Q_{BB} + Q_D) \quad (5-64)$$

where n is the rms value of the noise in volt, g is the non-uniformity coefficient, Q_{BB} and Q_D are the background photon fluxes on the detector from the scene and seeker dome as defined before by Eq.(5-53) and Eq.(5-54) respectively. Array non-uniformity is a problem area that has been discussed extensively in the literature. For state-of-the art sensors the array non-uniformity coefficient varies between 0.01 and 0.0001[30].

E. COMPUTATION OF THE DETECTION RANGE

Acquisition range for an IR seeker of an air-to-surface anti-ship supersonic missile with a 256x256 CCD staring sensor was

E. COMPUTATION OF THE DETECTION RANGE

Acquisition range for an IR seeker of an air-to-surface anti-ship supersonic missile with a 256x256 CCD staring sensor was computed for a midlatitude scenario (LOWTRAN 6), in winter and summer, for two background-to-target normalized differential temperatures ($K_T=2.5$ and $K_T=4.0$) and for two missile flight profiles, level flight at 20 m and 3km altitude, and for a range of mean dome temperatures of 300, 600, 900, 1043 and 1200K, corresponding to missile flight speeds up to Mach 4.

The detection or acquisition range was computed using Eq.(5-63). To compute the *NETD* a MS-FORTRAN program developed, by S.T. Smith (Naval-Air Warfare Center, China Lake) was used. The program computes the *NETD* for different detector materials, integration times, dome materials, dome temperature, array nonuniformities, fill efficiency, background temperature, collector aperture and optical configurations. The *NETD* was computed for each set of parameters shown in Table 5-1, with LOWTRAN atmospheric transmission.

The total transmittance of the optical path was determined first. The LOWTRAN6 computer code was used to predict atmospheric transmittance. Figure 5-3 shows the total computed transmittance for a slant path from 3km altitude to sea level and for a horizontal path at 20 meters altitude for several ranges in a Navy Maritime environment(see Appendix B) in the 3.5-4.2 μm and 8.0-10.5 μm , for the midlatitude summer and winter models.

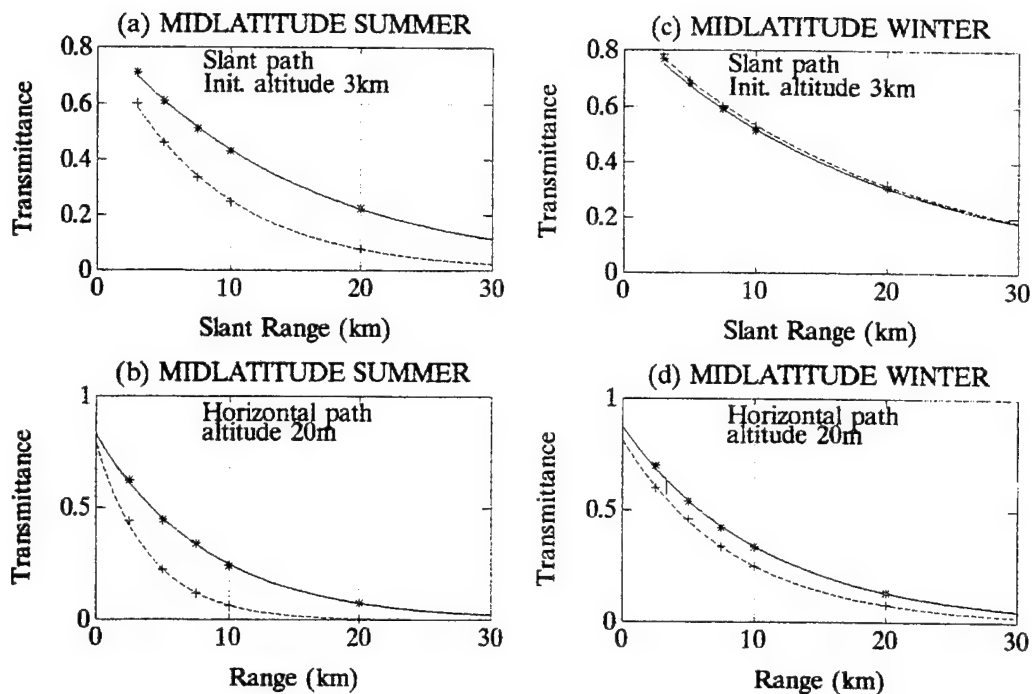


Figure 5-3. LOWTRAN 6 computed atmospheric transmittance. * 3.5-4.2 μ m + 8.0-10.5 μ m. Navy maritime aerosol model. (a)(b) Midlatitude Summer; visibility 44.2 km ; Humidity 76.2%; (c)(d) Midlatitude Winter; visibility 43.9km; Humidity 77.1%.

Using a least-squares fit, the coefficients α and β of Eq.(5-61) were computed for the four different scenarios for the two spectral bands. The curve-fit parameters for atmospheric transmission and the computed *NETD* for the each set of sensor parameters (see Table 5-1) and dome temperatures of 300, 600, 900, 1043 and 1200K, were used to compute the seeker detection range by applying Eq.(5-63). The selected dome materials were the sapphire and the diamond for the 3.5-4.2 μ m band and 8.0-10.5 μ m spectral band respectively. These materials were matched to the spectral bands where they exhibit better transmission properties. These materials are considered to withstand the severe thermal environments of

advanced, highly supersonic missiles. The temperature of 1144K was found in Chapter IV to be the mean dome temperature of the conceptual missile at Mach 4 at sea level.

The normalized differential temperatures, $K_T=2.5$ and $K_T=4.0$ were chosen for a SNR of 2.0. This implies that we are looking at temperature differences of 5.0K and 8.0K between the target and the background.

F. RESULTS AND DISCUSSION

Figure 5-4 through Fig.5-7 show the computed NETD for "residual" array nonuniformity coefficient after compensation of 0.1, 0.01, 0.001 and 0.0001 respectively for the two selected dome materials. Fig.5-8 through Fig.5-23 show the computed detection ranges for the seeker.

Before starting a detailed analysis of the detection range computation results it should be noticed that the values of the computed NETD depend on the area of the collector aperture(see Eq.(5-10)). So all the discussion relates to the nose shape and dimensions of the hemispherical nose configuration of Chapter IV. The quantitative results obtained cannot be immediately extrapolated to other seekers. However the results obtained show the trends and influence of the several system parameters on the IR seeker performance. A LRASM (Long Range Anti-Ship Missile) would enable the installation of a larger primary optical aperture resulting in better detection range and good resolution for imaging.

Analyzing the results it is clear that the array nonuniformity has strong effect on the seeker performance. The array nonuniformity

is particularly important at high supersonic speeds when the dome temperatures become particularly high. For the case of a Mach 4 missile the seeker becomes blind (detection range falls to zero) for residual array nonuniformities of 10 percent. For the other cases of improved array nonuniformity the detection range of the system improves considerably. The sapphire dome systematically shows a better performance than the diamond dome in terms of detection range.

In terms of environmental influence on the performance the winter condition with a slant path scenario gives the best results in opposition to the summer scenario for a sea-skimmer missile at an altitude of 20m.

The results show clearly that the designer should determine carefully the effect of array nonuniformity and the dome temperature reached during flight by the seeker.

The model used does not take into account target-to-background contrast reflectance. A better model should include this effect if a better target-to-background discrimination is desired. This effect is expected to be larger in the MWIR spectral band than the LWIR spectral band.

For aim-point considerations a minimum of 100 pixels on target is desired (Johnson criteria). To calculate the aim-point tracking range one should take into account the geometrical characteristics of the target and the instantaneous field of view of the seeker optical system.

FPA.....	256x256, 30 μ m pitch
Aperture Diameter	2.25 cm
FOV	4.46°
IFOV	0.2°
Diffraction limit blur	0.13mrad
Obscuration coefficient.....	0.1
Dome Material	
3.5 - 4.2 μ m band (Sapphire)	
8.0 - 10.5 μ m band (ZnS and Diamond)	
Detector Material	
3.5 - 4.2 μ m band	InSb
8.0 - 10.5 μ m band	HgCdTe
Array Nonuniformity	
0.001, 0.01, 0.10, 1.00	
Dwell Time	
Staring	4.0 ms
Dome shapes	
hemispherical	
elipsoidal	

Table 5-1. Seeker Parameters. Study Cases.

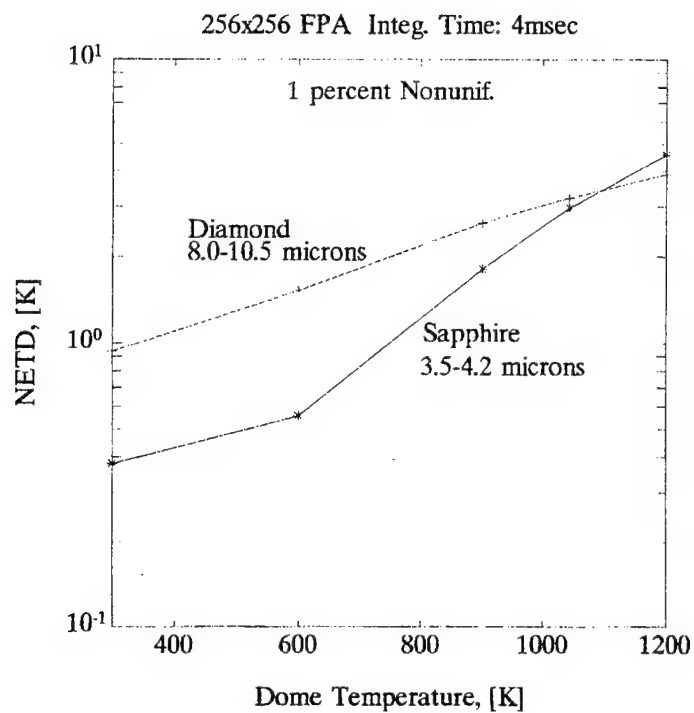


Figure 5-4

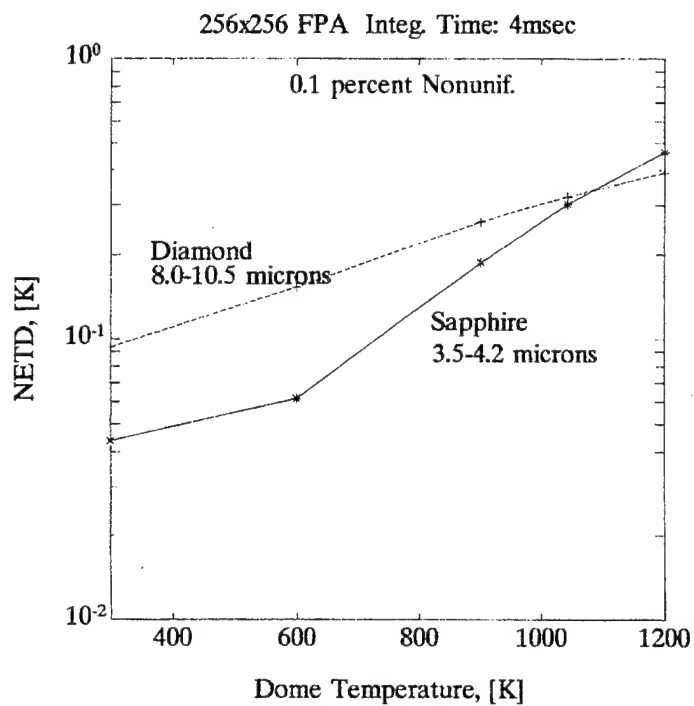


Figure 5-5

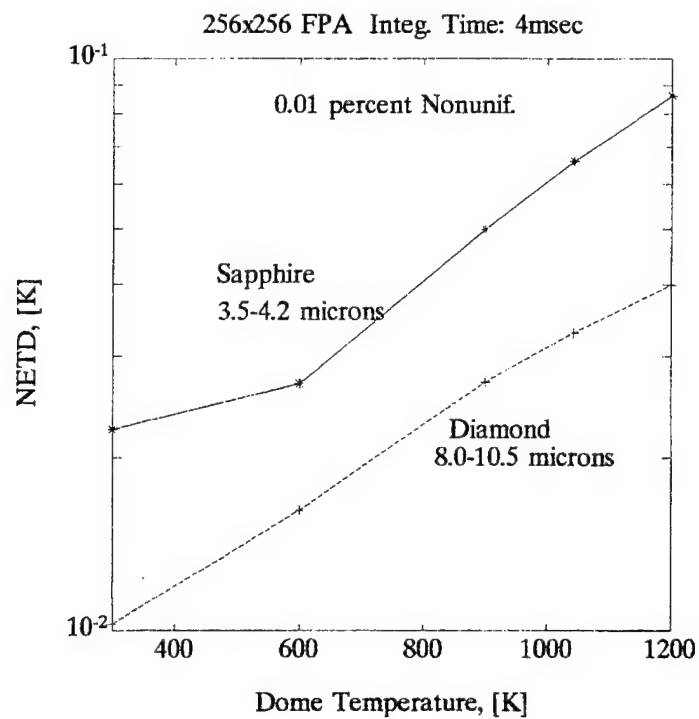


Figure 5-6

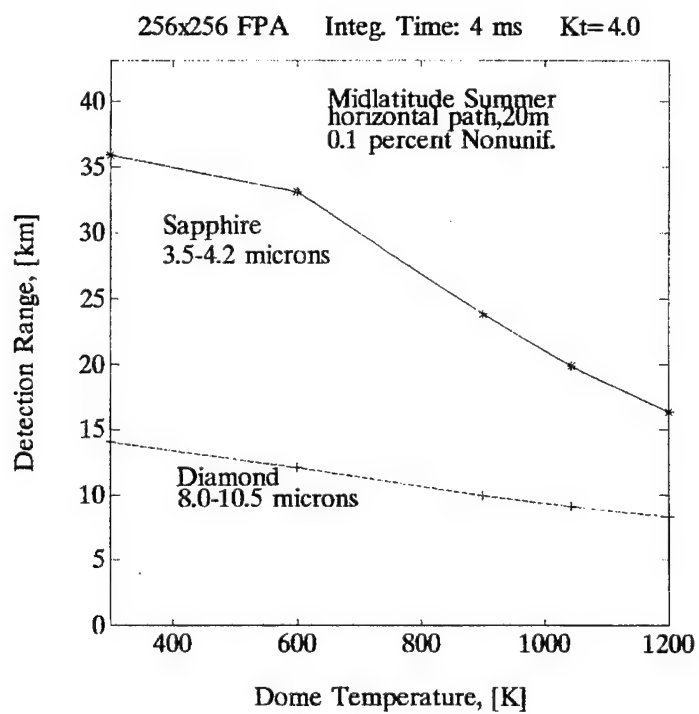


Figure 5-7

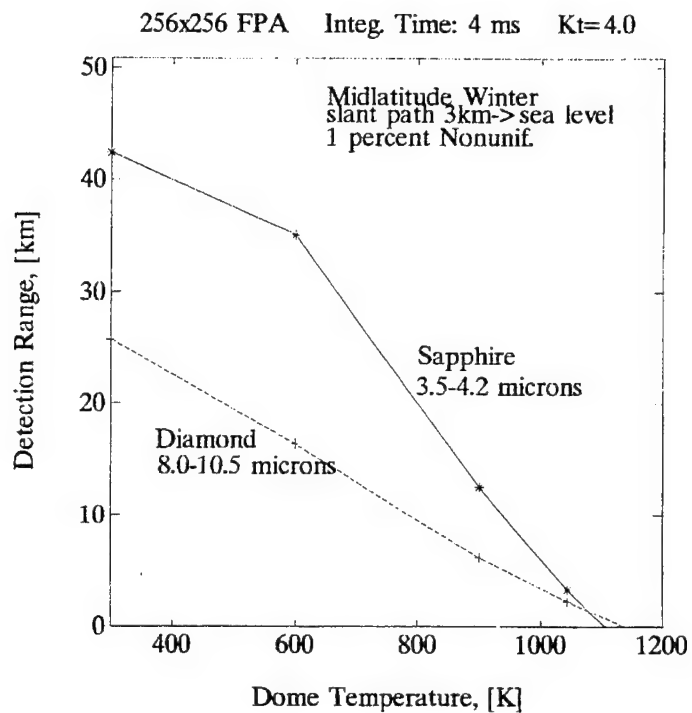


Figure 5-8

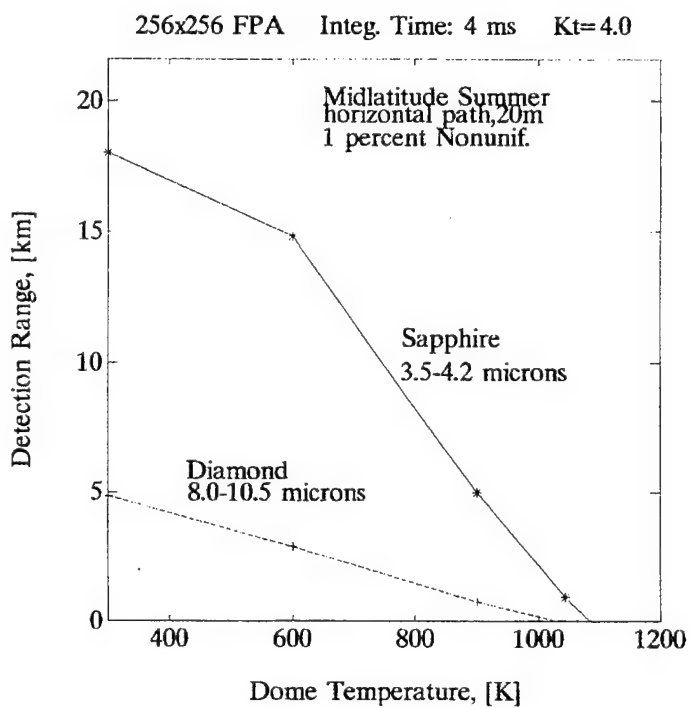


Figure 5-9

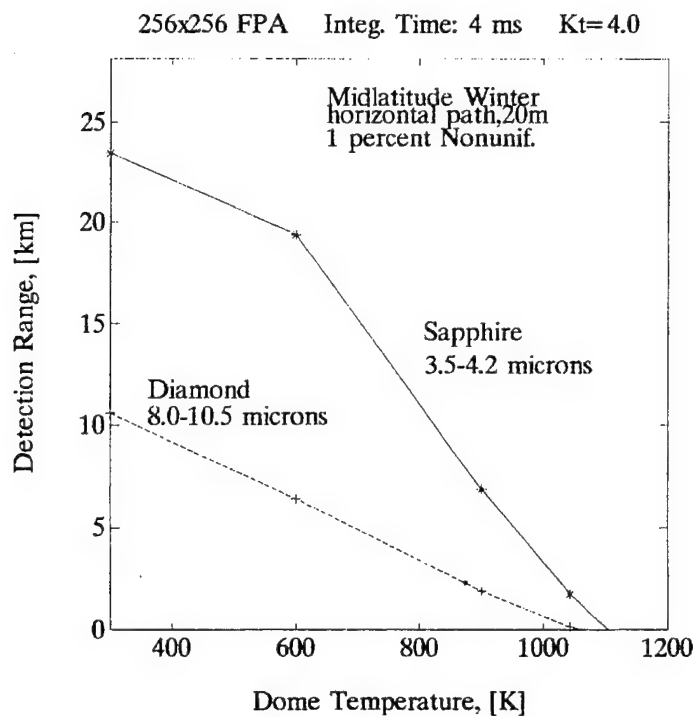


Figure 5-10

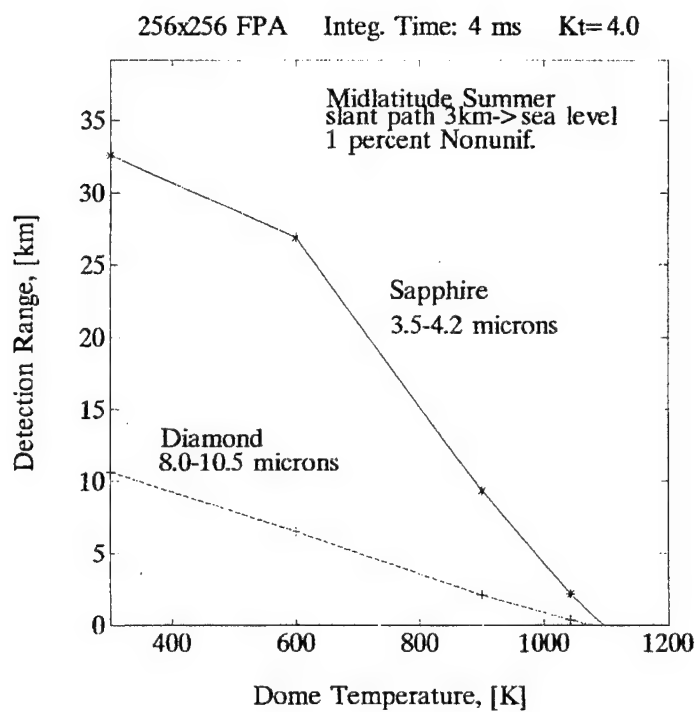


Figure 5-11

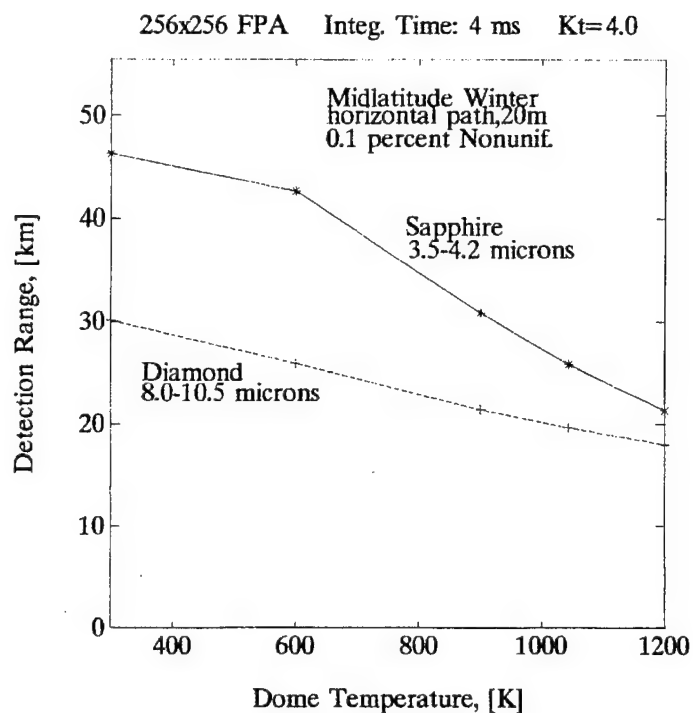


Figure 5-12

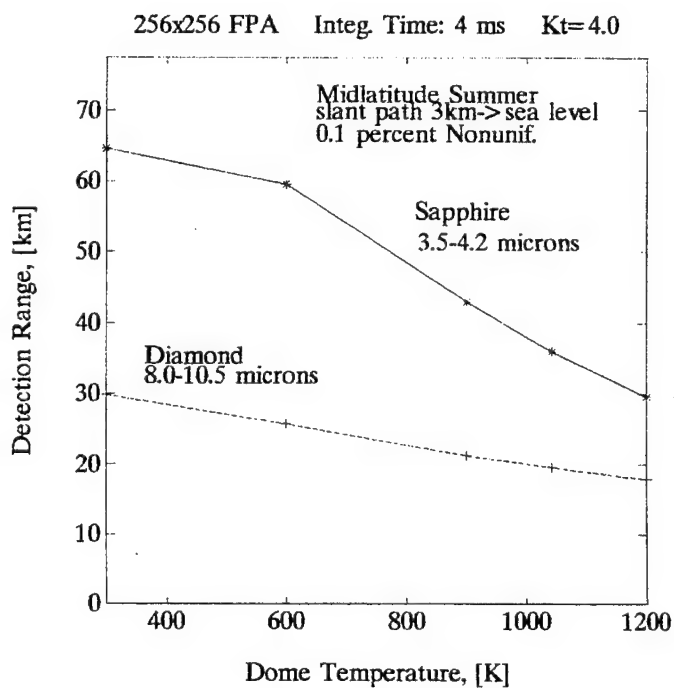


Figure 5-13

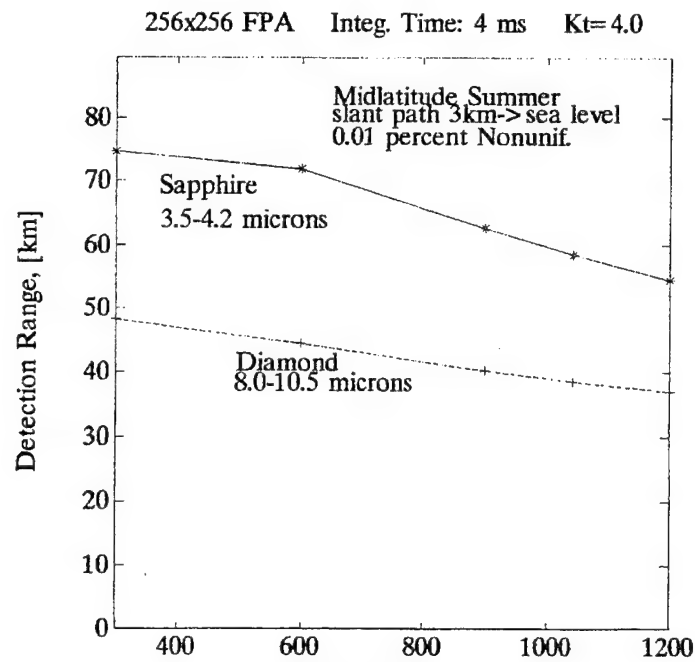


Figure 5-14

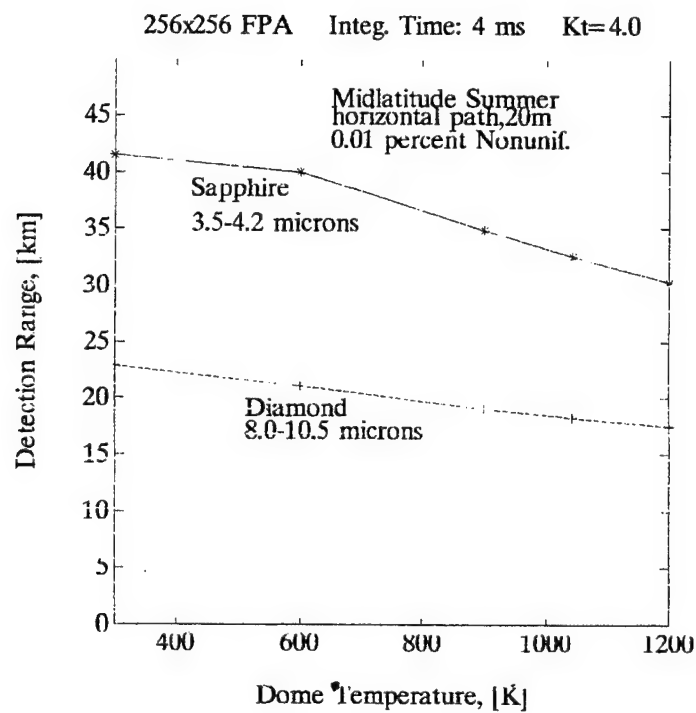


Figure 5-15

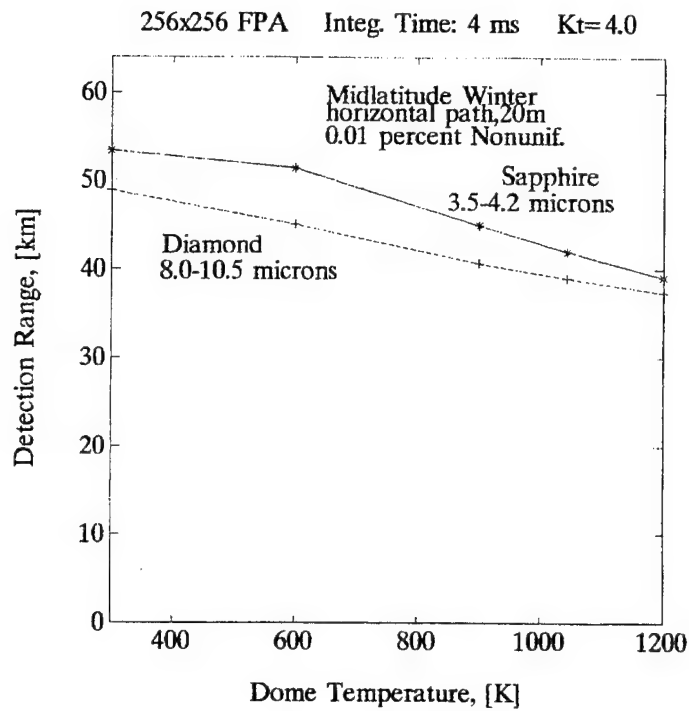


Figure 5-16

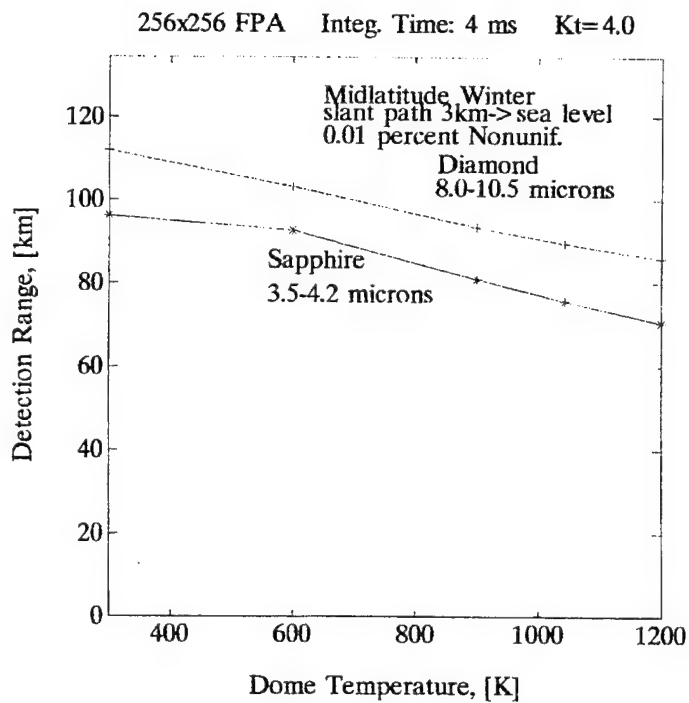


Figure 5-17

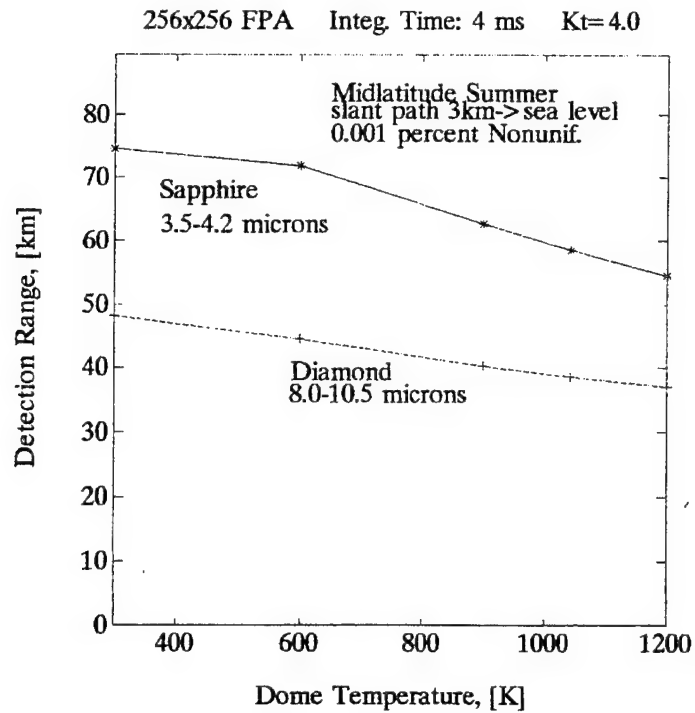


Figure 5-18

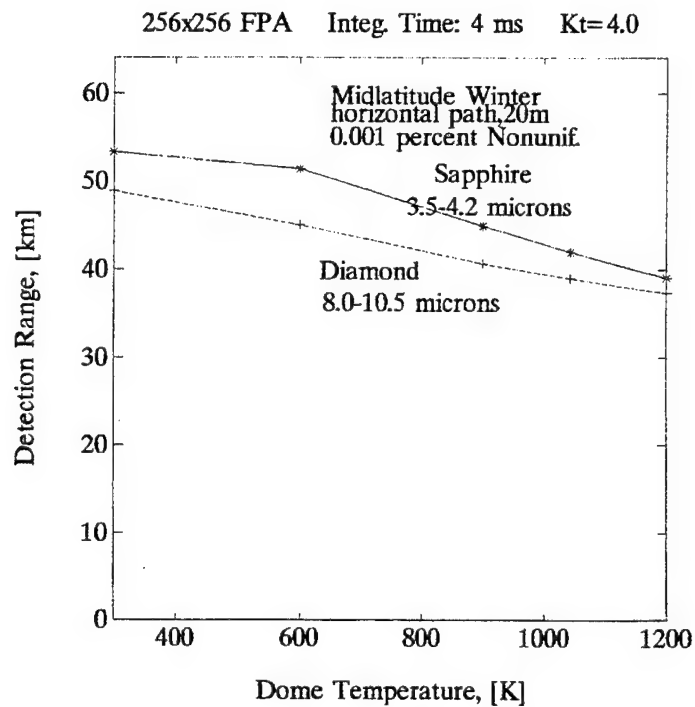


Figure 5-19

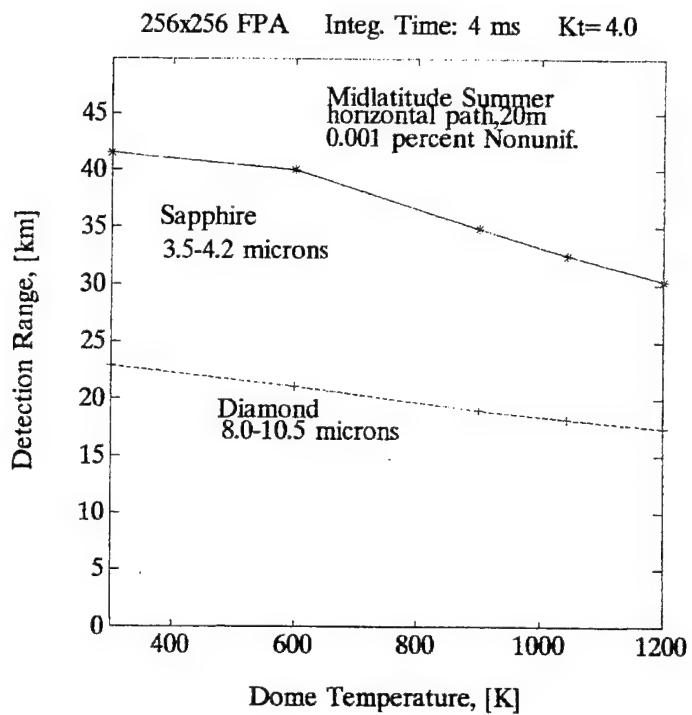


Figure 5-20

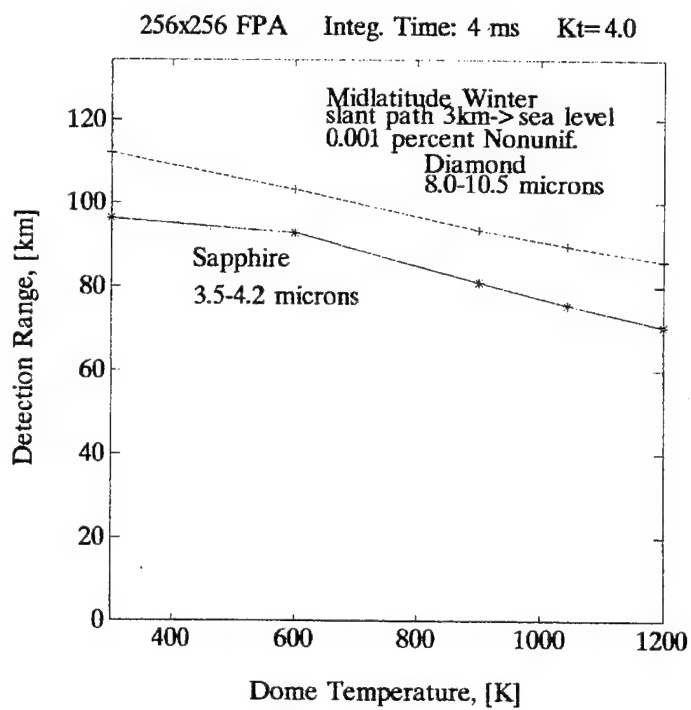


Figure 5-21

	Dome: Sapphire ($\epsilon=1 \times 10^{-3}$) Detector: InSb Spectral Band: 3.5-4.2 μm		Dome: Diamond ($\epsilon=5 \times 10^{-2}$) Detector: MCT Spectral Band: 8.0-10.5 μm	
Dome Temperature [K]	NEI [W/cm^2]	NETD [K]	NEI [W/cm^2]	NETD [K]
300	3.293×10^{-15}	2.236×10^{-2}	3.545×10^{-14}	1.026×10^{-2}
600	3.958×10^{-15}	2.689×10^{-2}	5.606×10^{-14}	1.623×10^{-2}
900	7.335×10^{-15}	4.982×10^{-2}	9.336×10^{-14}	2.702×10^{-2}
1043	9.705×10^{-15}	6.592×10^{-2}	1.140×10^{-13}	3.301×10^{-2}
1200	1.270×10^{-14}	8.628×10^{-2}	1.379×10^{-13}	3.993×10^{-2}

Table 5-2. Computed NEI and NETD for a 256x256 FPA with 0.01% Nonuniformity.

	Dome: Sapphire ($\epsilon=1 \times 10^{-2}$) Detector: InSb Spectral Band: 3.5-4.2 μm		Dome: Diamond ($\epsilon=5 \times 10^{-2}$) Detector: MCT Spectral Band: 8.0-10.5 μm	
Dome Temperature [K]	NEI [W/cm^2]	NETD [K]	NEI [W/cm^2]	NETD [K]
300	6.4471×10^{-15}	4.3790×10^{-2}	3.2358×10^{-13}	9.3677×10^{-2}
600	9.0596×10^{-14}	6.1534×10^{-2}	5.2919×10^{-13}	1.5320×10^{-1}
900	2.7617×10^{-14}	1.8758×10^{-1}	9.0180×10^{-13}	2.6107×10^{-1}
1043	4.4396×10^{-14}	3.0155×10^{-1}	1.1082×10^{-12}	3.2083×10^{-1}
1200	6.8278×10^{-14}	4.6375×10^{-1}	1.3473×10^{-12}	3.9003×10^{-1}

Table 5-3. Computed NEI and NETD for a 256x256 FPA with 0.1 % Nonuniformity.

	Dome: Sapphire ($\epsilon=1 \times 10^{-3}$) Detector: InSb Spectral Band: 3.5-4.2 μm		Dome: Diamond ($\epsilon=5 \times 10^{-2}$) Detector: MCT Spectral Band: 8.0-10.5 μm	
Dome Temperature [K]	NEI [W/cm ²]	NETD [K]	NEI [W/cm ²]	NETD [K]
300		3.789×10^{-1}		9.358×10^{-1}
600		5.570×10^{-1}		1.531
900		1.818		2.609
1043		2.9574		3.207
1200		4.5795		3.870

Table 5-4. Computed NETD for a 256x256 FPA with 1.00 % Nonuniformity.

	Dome: Sapphire ($\epsilon=1 \times 10^{-3}$) Detector: InSb Spectral Band: 3.5-4.2 μm		Dome: Diamond ($\epsilon=5 \times 10^{-2}$) Detector: MCT Spectral Band: 8.0-10.5 μm	
Dome Temperature [K]	NEI [W/cm ²]	NETD [K]	NEI [W/cm ²]	NETD [K]
300	3.2933×10^{-15}	2.2368×10^{-2}	3.5448×10^{-14}	1.0262×10^{-2}
600	3.958×10^{-15}	2.6886×10^{-2}	5.6063×10^{-14}	1.6230×10^{-2}
900	7.3345×10^{-15}	4.9817×10^{-2}	9.3362×10^{-14}	2.7028×10^{-2}
1043	9.7048×10^{-15}	6.517×10^{-2}	1.1401×10^{-13}	3.3007×10^{-2}
1200	1.2703×10^{-14}	8.6283×10^{-2}	1.3779×10^{-13}	3.9930×10^{-2}

Table 5-5. Computed NEI and NETD for a 256x256 FPA with 0.0001 % Nonuniformity.

	<i>Dome: Sapphire ($\epsilon=1 \times 10^{-3}$) Spectral Band: 3.5-4.2 μm</i>	<i>Dome: Diamond ($\epsilon=5 \times 10^{-2}$) Spectral Band: 8.0-10.5 μm</i>
<i>Dome Temperature [K]</i>	<i>Computed Photon Incidence [Photons/sec cm^2 sr]</i>	<i>Computed Photon Incidence [Photons/sec cm^2 sr]</i>
300	7.9172×10^{14}	1.1486×10^{17}
600	1.6141×10^{15}	1.8792×10^{17}
900	3.8033×10^{15}	3.2031×10^{17}
1043	6.1885×10^{15}	3.9366×10^{17}
1200	9.5829×10^{15}	4.7860×10^{17}

Table 5-6. Computed Photon Incidence in the focal plane.

VI. COMPUTATION OF PHOTON NOISE FROM HOT DOME

The characterization of fixed pattern-noise is an important aspect in evaluating the performance of a staring array. The hot IR dome will induce on the sensor a background photon noise distribution that can be considered like a fixed pattern-noise. In discussing the "hot dome problem" the question arises as to what dome temperature distribution should be used in the calculation of the dome emission effects on a staring sensor performance. Is it sufficient to consider the temperature of the dome to be uniform, and use a mean temperature, or will the background photon flux induced by dome emission impose a significant fixed pattern noise on the detector array? A useful simplification of the problem would be to consider the photon flux constant through the detector area and consider an averaged dome temperature.

In this chapter these questions will be investigated by computing the radiative interchange between the hot dome and the detector array.

A. RADIATION TRANSFER

Given the temperature distribution on the nose, we are able to compute the IR emission due to the aerokinetic heating of the window. In our case we want to compute the self-emission generated by the hot window that will fall on the seeker's IR sensor. As assumptions, we will consider that the window has reached thermal equilibrium, and so the temperature of the dome is the recovery temperature, that the window is thermally thin, and that the dome

inner surface is not coated with any material. In order to compute the window's self-emission sensed by the detector, an optical system must be assumed. In this case a small telescope, composed simply of a single germanium lens, is adopted. This optical design may seem unrealistic (no field lens or light pipe are used), but in fact, it can serve as a benchmark to compare some of the aero-thermal effects that degrade the system image quality due to dome emission.

To start the radiant transfer analysis, the radiant power reaching an element of area dA_d of the detector surface S_d due to the source element dA_w on window surface S_w should be computed first. For simplicity one should assume, for the moment, that no lens is present between the self-emitting window and the detector. The line joining the element areas, of length r_{dw} , makes angles of θ_w and θ_d with the respective normals to the surface elements, as shown in Fig. 6-1. The radiant power is d^2W_{dw} , a second order differential because both the source and receptor are elemental areas[11][21], so that

$$d^2W_{dw} = \frac{L dA_w dA_d \cos\theta_w \cos\theta_d}{r_{dw}^2} \quad (6-1)$$

where L is the radiance at dA_w .

The total radiant power at the entire second surface due to the entire first surface is, by integration.

$$W_{dw} = \int_{A_d} \int_{A_w} \frac{L \cos\theta_w \cos\theta_d dA_d dA_w}{r_{dw}^2} \quad (6-2)$$

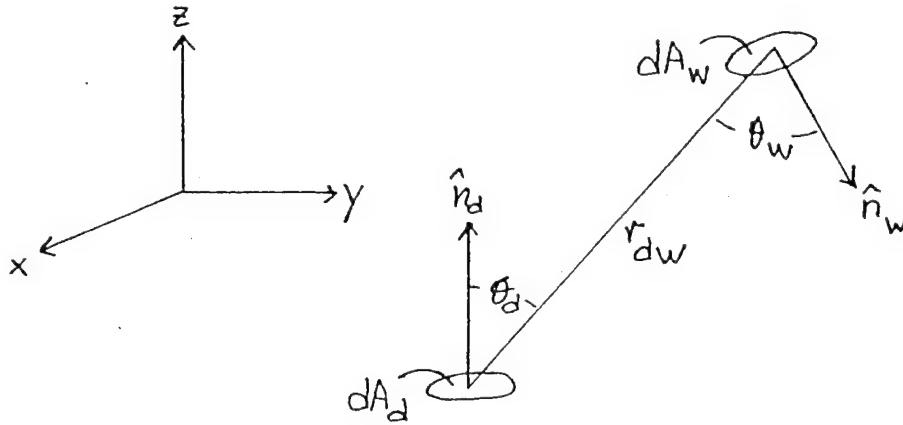


Figure 6-1. Configuration for interchange between two infinitesimal elements.

In adding power rather than amplitudes in this integration, we have tacitly assumed that the radiation source emits incoherent radiation and that the radiation emitted from any point of the surface is diffusely distributed, obeying Lambert's law. If we discretize the window and the detector in finite area elements, and consider each element to be isothermal, the total irradiance into the detector area element A_{dk} originated by the window is

$$W_k = \sum_{j=1}^J \frac{L_j \cos \theta_{wj} \cos \theta_{dkj} A_w A_{dk}}{r_{jk}^2} \quad (6-3)$$

where the window is discretized in J finite area elements and the detector in K finite area elements. The radiance in the spectral

region of interest of the window finite element j is

$$L_j(\lambda, T) \cdot \int_{\lambda_1}^{\lambda_2} \left(\frac{\varepsilon_j(\lambda, T)}{\pi} \right) \left(\frac{2\pi c}{\lambda^4} \right) \left(\frac{1}{e^{ch/\lambda k T_j - 1}} \right) d\lambda \quad (6-4)$$

where c is the speed of light in vacuum, h is Planck's constant and k is the Boltzmann's constant, and $\varepsilon(\lambda, T)$ the emissivity of the infinitesimal element.

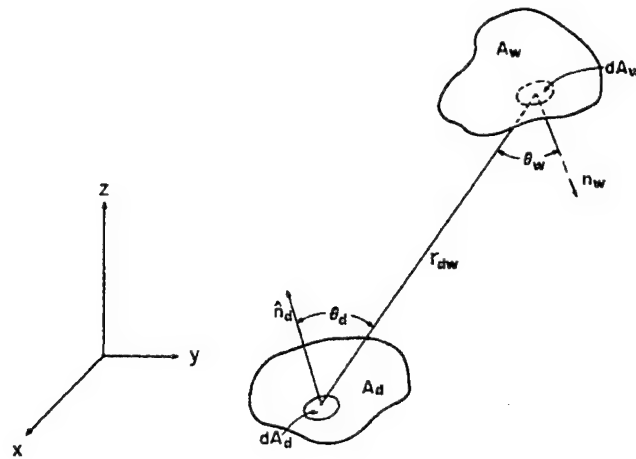


Figure 6-2. Configuration for interchange between two finite surfaces.

As was shown in the previous chapter, when the interest is in the limits imposed by dome heating on seeker performance, a more relevant quantity is the photon exitance Q (photons $s^{-1} cm^{-2}$) from the window. The spectral photon exitance, Q_λ (photons $s^{-1} cm^{-2} \mu m^{-1}$), is obtained by dividing Planck's law by hc/λ ,

$$Q_{\lambda}(T, \lambda) \cdot \left(\frac{2\pi c}{\lambda^4} \right) \left(\frac{1}{e^{hc/\lambda kT} - 1} \right) \cdot \quad (6-5)$$

The integrated photon exitance, in a given wavelength band, is then obtained by integrating Eq.(6-5) between the cut-on and cut-off wavelengths,

$$Q(T) \cdot \int_{\lambda_1}^{\lambda_2} Q_{\lambda} d\lambda \cdot \quad (6-6)$$

Numerical approximation of this integral over a narrow wavelength range yields

$$Q(T) \approx \frac{2\pi c}{\lambda_{mean}^4} \cdot \frac{1}{e^{hc/\lambda_{mean} kT} - 1} \cdot (\lambda_2 - \lambda_1) \quad (6-7)$$

where λ_{mean} is the average wavelength within the band λ_1 and λ_2 .

Then the photon flux that irradiates a finite area element k of the detector is

$$\Phi_k \cdot \sum_{j=1}^J \frac{\epsilon_j(\lambda, T) Q_j \cos \theta_{w_{jk}} \cos \theta_{d_{kj}} A_{w_j} A_{d_k}}{r_{jk}^2} \quad (6-8)$$

where Q_j is the black body exitance of the element j .

B. COMPUTATION METHOD

Now let's consider that between the window and the detector there exists a thick converging lens. This system is not in thermal equilibrium. In fact for simplification consider that the detector and lens are cooled to zero absolute. To compute the irradiance on the detector due to the thermal emission of the heated window, a ray tracing must be done. In this method, the paraxial system matrix is used to compute the image surface for the lens conjugate to the hot irdome (infrared dome) as object surface. This image surface is then treated as an equivalent input surface viewed directly from the detector plane. The conjugate surface is found by mapping several points of the window by means of a matrix transformation. This virtual surface is then divided into diffusely emitting finite elements. Radiative transfer calculations between each detector element and the finite elements of the image surface are carried out, taking into consideration the respective shape factors. The contributions of all finite elements are integrated, enabling the computation of the photon flux that irradiates each photo-sensitive detector element. This procedure is applied to all the elements of the detector array. An array fill factor of 1.0 is assumed.

1. System Ray-Transfer Matrix

If we consider the temperature field of the window to be axisymmetric, resulting from zero incidence of the missile, and the optical system to be looking in the missile longitudinal axis direction, the problem of computing the photon flux that falls into the detector becomes a 2-dimensional calculation with cylindrical symmetry. Considering the optical system consisting of a single

lens, a matrix can be constructed representing the action of the thick lens on the radiation emitted from the window, as follows:

$$M = \mathfrak{S}_3 \mathfrak{R}_2 \mathfrak{S}_2 \mathfrak{R}_1 \mathfrak{S}_1 \quad (6-9)$$

where M the composite transfer matrix is formed by: translation matrix, \mathfrak{S}_1 , representing the optical path from the input plane to the front face of the lens; refraction matrix, \mathfrak{R}_1 , representing the refraction process at the lens front surface; \mathfrak{S}_2 , translation matrix through the lens medium; \mathfrak{R}_2 , describing the refraction at the lens back surface; and finally \mathfrak{S}_3 , describing the final optical path from the lens back surface to the output plane, conjugate to the input plane.

The system matrix has the following format,

$$M = \begin{bmatrix} m_{11} & m_{12} \\ m_{21} & m_{22} \end{bmatrix} \quad (6-10)$$

If the output plane corresponds to the conjugate to the input plane, the matrix element m_{12} must be identically zero [21]. Then m_{11} is the transverse linear magnification.

2. Calculation of the System Ray-Transfer Matrix

In this section the system matrix will be calculated by multiplying consecutively the several translation and refraction component matrices for paraxial rays.

$$\mathfrak{S}_1 = \begin{bmatrix} 1 & x_o \\ 0 & 1 \end{bmatrix} \quad (6-11a)$$

$$\mathfrak{R}_1 = \begin{bmatrix} 1 & 0 \\ \frac{1}{R_1} \left(\frac{n}{n_1} - 1 \right) & \frac{n}{n_1} \end{bmatrix} \quad (6-11b)$$

$$\mathfrak{S}_2 = \begin{bmatrix} 1 & t \\ 0 & 1 \end{bmatrix} \quad (6-11c)$$

$$\mathfrak{R}_2 = \begin{bmatrix} 1 & 0 \\ \frac{1}{R_2} \left(\frac{n_1}{n} - 1 \right) & \frac{n_1}{n} \end{bmatrix} \quad (6-11d)$$

$$\mathfrak{S}_3 = \begin{bmatrix} 1 & x \\ 0 & 1 \end{bmatrix} \quad (6-11e)$$

where x_o is the distance from the input surface to the lens, R_1 and R_2 are the radii of curvature of the front and back surfaces of the lens, n and n_1 the indexes of refraction of the air and of the lens respectively, t represents the lens thickness, and finally, x is the distance from lens to the output plane. Carrying out the matrix multiplication as in Eq.(6-9) yields the following matrix elements m_{11} and m_{12} of the system matrix M :

$$m_{12} = x_o \cdot \frac{tx_o}{R} \left(\frac{n}{n_1} - 1 \right) \cdot \frac{nt}{n_1} \cdot x \left[\frac{1}{R_2} \left(\frac{n_1}{n} - 1 \right) \left(x_o \cdot \frac{tx_o}{R_1} \left(\frac{n}{n_1} - 1 \right) \cdot \frac{nt}{n_1} \right) \cdot \frac{n_1}{n} \left(\frac{x_o}{R_1} \left(\frac{n}{n_1} - 1 \right) \cdot \frac{n}{n_1} \right) \right] \quad (6-12a)$$

$$m_{11} = 1 \cdot \frac{t}{R_1} \left(\frac{n}{n_1} - 1 \right) \cdot \frac{x}{R_1} \left(\frac{n}{n_1} - 1 \right) \left[1 \cdot \frac{t}{R_1} \left(\frac{n}{n_1} - 1 \right) \cdot \frac{n_1}{n} \right] \quad (6-12b)$$

When $m_{12} = 0$, the output plane is the image plane conjugate to the input plane. Using Eq.(6-12a) the location x of the output plane can be then computed:

$$x = \frac{x_o \cdot \frac{tx_o}{R} \left(\frac{n}{n_1} - 1 \right) \cdot \frac{nt}{n_1}}{\frac{1}{R_2} \left(\frac{n_1}{n} - 1 \right) \left(x_o \cdot \frac{tx_o}{R_1} \left(\frac{n}{n_1} - 1 \right) \cdot \frac{nt}{n_1} \right) \cdot \frac{n_1}{n} \left(\frac{x_o}{R_1} \left(\frac{n}{n_1} - 1 \right) \cdot \frac{n}{n_1} \right)} \quad (6-13)$$

Substituting this value of x in Eq.(6-12b) gives the value of linear magnification at that position.

In order to determine the system limiting aperture (footprint at the dome) the other elements should be calculated as well, leading to the following values:

$$m_{21} = \frac{1}{R_2} \left(\frac{n_1}{n} - 1 \right) \left(1 \cdot \frac{t}{R_1} \left(\frac{n}{n_1} - 1 \right) \right) \cdot \frac{n_1}{n} \left(\frac{1}{R_1} \left(\frac{n}{n_1} - 1 \right) \right) \quad (6-14a)$$

$$m_{22} = \frac{1}{R_2} \left(\frac{n_L}{n} - 1 \right) \left(x_o \cdot \frac{tx_o}{R_1} \left(\frac{n}{n_L} - 1 \right) \cdot \frac{nt}{n_L} \right) \cdot \frac{n_L}{n} \left(\frac{x_o}{R_1} \left(\frac{n}{n_L} - 1 \right) \cdot \frac{n}{n_L} \right) \quad (6-14b)$$

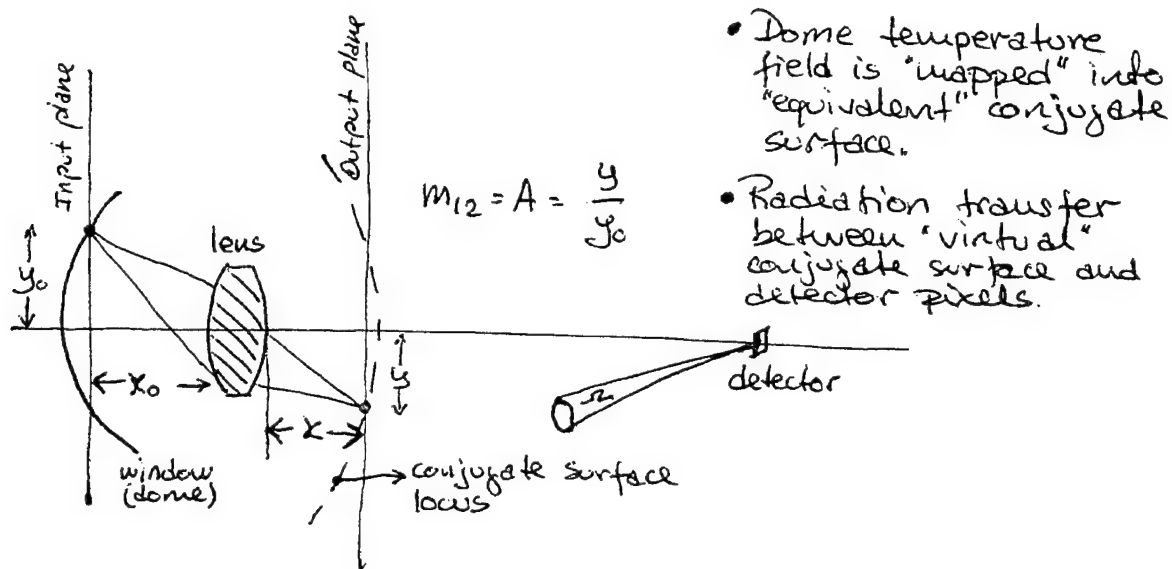


Figure 6-3. Notation and surface definition.

3. Computation of the Footprint at the Dome

The computation of the footprint at the dome of the system is necessary in order to determine which portion of the dome will irradiate the detector, and so contribute to the background noise. This can be done by tracing back the limiting optical rays from the detector that pass through the lens aperture. Again considering the same system geometry, the problem becomes 2-dimensional. We have

$$\begin{bmatrix} y \\ \sin \alpha \end{bmatrix} \cdot M' \begin{bmatrix} y_0 \\ \sin \alpha_0 \end{bmatrix}, \quad (6-15)$$

where α_0 is the angle subtended by the ray from the detector passing through the lens margin, as shown in Fig. 6-4, and the composite matrix M' defined as follows:

$$M' = \mathcal{R}'_2 \mathcal{S}'_2 \mathcal{R}'_1 \mathcal{S}'_1 \quad (6-16)$$

where $\mathcal{R}'_1 = \mathcal{R}_1$, $\mathcal{S}'_2 = \mathcal{S}_2$, $\mathcal{R}'_2 = \mathcal{R}_2$, and the translation matrix

from the detector into the lens back surface is defined as follows:

$$\mathfrak{S}'_1 = \begin{bmatrix} 1 & t_3 \\ 0 & 1 \end{bmatrix}, \quad (6-17)$$

The matrix multiplication as written in Eq.(6-14) leads to the following matrix M' elements

$$m'_{11} = 1 + \frac{t}{R_2} \left(\frac{n}{n_L} - 1 \right) \quad (6-18a)$$

$$m'_{12} = t_3 + \frac{tx_o}{R_2} \left(\frac{n}{n_L} - 1 \right) + \frac{nt}{n_L} \quad (6-18b)$$

$$m'_{23} = \frac{1}{R_2} \left(\frac{n_L}{n} - 1 \right) \left(1 + \frac{t}{R_2} \left(\frac{n}{n_L} - 1 \right) \right) + \frac{n_L}{n} \left(\frac{1}{R_2} \left(\frac{n}{n_L} - 1 \right) \right) \quad (6-18c)$$

$$m'_{24} = \frac{1}{R_1} \left(\frac{n_L}{n} - 1 \right) \left(t_3 + \frac{tx_o}{R_2} \left(\frac{n}{n_L} - 1 \right) + \frac{nt}{n_L} \right) + \frac{n_L}{n} \left(\frac{tx_o}{R_2} \left(\frac{n}{n_L} - 1 \right) + \frac{nt}{n_L} \right) \quad (6-18d)$$

Substituting the following values into the respective expressions,

$$n = 1.000$$

$$t = 0.300 \text{ cm}$$

$$n_L(10\mu\text{m}) = 4.003174$$

$$t_3 = 9.09099 \text{ cm}$$

$$R_1 = -50.000 \text{ cm}$$

$$R_{ap} = 1.500 \text{ cm}$$

$$R_2 = 60.000 \text{ cm}$$

yields the following matrix:

$$M' = \begin{bmatrix} 0.996249 & 9.131830 \\ -5.683183e-2 & -1.483700 \end{bmatrix}, \quad (6-19)$$

with α_0 given by

$$\alpha_0 = \tan^{-1} \left(\frac{R_{ap}}{t_3} \right) \quad (6-20)$$

Using Eq.(6-13),

$$\begin{bmatrix} y \\ \sin\alpha \end{bmatrix} = \begin{bmatrix} 0.996249 & 9.131830 \\ -5.683183e-2 & -1.483700 \end{bmatrix} \begin{bmatrix} 0 \\ \sin(9.37^\circ) \end{bmatrix}, \quad (6-21)$$

yields

$$\begin{bmatrix} y \\ \sin\alpha \end{bmatrix} = \begin{bmatrix} 1.487 \\ -.2416 \end{bmatrix}, \quad (6-22)$$

which implies that $\alpha = 13.98^\circ$ Furthermore, it follows that

$$(z-r_w)^2 + r^2 = r_w^2 \quad (6-23)$$

where $r_w = 3.3166$ cm (dome radius of curvature). This defines a circular pupil on the dome of radius $r = 1.9$ cm ($z=0.595$ cm), computed by the following approximate formula:

$$r = \tan\alpha(t_1 - z) + R_{ap}. \quad (6-24)$$

The quantities α , t_1 , z and R_{ap} are defined in Fig. 6-4.

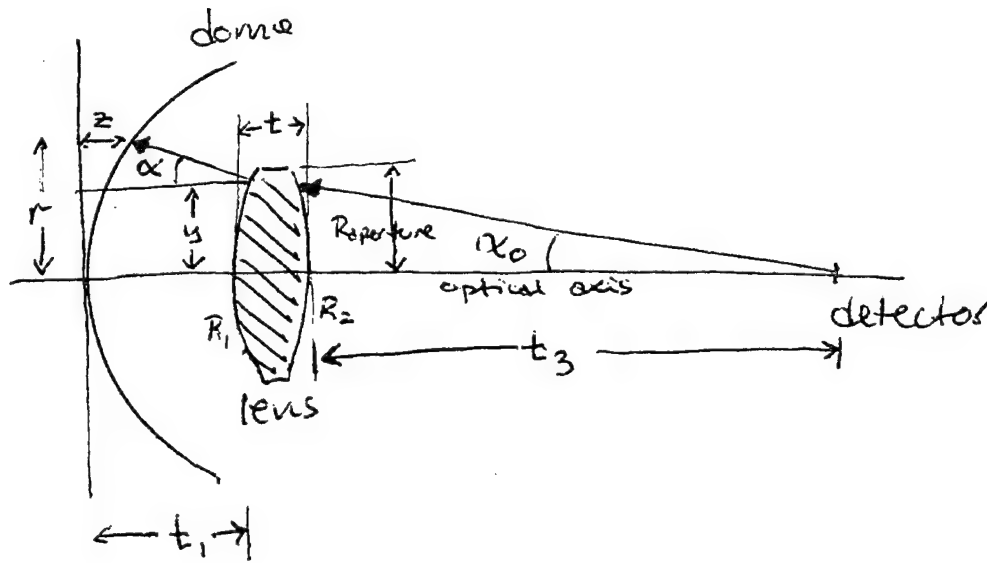


Figure 6-4. Ray tracing variable nomenclature.

C. RESULTS AND DISCUSSION

The characterization of fixed pattern noise is an important aspect in evaluating the performance of a staring array. Fixed pattern noise is a generic term used to describe the variations in gain and offset levels observed over the FPA detector elements.

The motivation of our study is the characterization of fixed pattern noise induced by dome emission.

Computations were performed for the case of a hemispherical dome corresponding to the case I nose configuration (see page 49) of a missile at Mach 4 at sea level with zero incidence angle. Two

different computations were performed, the first considering that the dome temperature field was that obtained by solving the thin-layer Navier-Stokes equations and considering an adiabatic wall as one of the boundary conditions; in the other case the dome temperature was considered to be the mean value of the first case.

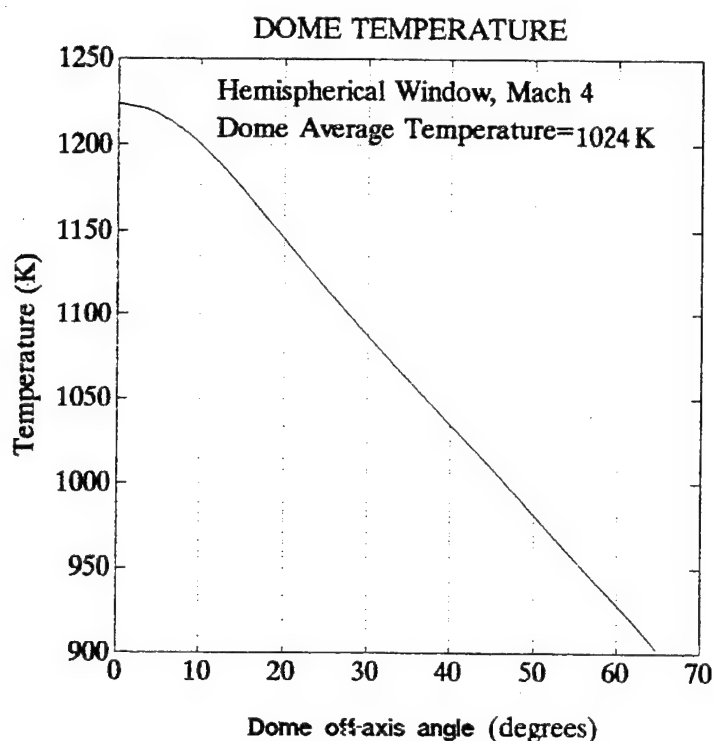


Figure 6-5. Thin-Layer-Navier-Stokes computed dome temperature.

The optical system was considered to be looking straight ahead and just the portion of the window corresponding to the system's window pupil was considered. The collecting lens was designed using the ZEMAX XE ray tracing program. The lens data are given in Appendix E. The dome material chosen was CVD Diamond. The waveband considered was from 8.0-10.5 μ m. Fig. 6-5 shows the dome temperature

versus off-axis angle. For the case considered the temperature field has cylindrical symmetry. Fig. 6-6 shows the photon irradiance on a 64x64 FPA(Focal Plane Array) due to this temperature distribution. Fig. 6-7 shows the photon irradiance on a 64x64 FPA based on the mean dome temperature of the same temperature distribution. The mean dome temperature considered is 1024 K.

For the computations cell separation of 30 μ m and a fill factor of 1.0 are considered. A fill factor of 1.0 although unrealistic serve the purpose of showing the variation of the photons flux through the array.

The usual means of characterizing fixed-pattern noise is by specifying the variance, σ , of the pixel levels,

$$\sigma^2 = \frac{\sum_i \sum_j [I(x_i, y_j) - M]^2}{\text{number of pixels}} \quad (6-25)$$

The variance computation is often written(schematically) as:

$$\sigma^2 = \overline{(I - M)^2} = \overline{I^2} - M^2, \quad (6-26)$$

the array data being denoted by $I(x,y)$ and the mean by M . A relatively larger variance is seen for arrays exhibiting an appreciable amount of fixed-pattern noise. However, a specification of variance alone gives no indication as to how the non-uniformities are distributed over the array, essentially assuming that there is an equal contribution from the fixed-pattern noise at all spatial frequencies.

Figure 6-6 shows the percentage variation of the quantum irradiance on a 64x64 focal plane array due to a dome with a non-

uniform temperature field distribution. The values were computed in relation to the maximum quantum irradiance at the center of the array. The maximum quantum irradiance is 9.924×10^{12} photons/sec per pixel at the center of the array. The minimum quantum irradiance is 9.839×10^{12} photons/sec per pixel at the corners of the array. The computed mean quantum irradiance is 6.2829 photons/sec per pixel. For this case the maximum computed irradiance variation is -0.8% at the corners of the array.

Figure 6-7 shows the percentage variation of the quantum irradiance on the focal plane array due to a dome with a uniform temperature field distribution. The values were computed in relation to the maximum quantum irradiance at the center of the array. The minimum quantum irradiance is $\times 10^{12}$ photons/sec per pixel at the corners of the array. The computed mean quantum irradiance is 6.2829 photons/sec per pixel. For this case the maximum computed irradiance variation is -0.8% at the corners of the array.

This is five times more than the variance found for a uniform temperature dome at the average computed temperature. (Fig.6-7). The computed variance is 1.26×10^{13} photons² per pixel for the case of a dome with uniform temperature.

Fig. 6-8 shows a detectivity contour plot for the case of uniform dome temperature. For that purpose the following equation [29] was used,

$$D_{BLIP}(\lambda, f) = \frac{\lambda_{mean}}{hc} \sqrt{\frac{\eta}{2Q_p^B}} \quad (6-27)$$

where Q_p^B is the background photon flux per pixel element area. The

quantum efficiency, η , is 0.7.

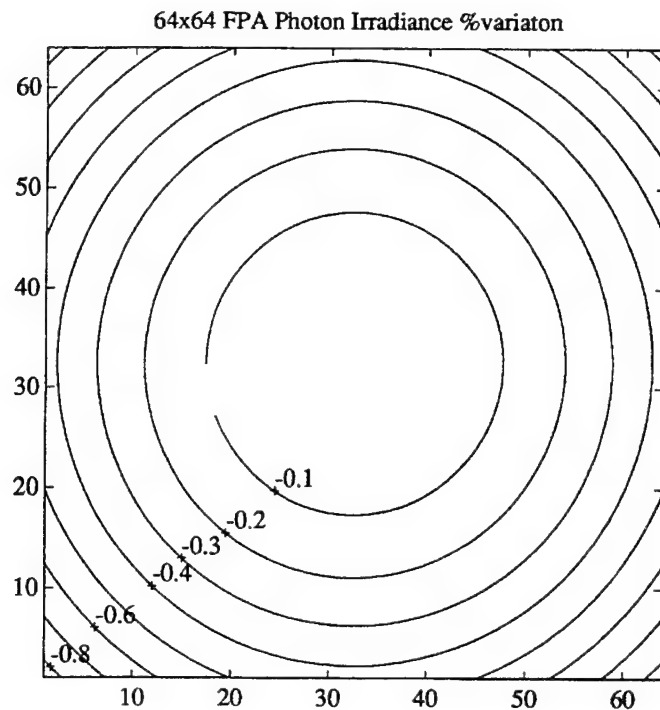


Figure 6-6.. Photon irradiance percentual variation for a 64x64 FPA considering a non-uniform dome temperature.

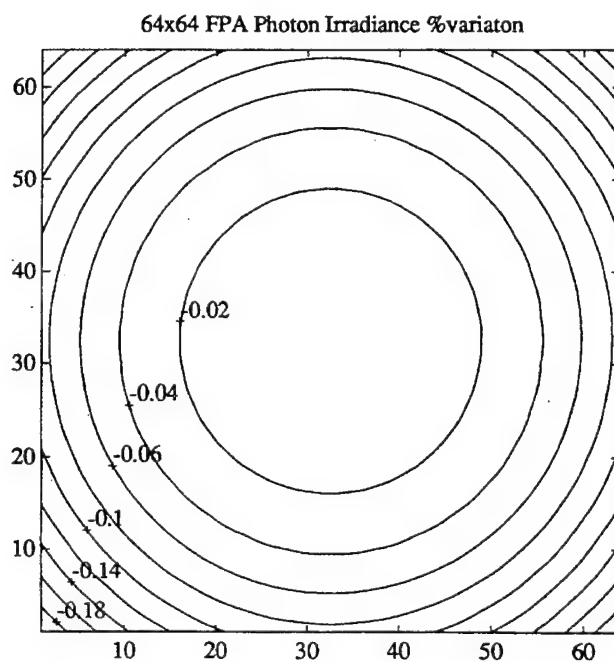


Figure 6-7. Photon irradiance percentual variation on a 64x64 FPA considering a uniform dome temperature.

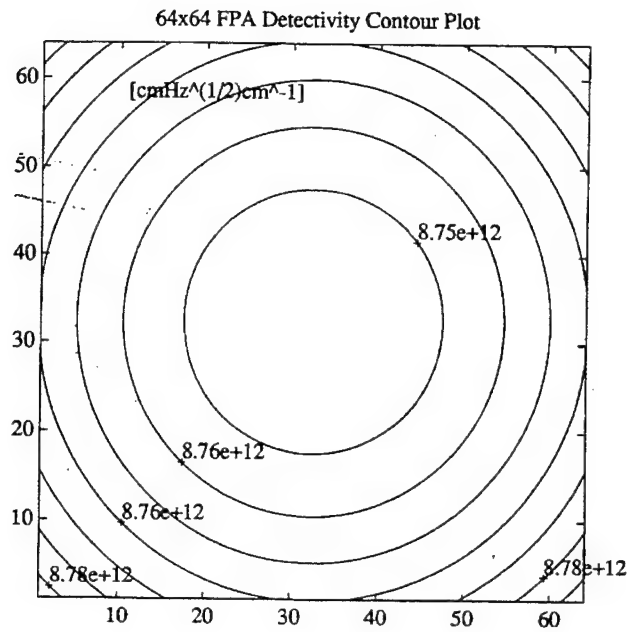


Figure 6-8. Detectivity contour on a 64x64 FPA induced by the fixed pattern of the dome background irradiance (non-uniform dome temperature)

VII. CONCLUSIONS

As expected, flight at high supersonic speeds has a dramatic effect on target detection range degradation of IR guided missiles due to the aerokinetic heating of its IR window dome. The temperature increase of IR dome increases the background quantum flux density that irradiates the IR sensor leading to an decrease of the signal-to-noise ratio and the correspondent decrease of the NETD of the detection system. An equation was derived that shows this effect. For Mach number speeds of 2 and 4 the detection range degradation for the cases considered reached values around 37% and 97% respectively for array non-uniformity of 1%. This means that at high supersonic Mach numbers the seeker IIR ("Imaging Infra-Red") system becomes "blind" due to dome emission. For lower array non-uniformities, i.e. 0.001 percent the detection range degradation was smaller in the range 12% and 22% for Mach 2 and 4 respectively.

Since the integration times of the array are much smaller than the missile guidance system time constant (over 100 times) the photon irradiance due to dome emission on the FPA originates a fixed pattern noise on the detector responsible for a detectivity non-uniformity of the array pixels. As shown in Chapter 5, the IR seeker detection range has a strong dependance of the detection array non-uniformity.

APPENDIX A. CALCULATION OF DOME THICKNESS

Any viable missile dome structure must be able to withstand the mechanical stresses induced by aerodynamic pressure as well as thermal stresses induced by aerodynamic heating. In a thermally thin regime, the TSR (Temperature Shock Resistance) performance will be maximized by making the dome as thin as possible. The *TSR* indicates the range of Mach number variation that an IR dome can withstand without a good chance of catastrophic failure[10]. This temperature corresponds to the maximum difference in temperature between the stagnation temperature and the temperature of the inner wall of the dome that the dome can withstand. This leads to an "optimum" dome thickness equal to the minimum dome thickness (L_{min}) required to withstand the aerodynamic loads. Since the emittance of the dome increases with its thickness the minimum dome thickness will minimize dome self-emission effects as well. An accurate prediction of the dome emission effects necessitates an accurate computation of the dome temperature and of its emittance, and by consequence of the dome thickness.

1. Pressure Induced Stress

In a supersonic flight environment, altitude and velocity determine the pressure load. We should follow the procedure outlined in section II.C in order to calculate the minimum dome thickness to withstand the aerodynamic load,

$$\Delta p = p_{st} - p_{\infty} = p_{\infty} \left[\frac{p_{st}}{p_{\infty}} - 1 \right] \quad (A-1)$$

where

$$\frac{P_{st}}{P_{\infty}} = \left[\left(\frac{\gamma + 1}{2} \right) M_{\infty}^2 \right]^{\frac{\gamma}{\gamma + 1}} \left[\left(\frac{2\gamma}{\gamma + 1} \right) M_{\infty}^2 - \frac{\gamma - 1}{\gamma + 1} \right]^{\frac{1}{\gamma + 1}} \quad (A-2)$$

Consider a medium altitude flight profile. From *U.S. Standard Atmosphere* Tables one has for an altitude of 3 km:

$$\gamma = 1.4$$

$$P_{\infty} = 10.2 \text{ psi.}$$

Evaluating Eq.(A-2) gives a pressure jump along the stagnation streamline of 21.07. Substituting values in Eq.(A-1), gives $\Delta p = 204.7 \text{ psi.}$

Let us consider that a "floating attachment" scheme, like a polyamide adhesive, is used to decouple the dome from the missile body. The maximum tensile stresses failure criterion leads to the following expression

$$\frac{\sigma_f / SF}{\Delta p} = 0.581 \left(\frac{L_{min}}{R} \right)^{3/2} \quad (A-3)$$

for the minimum dome thickness, L_{min} , where σ_f refers to the nominal flexure strength of the material, and SF is an appropriate safety factor that yields the minimum thickness required to prevent catastrophic failure of the dome. Since currently available IR transmitting dome materials are brittle ceramics, they may exhibit a wide range of fracture probabilities under apparently identical loadings, which suggest safety factors of at least four (4) if σ_f is the characteristic flexural strength derived from a Weibull statistical analysis. The dome thickness required for withstanding

aerodynamic loads Δp with good probability of survival can be obtained from the following equation:

$$\frac{L_{min}}{R} = 1.75 \left(\frac{\Delta p}{\sigma_f} \right)^{2/3} \quad (A-4)$$

For a truncated hemispherical dome with $R = 3.3166$ cm, and using CVD diamond as dome material,

$$L_{min} = 1.75 (3.32 \times 10^{-2} m) \left(\frac{1.41 \times 10^6 Pa}{1.5 \times 10^9 Pa} \right)^{2/3} = 5.4 \times 10^{-5} m \quad (A-5)$$

2. Thermally Induced Stress

As shown in Chapter 1 the maximum tensile stress should be given by an expression such as [10]

$$\sigma_{max} = \frac{1}{TSF} \alpha E' \Delta T, \quad (A-6)$$

where α = thermal expansion coefficient,
 TSF = Thermal Stress Factor,
 E' = biaxial elastic modulus,
 ΔT = temperature differential across the dome wall.

The stress induced by the sudden aerodynamic heating of the dome depends on the ability of the dome to conduct the heat flow and ultimately upon the heat-flow pattern, which is controlled by the Biot number.

$$Bi = \frac{hL}{k}, \quad (A-7)$$

where h = heat transfer coefficient at the outer surface,
 L = dome thickness,
 k = thermal conductivity of dome material.

The "optimum" dome thickness, $L = L_{\min}$ is determined by aerostructural requirements and should be as thin as possible to enhance the thermal shock resistance and reduce self-emission. In assessing the "ultimate" TSR of an IR dome, the Biot number should be expressed in the following way

where h'_{st} refers to a 1-cm radius dome.

At Mach=4, altitude=3km

$$Bi = \frac{0.908\sqrt{R}}{k\sigma_f^{2/3}} \quad (A-8)$$

From Fig A-1,

$$Bi = \frac{(0.908)(3.3166\text{cm})^{1/2}}{(20\text{Wcm}^{-1}\text{K}^{-1})(150)^{2/3}} \approx 1 \times 10^{-4} \quad (A-9)$$

where R is in centimeters, k in watts per centimeter per kelvin, and σ_f is in megapascals. Considering the hemispherical dome window case, $R = 3.3166$ cm and CVD Diamond as window material, we conclude that the response of the diamond to transient heating will be in the thermally thin mode ($Bi < 1$). Indeed this material exhibits extremely low Biot numbers ($Bi < 0.001$) that minimize the temperature gradients

across the thickness.

The thermal shock temperature (TST) of the minimum thick temperature missile domes with Bi^* that represents the Biot number for the most severe environment based on projected tactical requirements.

For thermally thin domes the peak temperature differential between the outer and inner wall is given by

$$(\Delta T)_p = (T_{st} - T_{iw}) \times Bi, \quad Bi < 1. \quad (A-10)$$

In the thermally thin regime the temperature of the back face may get hot long before the front reaches the recovery temperature.

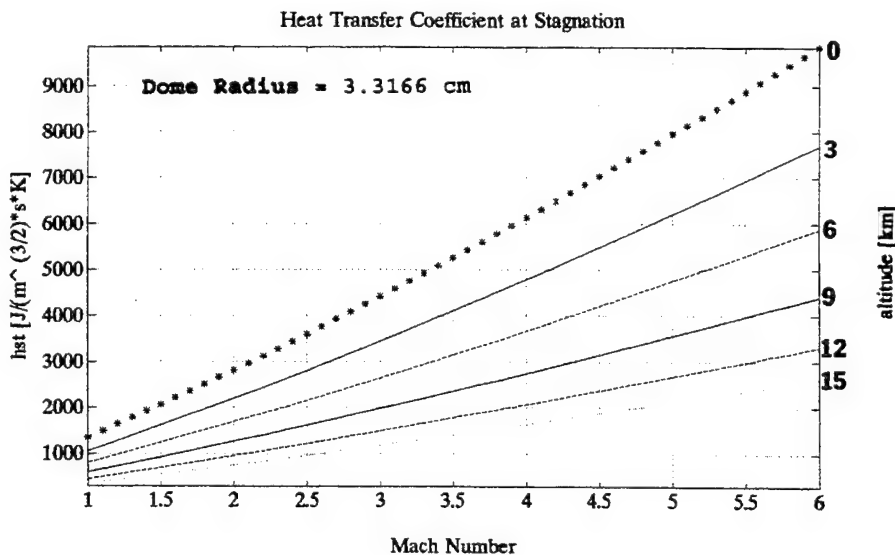


Figure A-1. Heat transfer Coefficient at Stagnation.

APPENDIX B. PROGRAM TO EXTRACT FLOW VARIABLES

The following program written in FORTRAN was used to extract from the *q.save* file (PLOT3D format) the values of the flow variables of Table 4-2. It uses the *grid.in* file (PLOT3D format) and the *q.save* file as input files. By a simple alteration of the source code it is possible to read from the *q.save* computed file flow field values for a specific range of I(streamwise direction), J(circumferencial direction) and K(radial direction).

```

C   Extract x,y,z vs. Temperature, Normalized Temperature,
C   Coefficient of Pressure from grid and Q files in PLOT3D format,
C
C   XYPLOT and MATLAB formats.
C
      PARAMETER (MI=300,MJ=100,MK=50)
      DIMENSION XYZ(MI,MJ,MK,3),Q(MI,MJ,MK,5)
      DIMENSION X(MI),Y(MI),Z(MI),T(MI)
      CHARACTER*80 FILE
C
      PARAMETER (GAMMA=1.4)
C
C
C   Read grid file.
C
      WRITE(*,1)
1  FORMAT(' Enter PLOT3D grid filename: ', $)
      READ(*,2) FILE
2  FORMAT(A)
      OPEN(UNIT=1,FILE=FILE,STATUS='OLD',FORM='FORMATTED')
      READ(1,*) NI,NJ,NK
      IF (NI.GT.MI .OR. NJ.GT.MJ .OR. NK.GT.MK) THEN
        WRITE(*,3)
3     FORMAT(' Grid is too big, exceeds internal dimensions.')
        GOTO 100
      ENDIF
      READ(1,*) (((XYZ(I,J,K,NX),I=1,NI),J=1,NJ),K=1,NK),NX=1,3)
      CLOSE(UNIT=1)
C
C   Read Q file.
C
      WRITE(*,4)
4  FORMAT(' Enter PLOT3D      Q filename: ', $)
      READ(*,2) FILE
      OPEN(UNIT=1,FILE=FILE,STATUS='OLD',FORM='FORMATTED')
      READ(1,*) NID,NJD,NKD
      IF (NID.NE.NI .OR. NJD.NE.NJ .OR. NKD.NE.NK) THEN
        WRITE(*,5)
5     FORMAT(' Q file dimensions don''t match grid.')
        GOTO 100
      ENDIF
      READ(1,*) FSMACH,ALPHA,RE,TIME
      READ(1,*) (((Q(I,J,K,NX),I=1,NI),J=1,NJ),K=1,NK),NX=1,5)
      CLOSE(UNIT=1)
C
C   Get range of (i,j,k).
C
      WRITE(*,11)
11  FORMAT(' Enter  IS,IE, JS,JE, KS,KE: ', $)
      READ(*,*) IS,IE,JS,JE,KS,KE
C

```

```

WRITE(*,12)
12 FORMAT(' Enter XYPLOT Wall Temp filename: ', $)
READ(*,2) FILE
OPEN(UNIT=1,FILE=FILE,STATUS='UNKNOWN',FORM='FORMATTED')
C
GM1    = GAMMA-1.
RHOINF = 1.
CINF   = 1.
PINF   = 1./GAMMA
V2INF  = 0.5*(FSMACH/CINF)**2
QINF   = RHOINF*V2INF
C
DO 20 K = KS,KE
C
DO 20 J = JS,JE
I = 1
J = 1
C
DO 20 K = 1,35
RHO    = Q(I,J,K,1)
U      = Q(I,J,K,2)/RHO
V      = Q(I,J,K,3)/RHO
W      = Q(I,J,K,4)/RHO
E0     = Q(I,J,K,5)/RHO
V2     = 0.5*(U**2 + V**2 + W**2)
EI     = E0 - V2
P      = GM1*RHO*EI
CP     = (P - PINF)/QINF
T(I)   = (P/PINF)/(RHO/RHOINF)*520*5/9.
Tratio = (P/PINF)/(RHO/RHOINF)
X(I)   = XYZ(I,J,K,1)
Y(I)   = XYZ(I,J,K,2)
Z(I)   = XYZ(I,J,K,3)
WRITE(1,*) X(I),Y(I),Z(I),T(I),Tratio,Cp
20    CONTINUE
CLOSE(UNIT=1)
C
C
100 CONTINUE
STOP
END

```


APPENDIX C. OVERFLOW INPUT/OUTPUT FILE SPECIFICATIONS

The following list describes the input/output files and the data they contain:

<i>Filename</i>	<i>Unit</i>	<i>I/O</i>	<i>Description</i>
grid.in	1	input	grid file (PLOT3D format)
fort.2	2	output	input from PEGASUS
q.restart	3	input	Q restart file (PLOT3D format)
q.save	4	input	Q save file (PLOT3D format)
q.bomb	4	input	Q bomb file (PLOT3D format)
resid.out	7	output	flow solver residual history
fomo.out	8	output	force and moment coefficient history
rpmin.out	9	output	minimum density/pressure/gamma history
turb.out	11	output	turbulence model residual history
species.out	12	output	species continuity residual history
interp.n	10	both	PEGASUS interpolation and boundary point indices
param.n	10	both	intermediate storage of run parameters
flowvar.n	10	both	intermediate storage of flow variables
gridmet.n	10	both	intermediate storage of grid and metrics

Table C-1. OVERFLOW Input/Output files.

APPENDIX D. LOWTRAN ATMOSPHERIC PROPAGATION MODEL

The *Atmospheric Transmittance/Radiance Computer Code* LOWTRAN 6 calculates both the atmospheric transmittance and radiance throughout the infrared spectrum (0.25 to 28.5 μm) [28]. It uses a single parameter band model for molecular absorption, and includes the effects of continuum absorption, molecular scattering, and aerosol absorption. Refraction and earth curvature are included in the calculation for slant paths [28].

Five seasonal models and the 1962 U.S. Standard Atmosphere are provided as inputs to the LOWTRAN program using typical altitude, pressure, temperature, water vapor density and ozone density profiles for each. The five other atmospheric profiles consist of (1) Tropical (15° N), (2) Midlatitude Summer (45° N-July), (3) Midlatitude Winter (45° N-January), (4) Subarctic Summer (60° N), and (5) Subarctic Winter (60° N-January). Additionally the user may input radiosonde data if desired to make calculations for a specific profile.

The LOWTRAN code includes three boundary layer aerosol types: Rural, Urban, and Maritime. Due to the nature of the scenario, only the latter was used to simulate an engagement of an anti-ship missile in open waters. These aerosols are largely sea-salt particles in the lower boundary layer caused by evaporation of sea-spray droplets. Together with a background aerosol of more or less pronounced continental characteristics they form a fairly uniform maritime aerosol which is representative of the lower 2 to 3 kilometers of the atmosphere over the oceans.

These aerosols should not be confused with the heavy direct sea-spray aerosols found in the lower 10 to 20 meters above the ocean surface which are strongly dependent on recent wind and sea surface turbulence. The extinction and absorption coefficients are calculated as a function of the relative humidity and based heavily upon the refractive index for the given altitude and weather conditions.

The ability to calculate slant-path transmittance is incorporated in the LOWTRAN VI utilizing a data base of seasonal and latitude dependencies of vertical aerosol distributions. This allows transmittance calculations of medium and high altitude missile attack profiles.

The LOWTRAN code calculates transmittance as a function of "absorber density" for the path, the pressure, and temperature, for the particular wavelength band chosen. It utilizes both empirical laboratory data and available molecular line constant data in performing its calculations.

The aerosol population found over the world's ocean is significantly different in composition and distribution from that of a continental origin. These aerosols are largely derived from the sea. They are produced by the evaporation of sea spray and from jet and film droplets. Jet droplets are ejected into the air by the bursting of small air bubbles at the sea surface. The bursting of the bubble film leaves behind many smaller film droplets that may also be diffused into the air. These mechanisms are wind dependent and require whitewater phenomenon to produce aerosol.

Once the aerosol droplets are airborne, they undergo additional

sorting and mixing processes. The marine boundary layer is usually capped by a temperature inversion and, within the boundary layer, the smaller marine aerosol together with any background aerosol form a fairly uniform aerosol spatial distribution. Once introduced into the atmosphere the lifetime of an aerosol particle is dependent on the size of the particular aerosol particle. Those with very small sizes have a very long residence time in the boundary layer if there are no washout processes taking place. On the other hand, those with very large sizes have a short residence time and do not contribute to the stationary long-term aerosol population. The reader is recommended to Reference[28] for more details.

APPENDIX E. SINGLE LENS DESIGN

The single lens used on the radiative transfer of the computation of detector irradiance was designed using the program ZEMAX-XE. In this appendix are included the output plots of such a computation.

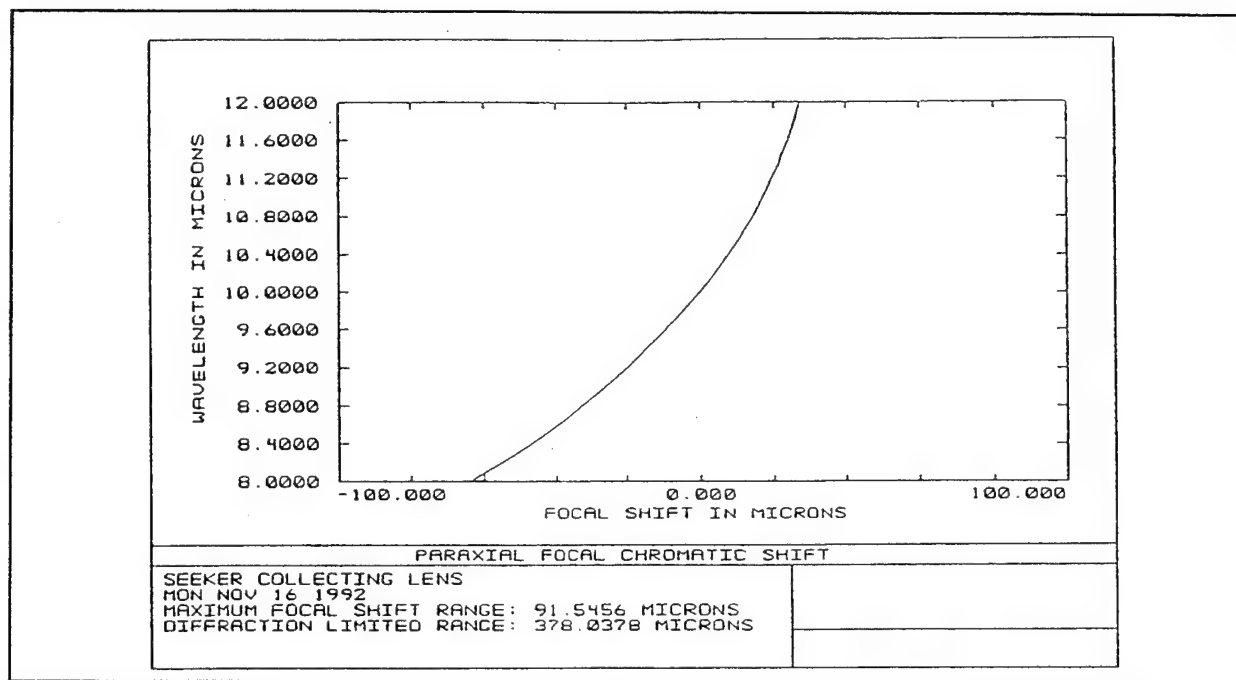


Figure E-1. Seeker collecting lens focal chromatic shift.

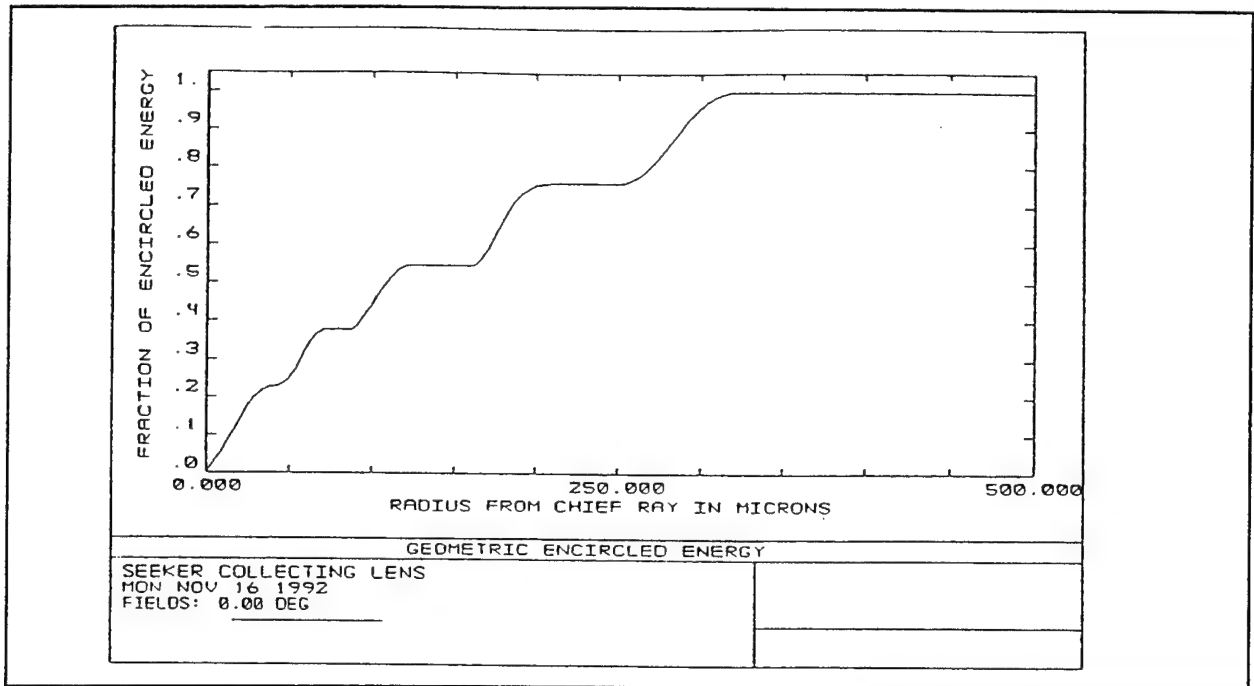


Figure E-2. Seeker collecting lens geometric encircled energy.

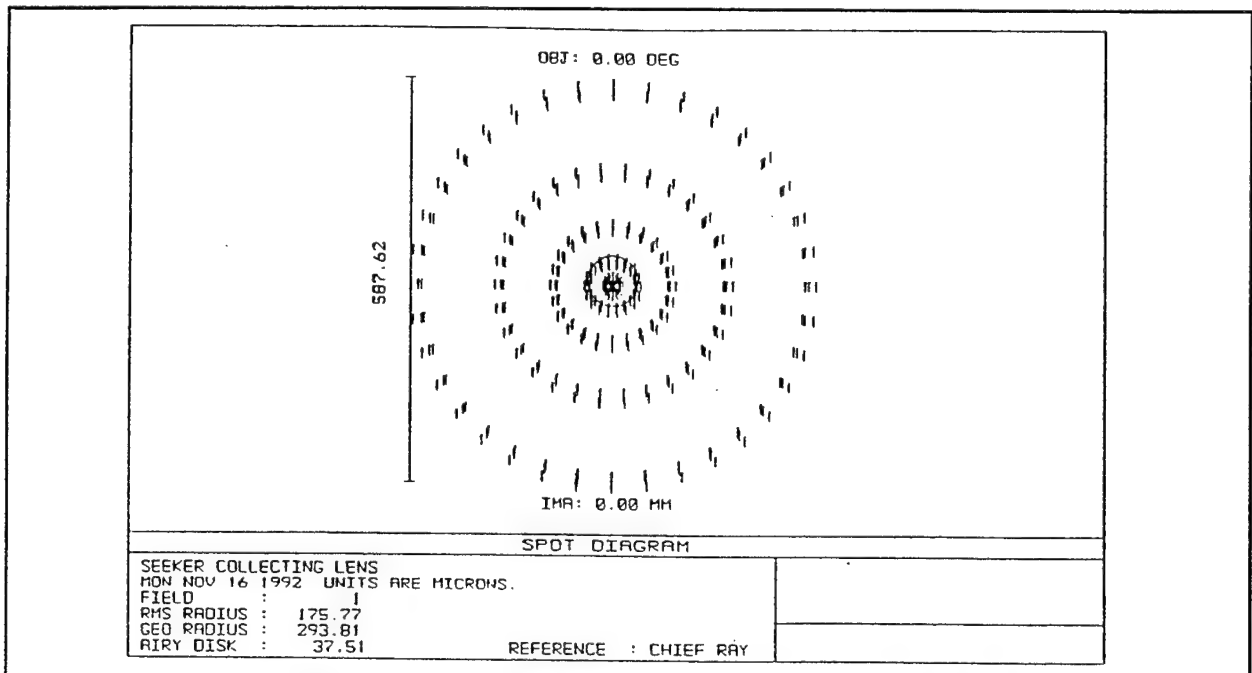


Figure E-3. Seeker collecting lens paraxial chromatic shift.

APPENDIX F. "POLE-FIT" EMISSIVITY MODEL

The "classical pole-fit" model" represents the complex permittivity, ϵ , in the form of the lattice vibrations[24]:

$$\epsilon(\nu, T) = \epsilon_{\infty} + \sum_j \frac{\Delta\epsilon_j(T) \nu_j^2(T)}{\nu_j^2(T) - \nu^2 - i\gamma_j(\nu, T)\nu}, \quad (F-1)$$

where $\Delta\epsilon_j$, γ_j are the j^{th} mode strength, line width, and long wavelength transverse optical frequency, respectively. This model adequately describe the reflectance, R , in the infrared region. Using Eq.(F-1), the static dielectric constant, $\epsilon_s(T) = \epsilon(0, T)$, becomes

$$\epsilon_s(T) = \epsilon_{\infty}(T) + \sum_j \Delta\epsilon_j(T). \quad (F-2)$$

The frequency dependence of γ_j represents a cutoff beyond the one-phonon region caused by anharmonicities of the potential. The cutoff is empirically represented as follows

$$\gamma_j = \gamma_j(T) \cdot 1; \quad \nu \leq \bar{\nu} \\ \cdot \exp \left[-\alpha \left(\frac{\nu^2}{\bar{\nu}} \right) - 1 \right]; \quad \nu \geq \bar{\nu} \quad (F-3)$$

where α and $\bar{\nu}$ are arbitrary parameters. Michael Thomas team at APL has been most successful in this effort by choosing $\alpha = 4$ and $\bar{\nu}$ as 1.1 times the highest infrared allowed transverse optical optical mode frequency.

As Eq.(F-1) suggests, the reflectance is a function not only of frequency but also of temperature. The temperature dependence of the transverse mode frequencies, ν_{T0j} , and the mode strengths, $\Delta\epsilon_j$, can be represented by linear equations of the form

$$\nu_{T0j}(T) = \nu_{T0j}(T_o) + a_j(T - T_o) \quad (F-4)$$

and

$$\Delta\epsilon_j(T) = \Delta\epsilon_j(T_o) + b_j(T - T_o) \quad (F-5)$$

where T_o is a reference temperature and a_j and b_j are mode- and material-specific constant coefficients. The dependence of the linewidth on temperature can be described by a quadratic equation in T as

$$\frac{\gamma_j}{\nu_{T0j}}(T) = \frac{\gamma_j}{\nu_{T0j}}(T_o) + c_j(T - T_o) + d_j(T - T_o)^2, \quad (F-6)$$

where T_o is again a reference temperature and c_j and d_j are mode and material-specific constant coefficients. The high-frequency permittivity, ϵ_∞ , is also temperature dependent and is represented by

$$\epsilon_\infty(T) = \epsilon_\infty(T_o) + e_j(T - T_o). \quad (F-7)$$

$e_j = d\epsilon_\infty/dT = 2n_\infty(dn_\infty/dT)$; thus, in most cases, e_j is determined from dn/dT measurements at the helium-neon laser frequency.

APPEENDIX G. RESULTS FROM ELECTROMAGNETIC THEORY

For optically smooth surfaces that are physically and chemically clean, electromagnetic theory with the aid of Kirchoff's law provides a prediction of the magnitude and distribution of the directional emissivity[12]. The radiation emission properties of the aforementioned ideal surfaces are sometimes distinguished by using the term emissivity instead of emittance.

Radiant energy either incident on or leaving from a surface can be resolved into two components of polarization. One of these components is polarized parallel to the plane of incidence and the other is polarized perpendicular to the plane of incidence. The electromagnetic theory predicts the specular reflectance ρ^s corresponding to each component of polarization, defined as the ratio of the monochromatic intensities of that component in the reflected and incident beams.

The expressions for ρ_{\perp}^s (perpendicular polarized component) and ρ_{\parallel}^s (parallel polarized component) constitute the well-known Fresnel law of reflection assuming that the medium adjacent to the reflecting surface has a refractive index of unity and an extinction coefficient of zero (vacuum and gases). These expressions are derived for monochromatic radiation. However, the subscript λ is omitted in order to avoid complicating an already cumbersome notation. The resulting equations are

$$\rho_{\perp}^s = \frac{a^2 \cdot b^2 \cdot 2a \cos \theta \cdot \cos^2 \theta}{a^2 \cdot b^2 \cdot 2a \cos \theta \cdot \cos^2 \theta} \quad (G-1a)$$

$$\rho_1^s(\theta) = \frac{a^2 \cdot b^2 - 2a \sin \theta \tan \theta \cdot \sin^2 \theta \tan^2 \theta}{a^2 \cdot b^2 + 2a \sin \theta \tan \theta \cdot \sin^2 \theta \tan^2 \theta} \quad (\text{G-1b})$$

The angle θ is the specular-ray direction corresponding to an incident beam whose angle of inclination is $\psi = \theta$. The quantities a and b are related to the angle of reflection θ and to the refractive index n and the extinction coefficient k of the material on which the radiation is incident.

$$2a^2 \cdot \sqrt{(n^2 - k^2 - \sin^2 \theta)^2 + 4n^2 k^2} \cdot (n^2 - k^2 - \sin^2 \theta) \quad (\text{G-2a})$$

$$2b^2 \cdot \sqrt{(n^2 - k^2 - \sin^2 \theta)^2 + 4n^2 k^2} \cdot (n^2 - k^2 - \sin^2 \theta) \quad (\text{G-2b})$$

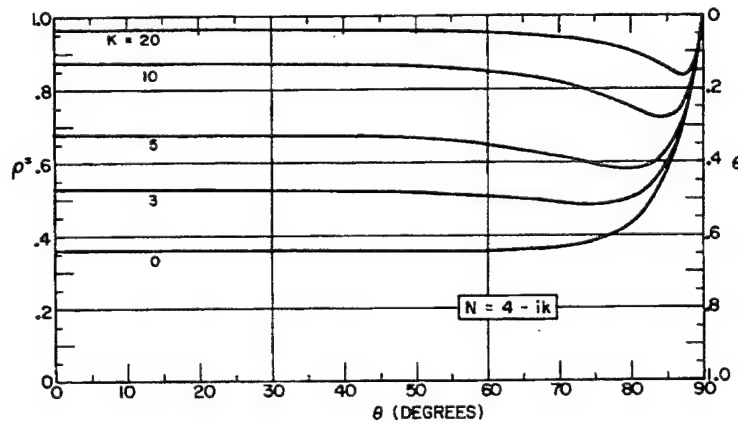


Figure G-1. Predictions of the monochromatic emissivity and the specular reflectance from electromagnetic theory.

The complex index of refraction, n , is defined taking the optical constants n and k together, as follows

$$\mathbf{n} = n - ik \quad (\text{G-3})$$

If the incident radiation is unpolarized, then the two components of polarization in the incident beam are of equal intensity. In this case it is readily verified that the monochromatic specular reflectance is the average of ρ_{\perp}^s and ρ_{\parallel}^s , that is,

$$\rho^s(\theta) = \frac{1}{2} [\rho_{\perp}^s(\theta) + \rho_{\parallel}^s(\theta)] \quad (G-4)$$

The monochromatic directional absorptivity, $\alpha(\theta)$, can be determined using Kirchhoff's law,

$$\alpha(\theta) = 1 - \rho^s(\theta) = 1 - \frac{1}{2} [\rho_{\perp}^s(\theta) + \rho_{\parallel}^s(\theta)] \quad (G-5)$$

Due to the fact that Kirchhoff's law applies directionally and monochromatically for each component of polarization, one can write the components

$$\epsilon_{\perp}(\theta) = \alpha_{\perp}(\theta) = 1 - \rho_{\perp}^s(\theta) \quad (G-6b)$$

$$\epsilon_{\parallel}(\theta) = \alpha_{\parallel}(\theta) = 1 - \rho_{\parallel}^s(\theta) \quad (G-6a)$$

Furthermore, the directional emissivity of the mixed radiation is the average of ϵ_{\perp} and ϵ_{\parallel} , that is,

$$\epsilon(\theta) = \frac{1}{2} [\epsilon_{\perp}(\theta) + \epsilon_{\parallel}(\theta)] \quad (G-7)$$

Although the subscript λ is omitted for notational simplicity, the foregoing equations, as well as those that follow, are to be regarded as applying monochromatically.

The predictions of electromagnetic theory for ρ_{\perp}^s and ρ_{\parallel}^s can be employed to provide an expression for the directional emissivity.

Upon substituting equations (G-1) into equations (G-6) e (G-7), one obtains

$$\varepsilon(\theta) = \frac{1}{2} \varepsilon_{\perp}(\theta) \left[1 + \frac{a^2 \cdot b^2 \cdot \sin^2 \theta}{\cos^2 \theta (a^2 \cdot b^2 \cdot 2a \sin \theta \tan \theta \cdot \sin^2 \theta \tan^2 \theta)} \right] \quad (G8)$$

where

$$\varepsilon_{\perp}(\theta) = \frac{4a \cos \theta}{a^2 \cdot b^2 \cdot 2a \sin \theta \cdot \cos^2 \theta} \quad (G-9)$$

The quantities a and b are related to the optical constants and to the angle of emission θ by equations (G-2). If n and k are known, Eq.(G-8) provides a prediction of the directional distribution of the monochromatic emissivity of an optically smooth surface.

The hemispherical emissivity ε can be determined from the directional emittance by integrating over the hemisphere. By introducing the definitions of ε and $\varepsilon(\theta)$, the emissivity can be computed using the following relation

$$\varepsilon = \frac{1}{\pi} \int_{hem} \varepsilon(\theta) \cos \theta d\omega \quad (G-10)$$

Eq.(G-8), can be then be employed to provide a prediction for ε . In the case of an electric nonconductor ($k = 0$), the execution of the integration yields

$$\frac{\varepsilon}{\varepsilon_n} = \frac{1}{2} \left[\frac{2}{3} + \frac{1}{3n} \cdot \frac{n(n+1)^2(n^2-1)^2}{2(n^2+1)^3} \ln \left(\frac{n+1}{n-1} \right) + \frac{n^2(n+1)(n^2+2n-1)}{(n^2+1)^2(n-1)} - \frac{4n^2(n^4+1)}{(n^2+1)^3(n-1)^2} \ln n \right] \quad (G-11)$$

in which ε_n is the emissivity in the direction normal to the surface

$$\varepsilon_n = \frac{4n}{(n+1)^2} \quad (G-12)$$

The ratio of the hemispherical to the normal emissivity ratio has practical significance inasmuch as it is the normal emissivity that is more often determined by experiment, whereas it is the hemispherical emissivity that is usually needed in the computation of the radiant interchange. The ratio $\varepsilon/\varepsilon_n$ is presented in Fig. G-2 as a function of the refractive index for parametric values of the extinction coefficient $k_0 = k/n$. Within the range of n and k values that correspond to real materials, the $\varepsilon/\varepsilon_n$ ratio is greater than one for metals and less than one for dielectrics. For the latter materials, ε is only slightly less than ε_n .

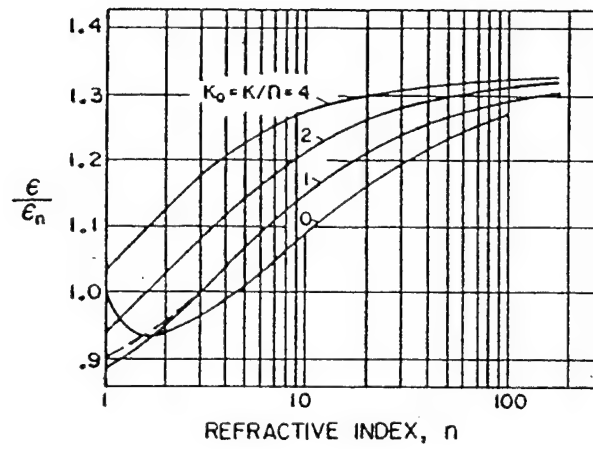


Figure G-2. Ratio of the hemispherical to the normal emissivity as predicted by electromagnetic theory.

APEENDIX H. RADIATION TRANSFER SOURCE CODE

The program listed below was written in MATLAB and computes the background photon flux on an nxn FPA originated by a hemispherical dome. The method used follows the procedure outlined in the section A and B of this chapter. The program assumes that the dome temperature has cylindrical symmetry and that the optical system is looking straight ahead.

1. Input Parameters

The temperature distribution, in kelvins, is entered in the vector *tempdata*. The first element is the dome stagnation temperature. The other temperature information is chosen in points downstream in order to ensure that a reasonable coverage of the dome is achieved. The *coord* has the radial coordinates (measured from the dome axis in cm) of the points corresponding to the data of vector *tempdata*.

Following is a list of the input parameters:

- > NW - radial discretization number of elements of the dome;
- > MW - number of sectors used to discretize the dome;
- > Rpupil - radius of the pupil measured from the dome axis(m);
- > R1 - radius of curvature of lens front surface(m);
- > R2 - radius of curvature of lens back surface(m);
- > Rdome - radius of curvature of the dome(m);
- > t - lens thickness;
- > t1 - lens separation from the dome;

-> t3 - backsurface focal length;
-> lambdamin - cut-on wavelength(microns);
-> lambdamax - cut-off wavelength(microns);
-> ND - sqrt(number of array pixels);
-> cell separation(microns);
-> em - dome emissivity;
-> n - index of refraction of the media suurronding the
lens;
-> nl - index of refraction of the lens;
-> toptics - cold optics optical transmission.

```

%%%%%%%%%%%%%%%%%%%%%%%%%%%%%%%%%%%%%%%%%%%%%%%%%%%%%%%%%%%%%%%%%%%%%%%%
%               @ LT Clelio D. Ferreira Leite               %
%               Monterey, 16 Nov 1992                       %
%               This program written in MATLAB               %
%               computes the photon irradiance on a FPA      %
%               originated by a hot window hemispherical dome %
%%%%%%%%%%%%%%%%%%%%%%%%%%%%%%%%%%%%%%%%%%%%%%%%%%%%%%%%%%%%%%%%%%%%%%%%

```

```

clear
format long e
ttime=clock

```

```

%%%%%%%%%%%%%%%%%%%%%%%%%%%%%%%%%%%%%%%%%%%%%%%%%%%%%%%%%%%%%%%% input parameters %%%%%%%%%%

```

```

coord=[0 0.0078 0.0115 0.0132 0.0158 0.0175 0.0189];
Tempdata=[1222 1183 1150 1112 975 945 905];
Tempcoef=polyfit(coord,Tempdata,6);
NW=41;%odd #
MW=60;%even #
Rpupil=.016;
R1=.600;
R2=-.500;
RW=.03166;
t=.003;
t1=.01;
t3=.090999;
lambdamin=8.0;
lambdamax=10.5;
ND=63;%even
cellsep=30e-6;
em=.05;
n=1.0;
nl=4.00431;
toptics=.5;

```

```

%% Compute coordinates on conjugate window and detector site %%%%%%%%%%

```

```

xdlim=ND*cellsep/2;
lambdamean=(lambdamax+lambdamin)/2;
Adbin=cellsep^2;
Tstag=polyval(Tempcoef,0)%1144;

```

```

    z1=n*t/nl;
    z2=1/R2*(nl/n-1)*(n*t/nl);
    z3=1;
    zc=-z1/((z2+z3));

```

```

for i=1:NW;
    r(i)=Rpupil*i/NW;
    z(i)=sqrt(RW^2-r(i)^2)+t1;
end

```

```

for i=1:2:NW-2;
    T(i)=polyval(Tempcoef,r(i+1));
end

```

```

for i=1:NW;
    z1=z(i)+t.*z(i)/R1*(n/nl-1)+n*t/nl;
    z2=1/R2*(nl/n-1)*(z(i)+t.*z(i)/R1*(n/nl-1)+n*t/nl);

```



```

dywd=ydet(n,m);
dzwd=t3-zc;
normwdx=dxwd/rwd;
normwdy=dywd/rwd;
normwdz=dzwd/rwd;

dotprodw=inorm*normwdx+jnorm*normwdy+knorm*normwdz;
normsurf=sqrt(inorm^2+jnorm^2+knorm^2);
normwd=sqrt(normwdx^2+normwdy^2+normwdz^2);
costhetaw=abs(dotprodw/((normsurf*normwd)));
dotprodd=-normwdz;
costhetad=abs(dotprodd/(normwd));
Qlambda=en*c3/(lambdamean^4*(exp(c2/(lambdamean*Tstag)-1)))*(lambdamax-lambdamin)
Q=Qlambda*daw*Adbin*costhetad*costhetaw/rwd^2;
Qbin(n,m)=Qbin(n,m)+Q;
end
end
end
end

%%% Compute Photon Flux %%%%%%%%%%%%%%%%%%%%%%%%%%%%%%%%%%%%%%%%%%%%%%%%%%%%%%%%%%%%%%%%%%%%%%%%%%%

for n=1:(ND+1)/2;
    elapsed_time=round(etime(clock,ttime))
    for m=1:(ND+1)/2;
        for k=1:2:NW-2;
            for l=2:2:MW;
                %Compute coordinates on conjugate window and detector site

                daw=pi*(r(k+2).^2-r(k).^2)/MW;
                rwd=sqrt((xconj(k+1,l)-xdet(n,m)).^2+(yconj(k+1,l)-ydet(n,m)).^2+(t3-zconj(k+1,l)

                dx1=xconj(k+2,l)-xconj(k,l);
                dy1=yconj(k+2,l)-yconj(k,l);
                dz1=zconj(k+2,l)-zconj(k,l);

                if l==MW;
                    dx2=xconj(k+1,l)-xconj(k+1,MW-1);
                    dy2=yconj(k+1,l)-yconj(k+1,MW-1);
                    dz2=zconj(k+1,l)-zconj(k+1,MW-1);
                else
                    dx2=xconj(k+1,l+1)-xconj(k+1,l-1);
                    dy2=yconj(k+1,l+1)-yconj(k+1,l-1);
                    dz2=zconj(k+1,l+1)-zconj(k+1,l-1);
                end

                icross=dy1*dz2-dz1*dy2;
                jcross=-dx1*dz2+dz1*dx2;
                kcross=dx1*dy2-dy1*dx2;
                lcross=sqrt(icross^2+jcross^2+kcross^2);

                inorm=icross/lcross;
                jnorm=jcross/lcross;
                knorm=kcross/lcross;

                dxwd=xdet(n,m)-xconj(k+1,l);
                dywd=ydet(n,m)-yconj(k+1,l);
                dzwd=t3-zconj(k+1,l);
                lwd=sqrt(dxwd^2+dywd^2+dzwd^2);

```

```

        z3=n1/n*(z(i)/R1*(n/n1-1)+n/n1);
        zcon(i)=-z1/((z2+z3));
        A1=1+t/R1*(n/n1-1);
        A2=1/R1*(n/n1-1)*(1+t/R1*(n/n1-1)+n1/n);
        A=A1+zcon(i).*A2;
        rconj(i)=A*r(i);

    for j=1:MW;
        xconj(i,j)=rconj(i)*cos(2*pi/MW*j);
        yconj(i,j)=rconj(i)*sin(2*pi/MW*j);
        zconj(i,j)=abs(zcon(i));
    end

end

x=xconj;
y=yconj;
z=zconj;
r=sqrt(x.^2+y.^2);

xdet=zeros(ND);
ydet=zeros(ND);
for n=1:ND+1
    for m=1:ND+1;
        xdet(n,m)=-xdlim+(n-1)*cellsep;
        ydet(n,m)=-xdlim+(m-1)*cellsep;
    end
end
Qbin=zeros(ND+1)

axis('square')

Qlambda=0;
c2=1.4388e4;
c3=1.8837e27;

%%% Compute photon flux originated by the dome central element %%%%%%%%%%

% rwd - virtual distance between the conjugate surface and the pixel at
%       detector;
% daw - area of finite element at the conjugate surface;
% costhetaw - angle between the normal to the conjugate surface
%             and the line of radiative interchange;
% costhetad - angle between the normal to the detector
%             and the line of radiative interchange;
% Qlambda - photon exitance of the dome
% Q - photon irradiance originated by a certain portion of the dome in a
%     pixel element;

for n=1:(ND+1)/2;
    for m=1:(ND+1)/2;

        daw=pi*r(1).^2;
        rwd=sqrt((-xdet(n,m)).^2+(-ydet(n,m)).^2+(t3-zc)^2);

        inorm=0;
        jnorm=0;
        knorm=1;

        dxwd=xdet(n,m);

```

```

normwdx=dxwd/lwd;
normwdy=dywd/lwd;
normwdz=dzwd/lwd;

dotprodw=inorm*normwdx+jnorm*normwdy+knorm*normwdz;
normsurf=sqrt(inorm^2+jnorm^2+knorm^2);
normwd=sqrt(normwdx^2+normwdy^2+normwdz^2);
costhetaw=abs(dotprodw/((normsurf*normwd)));
dotprodd=-normwdz;
costhetad=abs(dotprodd/(normwd));
Qlambda=em*c3/(lambdamean^4*(exp(c2/(lambdamean*T(k))-1)))*(lambdamax-lambdamin)
Q=Qlambda*daw*Adbin*costhetad*costhetaw/rwd^2;
Qbin(n,m)=Qbin(n,m)+Q;
end
end
end

for n=1:(ND+1)/2;
    for mm=(ND+1)/2+1:ND+1;
        Qbin(n,mm)=Qbin(n,ND+2-mm);
    end
end

for m=1:ND+1;
    for nn=(ND+1)/2+1:ND+1;
        Qbin(nn,m)=Qbin(ND+2-nn,m);
    end
end

save win1 Qbin

```

LIST OF REFERENCES

- [1] J. Rowe, A. Blume, and E. Boudreaux, *Dual-mode Dome Requirements for Future Air-to-Air Missiles*, Proceedings of the Third DoD, Symposium on Electromagnetic Windows, GAGIAC, Chicago, IL, 1990.
- [2] *The Infrared Handbook*, Chapter 24, The Infrared Information (IRIA) Center, 1978.
- [3] Uwe G. Hingst, *Laminar / Turbulent Flow Transition Effects on High Speed Missile Domes*, AGARD Conference Proceedings No.493, 1991.
- [4] Claude Klein, *Diamond Domes for High-Velocity Missiles: An Initial Assessment*, Proceedings of the Fourth DoD Symposium on Electromagnetic Windows, Naval Postgraduate School, 1991.
- [5] John D. Anderson, *Modern Compressible Flow*, McGraw-Hill Publishing Company, 1990.
- [6] Frederick S. Billig, *Shock-Wave Shapes around Spherical and Cylindrical-Nosed Bodies*.
J. Spacecraft and Rockets, Vol.4, June 1967.
- [7] J. Hayes and R. Neumann, *Tactical Missile Aerodynamics: Prediction Methodology*, Progress in Aeronautics and Astronautics, May 1991.
- [8] Robert Truitt, *Fundamentals of Aerodynamic Heating*, The Ronalds Press Company, 1960.
- [9] Daniel C. Harris, *Infrared Window and Dome Materials*, SPIE, Tutorial Text, 1992.
- [10] Claude Klein, *Infrared Missile Domes: Is there a Figure of Merit for Thermal Shock?*, RAY/RD/T-1202, Sep 1992.
- [11] E.M. Sparrow, R.D.Cess, *Radiation Heat Transfer*, Hemisphere Publishing Corporation.
1978.
- [12] Michael Thomas, *High Temperature Optical Properties of Oxide Dome Materials*, Johns Hopkins University, Applied Physics Laboratory, 1992.
- [13] Claude Klein, Personal Communication.
- [14] W.Tropf, M.Thomas,T.Harris, *Performance of Optical Sensors in Hypersonic Flight*, Johns Hopkins University, Technical Digest, Oct-Dec 1987.
- [15] T. Pulliam, J. Steger, *Implicit Finite-Difference Simulations of Three-Dimensional Compressible Flow*, AIAA Journal 1980.
- [16] C.Davies and E. Venkatapathy, *The Multidimensional Version of the Self-Adaptative Grid Code Sage*, Sterling Software, Palo Alto, CA, Jan 1991.
- [17] C.Davies and E. Venkatapathy, *A Simplified Self-Adaptative Grid Method*, SAGE, NASA Technical Memorandum 102198, Oct 1989.
- [18] David A. Anderson, Tannehill, Fletcher, *Computational Fluid Mechanics and Heat Transfer*, Hemisphere Publishing Corporation, 1984.
- [19] Charles L. Merkle, *Computational Fluid Dynamics of Inviscid and High Reynolds Number Flows*, Department of Mechanical Engineering,

The Pennsylvania State University at State Park, 1990.

[20] Tsuying Hsieh, *An Investigation of Separated Flow about a Hemisphere-Cylinder at Incidence in the Mach Number Range from 0.6 to 1.5*, AEDC, AIAA 1977.

[21] Pedrotti and Pedrotti, *Introduction to Optics*, Prentice-Hall, Inc., 1987.

[22] J.M.Lloyd, *Thermal Imaging Systems*, Plenum Press, 1975.

[23] Nussbaum and R.A.Phillips, *Contemporary Optics for Scientists and Enginners*, Prentice-Hall, 1976.

[24] Michael E. Thomas, *A Computer Code for Modeling Optical Properties of Window Materials*, SPIE Vol. 1112, Window and Dome Technologies and Materials, 1989.

[25] Claude A. Klein, *Hot Infrared Domes: A Case Study*, RAY/RD/T-1189, 31 July 1990.

[26] Claude A. Klein, *On Photosaturation of Intrinsic Detectors*, *Applied Optics*, Vol.8, page 1897, Sep 1969.

[27] Irving Spiro and Monroe Schlessinger, *Infrared Technology Fundamentals*, Series in Optical Engineering, Marcel Dekker Inc., 1989.

[28] *Atmospheric Transmittance/Radiance Computer Code LOWTRAN 6*, AFGL-TR-83-0187, Aug 93.

[29] Eustace Dereniak, Devon Crowe, *Optical Radiation Detectors*, John Wiley & Sons, 1984.

[30] Stanley Smith, China Lake, Presentation at the Naval Postgraduate School, 1992.

[31] A. Milton, F. Barone, M. Kruer, *Influence of Nonuniformity on Infrared Focal Plane Array Performance*, *Optical Engineering*, Vol. 24 No 5, October 1985.

[32] G. D. Boreman, P.L. Heron, *Description of Fixed-Pattern Noise in CCD's Using The Spatial Power Spectrum*, SPIE Vol 636, Thermal Imaging, 1986.

INITIAL DISTRIBUTION LIST

		No. Copies
1.	Defense Technical Information Center 8725 John J. Kingman Rd., STE 0944 Ft. Belvoir, Virginia 22060-6218	2
2.	Library, Code 13 Naval Postgraduate School Monterey, California 93943-5100	2
3.	Naval Air Warfare Center Weapons Division Attn: Code 3941 Dr. T. Smith China Lake, California 93555-6001	1
4.	Raytheon Company, Research Attn: Dr. Claude A. Klein Lexington, Massachusetts 02173	1
5.	The Johns Hopkins University Applied Physics Laboratory Attn: Dr. Michael E. Thomas Laurel, Maryland 20707-6099	1
6.	Texas Instruments Incorporated Aero/Thermal Technology Branch Attn: Dr. Craig L. Lee P.O. Box 405 M/S 3453 Lewisville, Texas 75067	1
7.	Superintendent, Naval Postgraduate School Attn: Professor Alfred W. Cooper (Code PH/Cr) Monterey, California 93943	2
8.	Superintendent, Naval Postgraduate School Attn: Professor Max Platzner (Code AA/Pl) Monterey, California 93943	2
9.	Superintendent, Naval Postgraduate School Attn: Professor Scott Davis (code PH/Da) Monterey, California 93943	1

10. Direcção do Serviço de Instrução e Treino 1
2ª Repartição
Praça do Municipio
1188 Lisboa CODEX
PORTUGAL
11. Att: Eng. Clelio Dinis Ferreira Leite 1
Chefe dos Sistemas Electro-Ópticos
Direcção de Navios
B.N.L. - Alfeite
2800 ALMADA
PORTUGAL
12. Att: Prof. Carvalho Rodrigues 1
Instituto Nacional de Engenharia e Tecnologia Industrial
Estrada do Paço do Lumiar
1699 Lisboa Codex
PORTUGAL
13. Att: Prof. José Leandro Andrade Campos 1
Laboratório de Energética e Detónica
Rua Pinheiro Chagas, 96
3000 Coimbra
Portugal